AFOSR-88-0143

NUMERICAL SIMULATION OF CIRRUS CLOUDS - FIRE CASE STUDY AND SENSITIVITY ANALYSIS

by Capt. Scot T. Heckman

William R. Cotton, P.I.

Colorado State University

DEPARTMENT OF ATMOSPHERIC SCIENCE

PAPER NO. 483

NUMERICAL SIMULATION OF CIRRUS CLOUDS -

FIRE CASE STUDY AND SENSITIVITY ANALYSIS

by

Capt. Scot T. Heckman

Department of Atmospheric Science

Colorado State University

Fort Collins, CO 80523

August 12, 1991

Atmospheric Science Paper No. 483

ABSTRACT OF THESIS

NUMERICAL SIMULATION OF CIRRUS CLOUDS - FIRE CASE STUDY AND SENSITIVITY ANALYSIS

The October 28, 1986 FIRE (First ISCCP Regional Experiment) case was simulated using the Regional Atmospheric Modeling System — RAMS developed at Colorado State University. This three dimensional, mesoscale model was applied in non-hydrostatic and nested-grid mode using explicit, bulk microphysics and radiation. The simulation resulted in very good agreement between observed and model predicted dynamic and cloud fields. We verified cloud height, thickness, areal extent and microphysical composition against GOES satellite imagery, lidar, and aircraft measurements taken during the FIRE Cirrus IFO (Intensive Field Observation). We examined the simulated cirrus lifecycle to determine possible formation, maintenance and dissipation mechanisms. Sensitivity simulations were run to determine long and short wave radiative forcing. Also, a simulation was run with no condensate to examine cloud feedbacks on the environment. Cloud top generation zones, fallstreaks, and layering were simulated. Longwave radiation appeared to be instrumental in developing weak convective activity in the lower layer thereby increasing it's optical depth. Cloud top cooling and cloud base heating affected the flow around the cloud. Secondarily, we studied the effects of three upper boundary conditions on cirrus clouds in a synoptic setting.

Capt. Scot T. Heckman
Department of Atmospheric Science
Colorado State University
Fort Collins, Colorado 80523
Spring 1991

i

ACKNOWLEDGEMENTS

TABLE OF CONTENTS

LIST OF FIGURES

Chapter 1

INTRODUCTION

Cirrus clouds cover about 20% of the globe on average and have been identified as a major uncertainty in our ability to diagnose and forecast climate change. It is hypothesized that cirrus clouds are a positive feedback to global warming due to their impact on the tropospheric radiation budget. Understanding this impact requires knowledge of the radiative effects of cirrus clouds, but, just as important, it requires knowledge of cirrus dynamics. These dynamics include the environment and processes responsible for cirrus formation, maintenance and dissipation. Cirrus research, therefore, has taken two paths: research into radiative effects and the focus of this study, exploration of cirrus dynamics.

Although cirrus research has lately been related to climate studies, better understanding of cirrus will benefit the operational meteorologist as well. Cirrus affect aircraft operations by causing turbulence and restricting visibility. Turbulence can interrupt midair refueling in the case of Department of Defense aircraft and can cause commercial airliners to change flight levels. Visibility restrictions, while much less than thicker, low level clouds, can still affect surveillance activities. Agricultural concerns will benefit from better cirrus forecasting. Cirrus reduce surface heating thus reducing evapotranspiration processes which, in turn, affect irrigation scheduling.

Future cirrus cloud forecast algorithms will require a method of diagnosing cloud height, thickness, coverage and microphysical properties from large scale resolvable fields. That is, mathematical relationships between the cirrus environment and resulting cloud properties will be required. In order to derive general relations, detailed observations of all types of cirrus are necessary. The observations must include dynamical properties such as horizontal motions, vertical motions, turbulent motions and static stability. They must also include

microphysical properties such as ice particle size distribution, crystal habit, and concentration. The First ISSCP (International Satellite Cloud Climatology Program) Regional Experiment (FIRE) combines satellite, airborne and surface observations of cirrus cloud systems in hopes of improving cloud and radiative parameterizations in climate models. FIRE sponsored an intensive field observation (IFO) for cirrus in Wisconsin during October of 1986. Results from this experiment are described in detail in the special November 1990 issue of *Monthly Weather Review*.

There is a limit to the time and space coverage of such observations. In order to fill in the gaps, numerical models are often used to supplement these datasets. Once verified against the observations, model output can be used to derive the statistical relationships needed. Thus, observational programs such as FIRE and modeling studies are highly complementary approaches in our quest to understand the cirrus lifecycle.

Cirrus are one of the most intricate of all cloud systems resulting from feedbacks between the large scale flow, turbulent motions, convective processes, radiative transfer and microphysical processes. They are also the result of complex scale interaction. They cover extensive areas when associated with synoptic scale weather features. They exhibit mesoscale organization with $20 - 100km$ areas of enhanced cloudiness. Also microscale features have been observed only $1km$ across. The resulting clouds are typically horizontally inhomogeneous with large variations in microphysical properties. It is this inhomogeniety that make determining their overall effects so difficult. The horizontal variations are compounded by the fact that cirrus often occur in layers, at times only hundreds of meters thick.

A model capable of representing all these interactions would be enormously complex. In reality, no such model exists. Rather, models concentrate on particular scales of interactions. Cloud scale process models simulate the small scale interactions between radiation, microphysics and turbulent motions after assuming a steady state large scale environment. They provide insight into the relative importance of each of the processes. Nested, limited area models are used to bridge the gap between cloud scale modeling and general circulation models (GCMs). These models can accurately reproduce the synoptic scale forcing and,

through the use of nesting, can still resolve mesoscale flows. Both approaches lead to better understanding of cirrus clouds in general.

This thesis is then a modeling study of cirrus clouds. It is the goal of this study to simulate and verify against a cirrus cloud system observed during the FIRE IFO. This study used the pre-existing Regional Atmospheric Modeling System (RAMS) developed at Colorado State University (CSU). RAMS is ideally suited for such a study. It has nested grids, a complete radiation parameterization, and a bulk microphysical parameterization specifically designed for cloud dynamics studies.

The following is an outline of the rest of the thesis:

Chapter 2 provides background information concerning cirrus microphysics, dynamics and modeling.

Chapter 3 describes the RAMS model as used in these simulations. It also describes radiative top boundary conditions tested and implemented as part of this study.

The weather events of 28 October 1986 are described in Chapter 4. 12 hourly analysis of the synoptic conditions, 3 hourly satellite imagery of the upper midwest region, 3 hourly soundings, and hourly surface observations are all used to describe what happened on that day.

The control simulation is described and verified in Chapter 5. Model analyses include dynamic, thermodynamic, moisture and cloud fields.

Chapter 6 addresses some observations of the cirrus lifecycle as simulated in this case.

Chapter 7 compares sensitivity studies to the control run. Sensitivity simulations were run without short or long wave radiation and then without clouds.

Chapter 8 summarizes the results of the case study and draws some conclusions about cirrus dynamics.

And finally, Chapter 9 contains suggestions for further research in this area.

Chapter 2

BACKGROUND

2.1 Introduction

This chapter will review the results of cirrus cloud observational studies, the theoretical views on the controlling dynamics, and the results of numerical modeling studies.

Cirrus clouds can take many forms depending on vertical velocity, wind shear, relative humidity, and static stability. Cirrostratus form with weak, uniform upward motions, saturated air, and high static stability. With less stability and weaker upward motion, convection may form cirrus uncinus, patches of cirrus producing large ice crystals. These crystals may fall several kilometers in subsaturated air and form long trails depending on the wind shear. These crystals have been shown to be important in seeding midlevel supercooled water clouds, contributing to higher precipitation rates (Braham and Spyers-Duran, 1967).

Cirrus clouds are similar to stratocumulus clouds in many ways. Both cloud systems can exist over huge horizontal expanses and, in a synoptic sense, are fairly dynamically inert. Both are governed by a complex balance between radiational effects, turbulence, and microphysical interactions. Both are capped by a temperature inversion; stratocumulus due to subsidence and cirrus due to the tropopause. Both clouds develop well mixed regions and can exhibit multi-layered structures.

However, cirrus are unique in several important ways. They have a much more complex microphysical structure; where ice and liquid water can coexist and precipitation plays an important role in controlling their structure and lifetimes. They are characterized by turbulent mixing in a very stable environment without the strong external diabatic heat flux source at their lower boundary, which dominates stratocumulus. The turbulence is frequently shear-driven rather than buoyancy-driven. They also experience periods of sporadic

turbulent behavior. They often are in regions of widespread ascent while stratocumulus form in regions of widespread descent. These differences make cirrus a much more difficult cloud to explain, forecast or parameterize.

It's worth mentioning some of the problems involved in studying cirrus in order to understand the uncertain nature of the results presented. Measurement of the concentration and habit of cirrus ice crystals requires sophisticated equipment onboard high flying aircraft. This is complicated by the wide range of sizes and geometries evident in cirrus. Equipment designed for spherical water drops doesn't work well on non-spherical ice crystals. Since expensive high- flying aircraft are required, the number of observations are much fewer than those in low-level clouds. Vertical motion measurements have always been difficult but are especially hard when the magnitude of the motions in cirrus clouds is equal to the error in the measurements.

2.2 Observed characteristics

2.2.1 Microphysics

Cirrus are characterized by a wide range of values for crystal habit, crystal diameter and ice water content (IWC). The wide range can be attributed to the various forms of cirrus. Cirrus clouds are comprised mainly of bullets, rosettes, columns and plates. Haloes and sundogs are often seen indicating a hexagonal geometry. These particles are typically 100 to 1000 μm with IWCs on the order of $0.1 g/m^3$. Concentrations measured by Heymsfield (1972) were 10-25 per liter. Heymsfield (1975a) also found high concentrations of particles in the 20-50 μm range (confirmed by Varley (1980)). These particles are very hard to measure but their existence has great consequences for those modeling the radiative properties of cirrus clouds (Stackhouse, 1989).

Sassen et al. (1989) reported sampling liquid water drops both with lidar and aircraft in their case study of cirrostratus. Sassen noted the difficulties in determining the amount of liquid water in cirrus. For lidar measurements, it must comprise a significant fraction of the total mass. For aircraft, the drops must be large enough for the probes to see it. And finally, the drops must not be evaporated or frozen before they can be sampled. Sassen also noted that haze particles can exist in subsaturated conditions at cirrus temperatures.

From the observed crystal habits, some inferences about nucleation can be made. Bullet rosettes are evidence of a freezing mechanism taking place at water saturation. Rosettes were sampled in clouds with relatively large updrafts. In fact, Heymsfield (1975a) only found liquid water in clouds with updrafts greater than 50 cm/s. In less vigorous clouds, plates and columns were found, indicating growth at low ice supersaturation and suggesting a deposition mechanism. This was the case for warm frontal cirrus where no liquid water was found, vertical motion was weak(1-10 cm/s), and RH values were 80-100%. An alternative mechanism may be the homogeneous freezing of haze droplets which may occur at RH values greater than 85%.

Through lidar studies, it has been determined that cirrus crystals are oriented horizontally with their long axis parallel to the ground. The orientation of the crystals is important for scattering and radiative transfer considerations. Lidar polarization values tend to be uniform suggesting the same size and shape crystals due to a common generation and history (Sassen et al., 1989). Heymsfield (1972) derived empirical equations correlating the width and length of the crystals for various temperatures.

Heymsfield (1975b) showed ice water content (IWC) in cirrus depended on temperature and vertical velocity. He showed that IWC increased when temperature increased or vertical velocity increased. Heymsfield and Platt (1984) reported that concentrations were dependent on vertical velocity. They also showed that particle habit distributions and the shape of the particle size distribution were dependent on temperature. Sassen et al. (1989) showed particle concentrations to be temperature dependent and to exhibit a rapid decrease at the -40°C to -45°C range associated with a change in crystal habit from bullet rossettes to columns.

2.2.2 Environment

The different forms of cirrus are products of their different environments. Yagi (1969) observed cirrus uncinus and spissatus to occur in well-mixed regions between stable layers. The difference between these being the degree of stability in the subcloud layer. Heymsfield and Knollenberg (1972) also observed this mixed layer structure and noted that uncinus formed in regions of significant wind shear, often in an area where the shear turned from

negative to positive. Sassen et al. (1989), Quante (1989) and Flatau et al. (1990) all discuss observations of this mixed layer structure.

Cirrus are often associated with jet streams where they appear parallel to high level temperature discontinuities above layers of strong vertical shear (Conover, 1960; Reuss, 1967). Thick cirrostratus tend to occur over warm fronts.

Different cirrus cloud types have different vertical motions. Warm frontal cirrus clouds have vertical motions on the order of 1-10 cm/s, warm front occlusions have 20 cm/s and convective elements near the jet stream have average vertical motions 50-70 cm/s (Heymsfield, 1975a). Vertical motions measured by Smith et al. (1990) during the FIRE Cirrus IFO match these values. Cirrostratus are usually found in large, dense sheets over warm frontal systems while cirrus uncinus are typically more convective in nature.

2.2.3 Heat and Moisture Budgets

Gultepe et al. (1990) derived the heat and moisture budgets of cirrus clouds observed by aircraft during the 1986 FIRE IFO. They determined that there is moisture convergence at the bottom and middle and divergence at the top. For moisture, advection terms are more important than turbulent and microphysical terms. For heat, vertical advection and the radiative cooling terms are dominant. The infrared cooling rate showed warming at cloud base and cooling at the top. Thus, it contributes to destabilization and offsets the surrounding stability.

2.2.4 Turbulence

Since cirrus develop in a stable environment and don't have the strong diabatic heat flux source at their base like stratocumulus, something else must provide the energy for continued mixing. Radiation, latent heat release, vertical wind shear and wave instabilities provide turbulent kinetic energy. Analysis of the turbulence gives insight into the sources and nature of this energy production and dissipation.

Quante (1989) used aircraft time series of vertical motion, potential temperature and horizontal motions to show the presence of waves and turbulence in cirrus clouds. He attributed the turbulence to wind shear and the breaking of Kelvin-Helmholtz waves with

the horizontal scale of a few kilometers to tens of kilometers. The time series showed shorter wavelength waves in the top of the cloud and more turbulence in the lower part. Measurements by Smith et al. (1990) and Sassen et al. (1989) showed this as well. Smith et al. showed that 80% of the variance in the vertical motion was explained by disturbances with a 4 km wavelength in the top of the cloud but by disturbances with wavelengths greater than 10 km near the bottom. They also noticed a jump in variance measured at all levels at the 5 km wavelength suggesting a dominant source of energy at this scale. Quante measured the vertical velocity variance to be a full order of magnitude less than its horizontal counterpart. This suggests a two dimensional nature to the turbulence in cirrus clouds.

Two dimensional turbulence (as summarized by Flatau et al. (1990)) may characterize the turbulence for many cirrus. It is fundamentally different than three dimensional turbulence in that energy does not cascade to smaller scales until it is dissipated on the molecular scale, rather energy propagates up scale and fuels larger scale motions. This 2-D turbulence can be related to cirrus in the following way: Small scale turbulence becomes quasi 2-D under stable stratification. Quasi 2-D turbulence is persistent as dissipation is small. Vertical motions are suppressed compared to horizontal. The cloud shrinks vertically and becomes thin. Motions in individual layers are decoupled.

Flatau et al. (1990) measured more turbulent energy in cloud than in clear air in both the FIRE and GASP data sets. This suggests that processes in the cloud (i.e. cloud diabetic effects) are a major source of turbulence. This supports Starr and Cox (1980) measurements, made using standard rawinsonde data, that buoyancy in cloud was almost always a larger source of turbulent kinetic energy than shear production both in and out of cloud.

2.3 Theories and Numerical Models of Cirrus Dynamics

2.3.1 Frontal Theory

The classic frontal theory describes cirrus clouds formed in the upward moving air above an elevated frontal zone. Adiabatic cooling causes saturation in a large area. This lifting also destabilizes the layer and can deepen the layer if lifting persists. The lifting

is greatest just above the front and the layer in the frontal zone is stable. Strong vertical shear of the horizontal wind is expected across the front. These conditions were found in a study by Reuss (1967) of cirrus formed along frontal surfaces.

Cirrus may form in the lifted air mass above or away from the frontal zone itself where lifting produces saturation. This can occur at high levels, where very little vertical motion is required to produce saturated conditions with respect to ice.

2.3.2 Mixed Layer Theory

Because cirrus display many similarities with stratocumulus, there have been attempts to explain cirrus dynamics with mixed layer theory. The mixed layer assumption is well based on observations (Yagi, 1969; Starr and Cox, 1980; Heymsfield, 1972). Mixed layer theory requires some external heat flux source as a driving mechanism. Some candidates are large scale lifting, radiative processes, shear generation, latent heating processes, and gravity waves. In clouds detached from large scale forcing, the radiative processes coupled with microphysics seem to be the most important.

The main idea behind the mixed layer theory is to treat the cirrus layer as a dry adiabatic layer sandwiched between stable layers. The cloud evolves by entraining stable air from above and beneath. The diabatic heating drives eddies which distribute the entrained air throughout the layer. With a steady source, this process can remain for quite some time.

Another source of energy may be gravity waves propagating in the lower stable layer (Heymsfield, 1975b). In this case, no large scale vertical motion is necessary.

Lilly (1988) applied a mixed layer model to cirrus formed by cumulonimbus outflows. He stated that while the ice mass is convectively-generated, it remains long after the convection as a well mixed layer in otherwise stable region. This mixed layer is the result of convectively-generated 3-D turbulence collapsing to 2-D turbulence and waves under the effects of stability. The mixed layer and ice crystals can then interact radiatively and begin their own circulations.

Lilly considered higher level and thicker clouds than Starr and Cox (1985a). He did not allow interaction with the microphysics.

His results showed that under conditions of net warming, the layer would grow until it eroded the upper temperature inversion completely. Lilly then explained that the mesoscale lifting associated with the heating can be retarded if the now collapsed plume is large enough. He used the analogy of a plate being pulled out of water, the movement is restricted until the water can run off the top. Applying this theory, Lilly then tried to explain why the upper inversion is almost never eroded.

In his conclusions, Lilly wondered if the mixed layer could develop before most of the IWC had precipitated out and became too thin a cloud to produce the needed radiative/convective forcing.

Flatau et al. (1989) also applied a mixed layer model to a cirrus case. Their model predicted the magnitude of the temperature jumps at the top and bottom of the mixed layer and the temperature of the mixed layer itself. Entrainment and the diabatic forcing were parameterized.

Flatau et al. used cloud radiative cooling and warming as the primary diabatic heat sources. For optically thick clouds that exhibit a small temperature difference with the surface, the cloud bottom warming was weak while the cloud top cooling is large. This lead to net cooling. For an optically-thin cloud over a fairly warm surface, the cloud never became black and warmed throughout. This heating depended on the particle size distributions which were parameterized.

Flatau et al. stated that their entrainment constants and turbulent fluxes were educated guesses requiring more observational study. They also didn't allow any feedback with the microphysics.

Their results showed clouds growing upward in the case of warming and downward in the case of cooling. The mixed layer assumption did not stop the growth through precipitation, a decrease in optical thickness, the presence of a strong inversion, large scales subsidence, evaporation of particles or solar heating.

Flatau et al.'s motivation for this model was to derive some information on the persistence of cirrus clouds for use in GCMs. From their model, this information can be determined on the basis of only field variables.

Dalu et al. (1990) used mixed layer theory to describe the horizontal variability and structure of cirrus (Sassen et al., 1989) as a interaction between the mixed layer and vertically propagating gravity waves. Dalu et al. suggested that the horizontal structure was due to a complex combination of mixed layer depth and the locations of the gravity wave sources. Depending on the depth, waves would be transmitted or ducted and their vertical motions would enhance or deplete the cirrus cloud. The ducted waves could then be reflected several times, creating a variability in the horizontal structure. A critical layer above the cirrus layer could enhance this effect. Dalu et al. also showed that latent heat release as a result of the gravity wave vertical velocity could produce a secondary convective circulation which could enhance or weaken the cloud.

2.3.3 Convective Outflows

Cirrus created by outflows from cumulonimbi or mesoscale convective systems (MCS) are easily identified on satellite imagery. No large scale uplift is necessary, only moisture and hydrometeor injection into the upper tropopause. These clouds are capped by the stable layer that created the outflow initially, usually the tropopause. Note that mesoscale ascent is associated with MCS outflows but usually not with individual cumulonimbus.

2.3.4 Jet Stream Cirrus

Conover (1960) suggested that cirrus clouds may be driven by vertical motions created by horizontal vortices due to the jet stream (longitudinal rolls). These clouds are observed to parallel temperature discontinuities and are probably capped by the tropopause.

Ciesielski et al. (1989) produced evidence that some cirrus aligned across the jetstream may result from asymmetric inertial instability. They observed propagating wavelets along the anticyclonic shear side the cirrus canopy associated with a strong subtropical jet.

2.3.5 Cloud Scale Models

Starr and Cox (1985a) created a cloud-scale model specifically to simulate cirrus clouds. They created a two dimensional (x,z), Eulerian model with 100 m resolution in both directions and a 30 second timestep. They parameterized the phase change of water, radiative

processes, the microphysics and vertical flux of ice water. They based their parameterizations on observations when possible but were restricted to -25^oC to -45^oC, weak large scale vertical motion, and no vertical shear of the ambient flow. This last restriction limited their ability to simulate cirrus uncinus which are observed in regions of strong shear (Heymsfield, 1975b).

Their results were realistic, matching observations of ice water content and vertical motions. They also reproduced the horizontal scale between convective cells and the tendency for layering.

In later simulations (Starr and Cox, 1985b), they ran sensitivity experiments to determine the effects of radiation (day vs. night), the magnitude of the large scale vertical motions, and microphysical structure. They found that the large scale ascent or descent was critical in determining the physical properties of the cloud, but noted that by changing the microphysical properties (through the parameterized ice crystal fall speed) they could affect large changes as well. In fact, 80% of the ice water content was lost due to precipitation. Radiation was determined to play a significant role in the modulation of local buoyancy. The day case appeared more cellular but less dense.

Starr (1987) ran simulations with the cirrus at much colder temperatures (-60^oC), outside of his parameterization restrictions, and compared these to lower level cirrus (-35^oC) for day and night cases. The results for the cold cirrus were comparable to observations despite the fact that the original parameterizations were developed from data from warmer cirrus. Starr concluded that radiative processes strongly regulated the cloud ice water budget and structure of convective thin cirrus. Again, night time cirrus were found to be 30% more dense. This is roughly 3 times as large a difference as would be expected due to temperature changes in the saturation vapor pressure. He also stated that there were corresponding differences in the convective circulations.

2.3.6 Mesoscale Models

Nicholls et al. (1990) applied a nested grid regional scale model to a day during the FIRE Cirrus IFO in an attempt to reproduce the larger scale features of the extensive cirrus

13

present on that day. The smallest grid had 15 km horizontal resolution and 500 m vertical resolution.

In spite of the coarse vertical resolution, the results were encouraging. They were able to simulate cirrus of the appropriate IWC, vertical position and extent, and the bulk of the horizontal extent. The model produced some layering.

However, they were unable to reproduce the cellular activity after the passage of a short wave disturbance. Vertical resolution prevented them from reproducing a thin cirrus layer at 11.3 km reported to be 200 m thick. This study is an extention of that research.

Chapter 3

RAMS

3.1 Description

The RAMS is a combination of a non-hydrostatic cloud model (Cotton et al., 1982; Tripoli and Cotton, 1980; Tripoli and Cotton, 1982; Tripoli and Cotton, 1989) and two hydrostatic mesoscale models (Pielke, 1974; Mahrer and Pielke, 1977; McNider and Pielke, 1981; McCumber and Pielke, 1981; Tremback et al., 1985). The resultant code is a highly flexible and modular program with many possible configurations. The following is a brief description of the configuration used in this modeling study.

3.1.1 Variables

Any numerical model is a mathematical description of a set of conservation principles. Conservation of mass, momentum, heat and water-substance should all be maintained by accounting for all important sources and sinks. These conservation equations, when coupled with the equation of state, are a closed set of partial differential equations that can be numerically- integrated in time. The partial differentials are approximated on a grid using a variety of schemes with varying amounts of accuracy.

The non-hydrostatic version of RAMS predicts u, v and w wind components, ice/liquid water equivalent potential temperature θ_{il}, dry air density, total water mixing ratio, and the mixing ratios of the various water variables. From these variables, pressure, potential temperature, temperature, vapor mixing ratio and cloud water mixing ratio can be diagnosed.

3.1.2 Grids

RAMS uses the standard Arakawa-C grid (Arakawa and Lamb, 1981) which is staggered in both vertical and horizontal directions. Scalar variables are defined at the center of each grid volume. Velocity components are defined on the faces of the grid volume.

Version 2B of RAMS utilizes a polar-stereographic horizontal grid. This grid structure eliminates the problems inherent with latitude/longitude grids.

The vertical coordinate is the σ_z terrain following system (Gal-Chen and Somerville, 1975). Vertical grid spacing is allowed to change according to the user's specifications.

3.1.3 Numerical procedures

The numerical procedures of the non-hydrostatic model are described in Tripoli and Cotton (1982) and Tripoli (1988). This version uses the leapfrog time differencing with an Asselin filter and a timesplit scheme (Klemp and Wilhelmson, 1978) to integrate the acoustic terms on a short time step and all other terms on a long time step. This study used the second-order advection scheme.

3.1.4 Parameterizations

RAMS is used for a wide variety of research projects each concerned with a different meteorological phenomena. It is a tribute to the flexibility of RAMS that it is configured for synoptic scale investigations of cirrus clouds as well as cloud scale investigations of tornado genesis. Since most parameterizations are not this flexible, the RAMS user must choose the parameterization most suited to his/her simulation.

Turbulence

This study used the deformation K turbulence scheme described in Tripoli and Cotton (1982), and in Tremback (1990). The scheme is similar to the Smagorinsky (1963) scheme with some modification (Lilly, 1962; Hill, 1974). Several parameters must be set in the RAMS formulation of this scheme. The vertical scale length was set to the vertical grid spacing. Three dimensional deformation was used to calculate the vertical eddy exchange coefficients. Adjustments to the vertical exchange coefficients were made using a Richardson number/moist Brunt-Vaisalla frequency factor. The horizontal scale length was set to

$\sqrt{\Delta x \Delta y}$. The horizontal exchange coefficients were calculated from only the horizontal deformation. The ratio of the eddy heat exchange coefficient to the eddy momentum exchange coefficient was set to three for both the horizontal and vertical.

Surface layer/Soil model

The Louis (1979) surface layer scheme was used in this study. In addition, a prognostic soil model was used (Tremback et al., 1985).

Microphysics

One of RAMS unique features is the Cloud Microphysics Module (CMM) (Flatau et al., 1989). The CMM simulates nucleation, growth, collection and precipitation processes for pristine ice crystals, snow, aggregates, graupel and rain. It also simulates all but precipitation for cloud water. With this code, overall effects of microphysical processes can be modeled and investigated.

For this study of high level ice clouds, pristine ice, aggregates, rain and cloud water were activated. Both the concentration and mixing ratio of pristine crystals were predicted while the concentrations of aggregates, rain and cloud water were diagnosed assuming a characteristic diameter.

The CMM was not originally designed for simulating cirrus clouds, but the basic processes are available. Pristine crystals are considered to be in a mono-dispersed size distribution with the characteristic diameter diagnosed from the predicted concentration and mixing ratios. The crystal nucleation scheme is described in Meyers et al. (1991).

Nucleation results from two primary processes:

- A combination vapor deposition and condensation/freezing mechanism where the number of activated nuclei is derived from the amount of supersaturation with respect to ice.

- Contact nucleation where the number of potential nuclei is derived from an observed temperature dependence.

Growth is through vapor deposition computed for hexagonal plates. The terminal velocity of the crystals is then computed based on the characteristic diameter. Crystals can aggregate, melt into rain drops and evaporate.

This treatment provides most of the known processes in ice clouds and as will be shown in Chapter 5, leads to a very realistic simulation of a cirrus cloud system. Important features missing are the handling of different particle sizes in the same grid box, the inclusion of a homogeneous freezing mechanism for crystal nucleation and the addition of different geometries for depositional growth.

Radiation

The radiation scheme employed in this study is described in Chen and Cotton (1983b). This scheme considers the influence of water vapor, ozone, carbon dioxide and condensate on shortwave and longwave radiative transfer. The scheme does not treat the various hydrometeor species differently. Rather it calculates condensate effects based on the predicted total mixing ratio minus the saturation vapor mixing ratio. Thus ice and water are treated alike and no consideration is given to the effects of ice crystal geometry or particle size distributions.

3.2 Development of the Top Boundary Condition

The non-hydrostatic model described above does not provide a radiative top boundary condition when used with a horizontally inhomogeneous initial field. The only choice for simulations using variable initialized fields was the "wall on top" condition where w is set to zero. This condition is known to be completely reflective. Some damping mechanism had to be formulated or adapted to the model.

3.2.1 Wall

The only top boundary condition available set w to zero at the model top. Without a damping layer, this is completely reflective and is unsatisfactory for this study.

3.2.2 Viscous Layer

One type of damping layer is the viscous layer used by Klemp and Lilly (1978). This method absorbs wave energy by increasing the diffusion coefficients in a layer at the model top. By changing the diffusion coefficients and the depth of the layer, the damping can be adjusted for different wavelengths.

When using the deformation K scheme, diffusion can be increased by simply increasing the eddy exchange coefficients. The increased value is based on a user determined dissipation time scale and the stability criteria for diffusion. This then decreases linearly with height from the bottom of the viscous layer to the model top. The criteria for stability is simply that the dissipation time be less than a model time step.

$$K = \frac{\Delta x^2}{8\Delta t}(\frac{z - z_b}{z_t - z_b}) \tag{3.2.1}$$

In this equation, K is the eddy exchange coefficient, z is the height of the model grid point, z_t is the height of the model top, z_b is the height of the bottom of the diffusive layer, Δx is the model horizontal grid spacing, and Δt is the user set dissipation time. The user sets the depth of this layer by specifying the number of model levels from the model top where the enhanced viscosity will be activated.

3.2.3 Modified Rayleigh Friction

Rayleigh friction is a damping mechanism where model variables are nudged back to a reference state (Clark, 1977). For homogeneous cases, this is very effective, but for variable initial fields it will nudge back to a reference state that is different from the initial fields,thereby producing artificial gradients.

An alternative approach,suggested by Dr. William R. Cotton and described in Cram (1990), is to nudge toward an horizontal running average. By adjusting the number of points in the average, the scale of the damping can be altered.

For a given variable χ, the tendency for the damping scheme is calculated using the following relation where $\bar{\chi}$ is a horizontal running average over a user specified number of points in both the x and y directions.

$$\frac{\partial \chi}{\partial t} = \tau(\chi - \bar{\chi}) \tag{3.2.2}$$

$$\tau = \frac{1}{\Delta t}\left(\frac{z - z_b}{z_t - z_b}\right) \tag{3.2.3}$$

In the unmodified scheme, $\bar{\chi} = \chi_0$. All other variables in these equations are the same as those described in the previous section. For the tests run here, the horizontal average was calculated over five points in both the x and y directions.

3.2.4 Damping Response

To determine the damping response of each as a function of wavelength, a unit amplitude sine wave was generated and then damped once. The resulting amplitude determined the damping efficiency for that wavelength. This exercise was completed for a range of waves and for a range of averaging points. The results are in Figures 3.1a- 3.1b for the diffusive damping and friction damping, respectively. Note that the figures are alike for ease of comparison even though there is no change across the abscissa of the diffusive damping response curve. Also note, however, the prefered wavelength of damping for the friction curve. There appears to be a more or less linear change with the number of averaging points selected. Although a smooth response is preferred, this is adequate. The friction is a rather strong damper for all wavelengths while the diffusion is negligable after only $5\Delta x$. This is a useful wavelength dependence but cannot be adjusted.

3.3 Testing of Top Boundary Condition

3.3.1 Linear mountain wave

Using the example of Klemp and Lilly, two dimensional linear mountain wave simulations were run to compare the two damping layers. This test allows for direct comparison with analytical results.

The conditions for the simulations were as follows:

- Initially isothermal at $250^o K$ with a constant horizontal wind speed of $10 m/s$.

- Bell shaped mountain with a maximum height of $10 m$ and a half width of $10 km$.
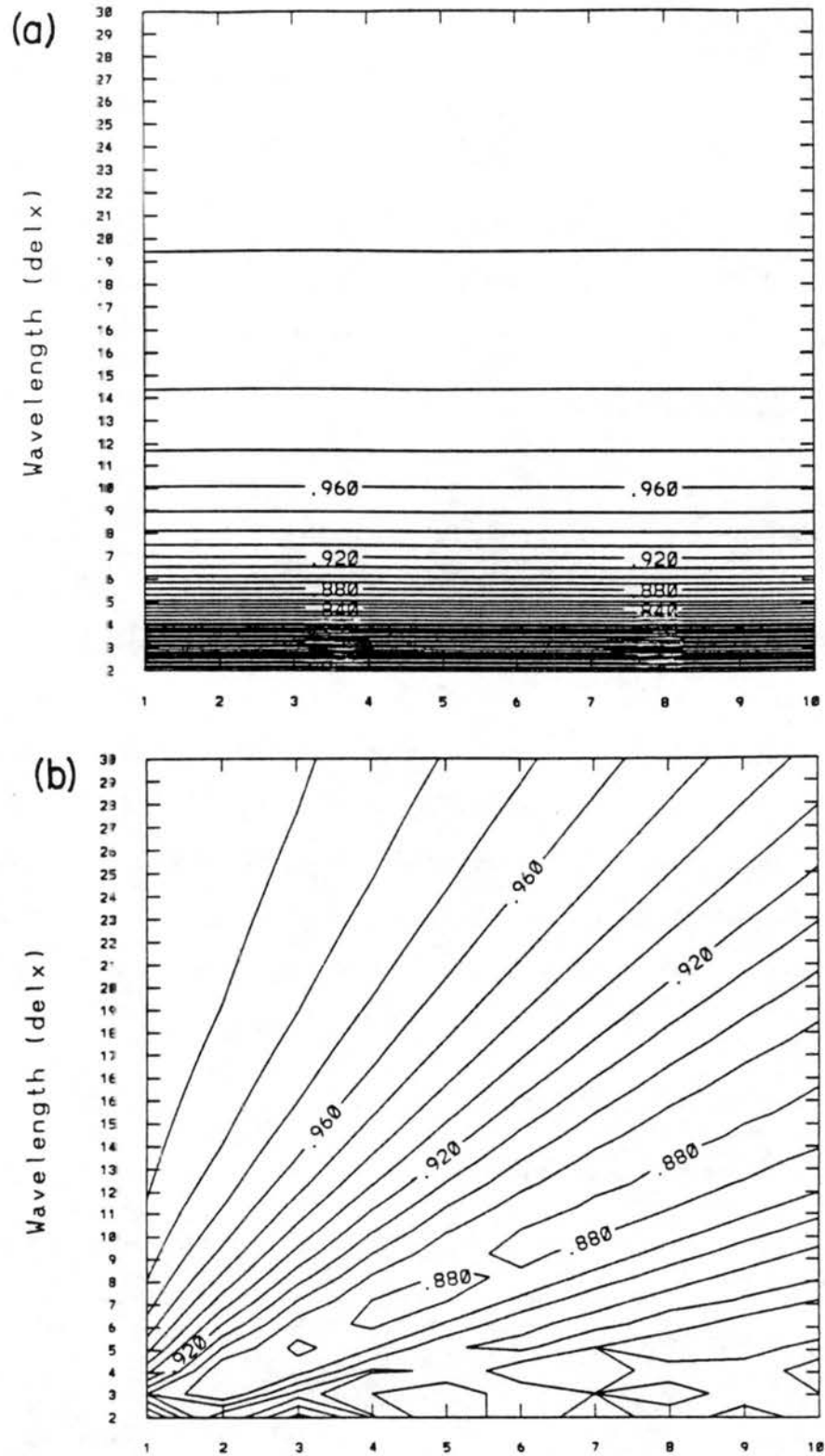
Figure 3.1: Damping response for (a) the viscous method, and (b) the modified Rayleigh friction method.

- 82 vertical grid points with $250m$ spacing to $20km$.

- 62 horizontal points with $2km$ spacing.

- The damping layers extend 20 points from the model top to $15km$.

The simulations were integrated to 24 hours.

Vertical motion profiles

The simulated vertical motion fields are shown in Figures 3.2a–3.2c. From these figures, it appears the modified Rayleigh friction scheme is damping more effectively. The vertical motion is effectively eliminated far away from the model top. The viscous layer damping is not as effective. The control run without the damping layer shows a chaotic vertical motion field indicative of complete reflection.

RMS error from linear solution

From Durran's (1986) treatment of the mountain waves, the analytic vertical velocity field may be derived from the wave equation assuming a radiative top boundary condition and taking the hydrostatic limit.

In spectral space,

$$\hat{w}(k, z) = ik\bar{u}\hat{h}(k, z)e^{ilz} \tag{3.3.1}$$

where $\hat{w}$ is the vertical motion in spectral coordinates, $\hat{h}(k, z) = h_0 a e^{-ak}$ is the spectral representation of a bell shaped mountain. h_0 is the maximum height and a is the distance from the center at which the height is $1/2$ the maximum.

After transferring back to physical space:

$$w(x, z) = \sqrt{\frac{\bar{\rho}_0}{\bar{\rho}}} \frac{\bar{u} h_0 a}{(a^2 + x^2)^2} (-2ax \cos lz + (x^2 - a^2) \sin lz), \tag{3.3.2}$$

where $\sqrt{\frac{\bar{\rho}_0}{\bar{\rho}}}$ is a density factor and, for the isothermal case it becomes $e^{\frac{g-R\gamma}{2RT}z}$.

The result is shown in Figure 3.3.

Root mean square (RMS) error from the analytical solution was calculated and plotted. RMS error below the damping layer is shown in Figures 3.4a–3.4c for all three cases. This error was then summed in the horizontal and plotted in Figure 3.5 as a function of height

Figure 3.2: Steady state vertical motion at 24 hours for the case of (a) no damping layer, (b) viscous damping layer, (c) modified Rayleigh friction layer.

for each case. This error reveals the total and partial reflection of the wave energy by the top boundary. The control case errors confirm the complete reflection evident in the vertical motion fields. The viscous layer error results show partial reflection, not evident in the vertical motion field. All cases show relatively large errors in the center of the wave.

This error analysis seems to show that the strong damping of the modified Rayleigh friction scheme results in much less reflection in this greatly simplified case.

Vertical momentum flux profiles

At 24 hours, a profile of the vertical flux of horizontal momentum for the linear mountain wave solution was calculated. From the analytic solution, this value should be constant with height (Klemp and Lilly, 1978),

$$M = \frac{\pi}{4}\rho_0 N \bar{u} h_0^2, \tag{3.3.3}$$

where ρ_0 is the constant density, N is the constant Brunt-Vaisalla frequency, $\bar{u}$ is the constant horizontal flow, and h_0^2 is the height of the mountain squared.

Vertical profiles were plotted as a percent of the theoretical value for both damping layers and the control simulation in Figure 3.6. The resulting values are near the theoretical value but exhibit a distinct wavy pattern as well as decreasing with height. The decrease in accuracy with height can be blamed partially on the inability to make the model initialized atmosphere truly isothermal. Because of initial interpolation, the atmosphere showed a $0.4^o K$ increase near the model top. Klemp and Lilly blame the wavy pattern on the vertical differencing's inability to conserve momentum.

The damping layers appear almost equal in this test. The viscous layer is closer to the theoretical value near the surface but the friction layer does better at the base of the damping layer.

3.3.2 Nonlinear mountain wave

Linear mountain waves are small amplitude, generating vertical motions of $3cm/s$. Since the viscous layer appeared to be partially reflective to this small wave, a more vigorous test was run to determine how it would react to stronger vertical motions. The friction
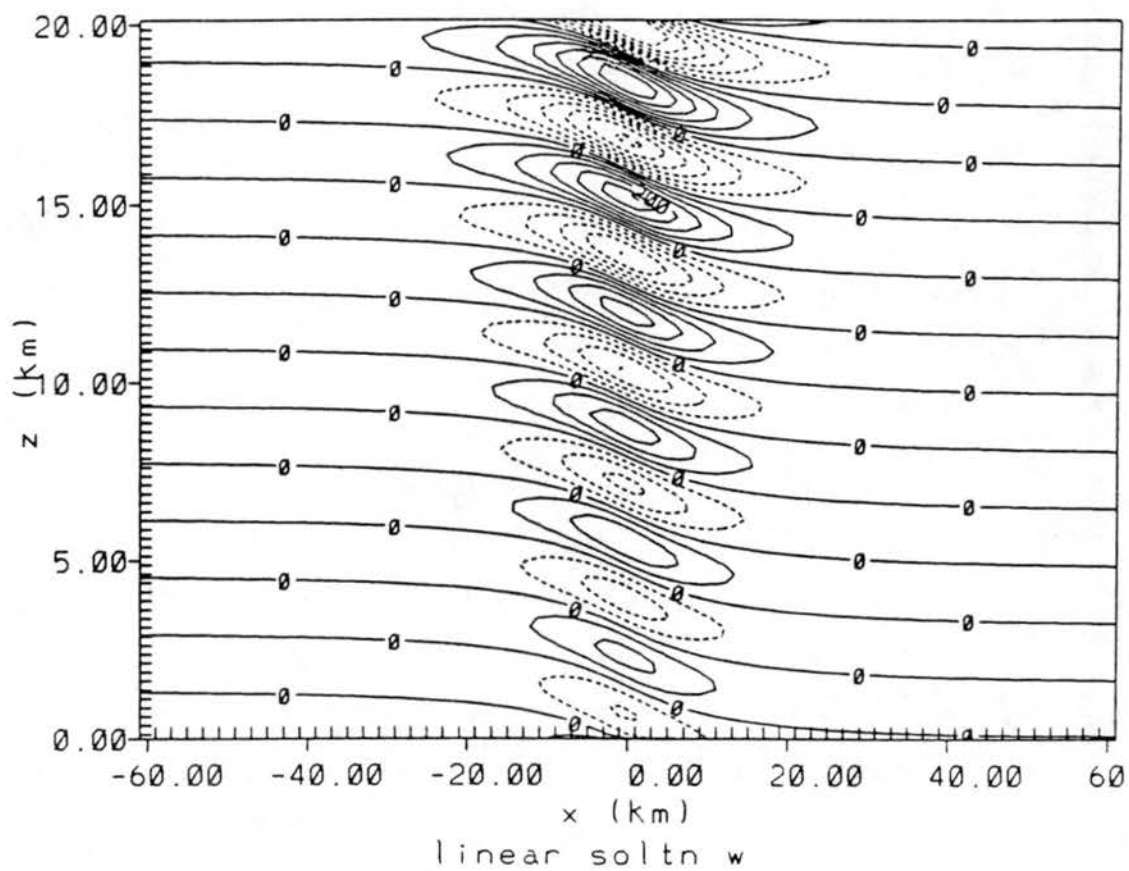
Figure 3.3: Analytical solution vertical motion on the model grid.
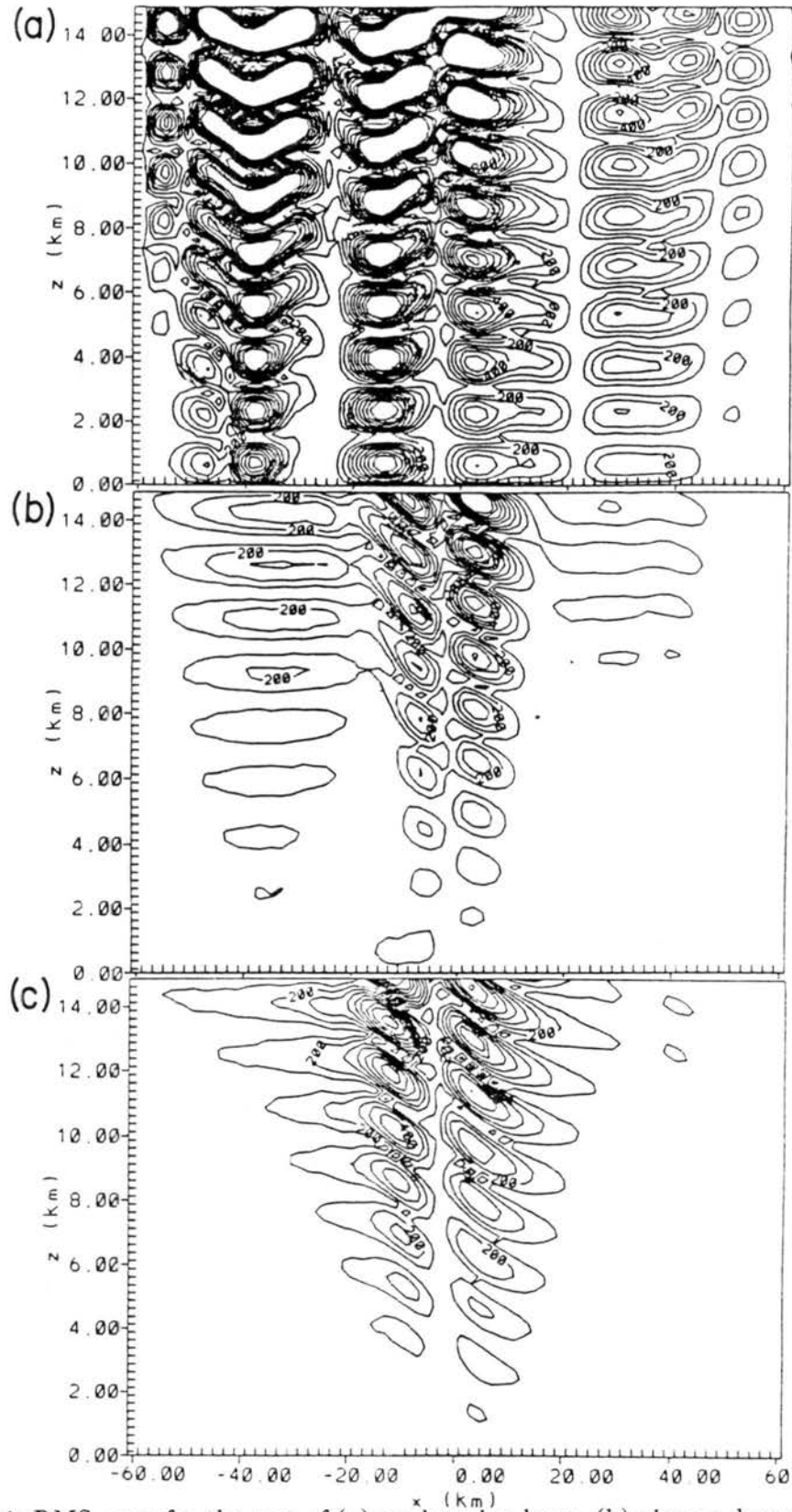
Figure 3.4: RMS error for the case of (a) no damping layer, (b) viscous damping layer, (c) modified Rayleigh friction layer.
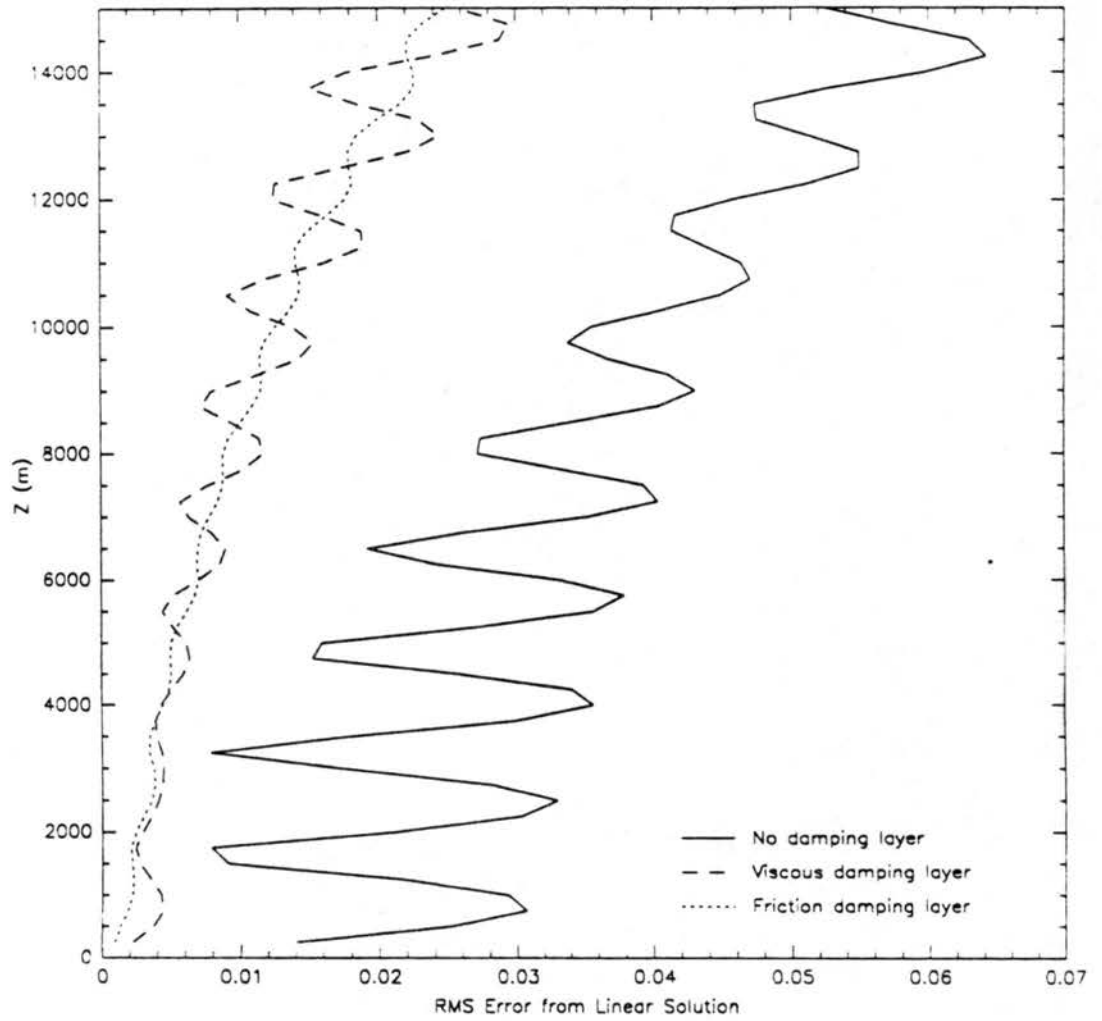
Figure 3.5: RMS error summed horizontally for all cases.
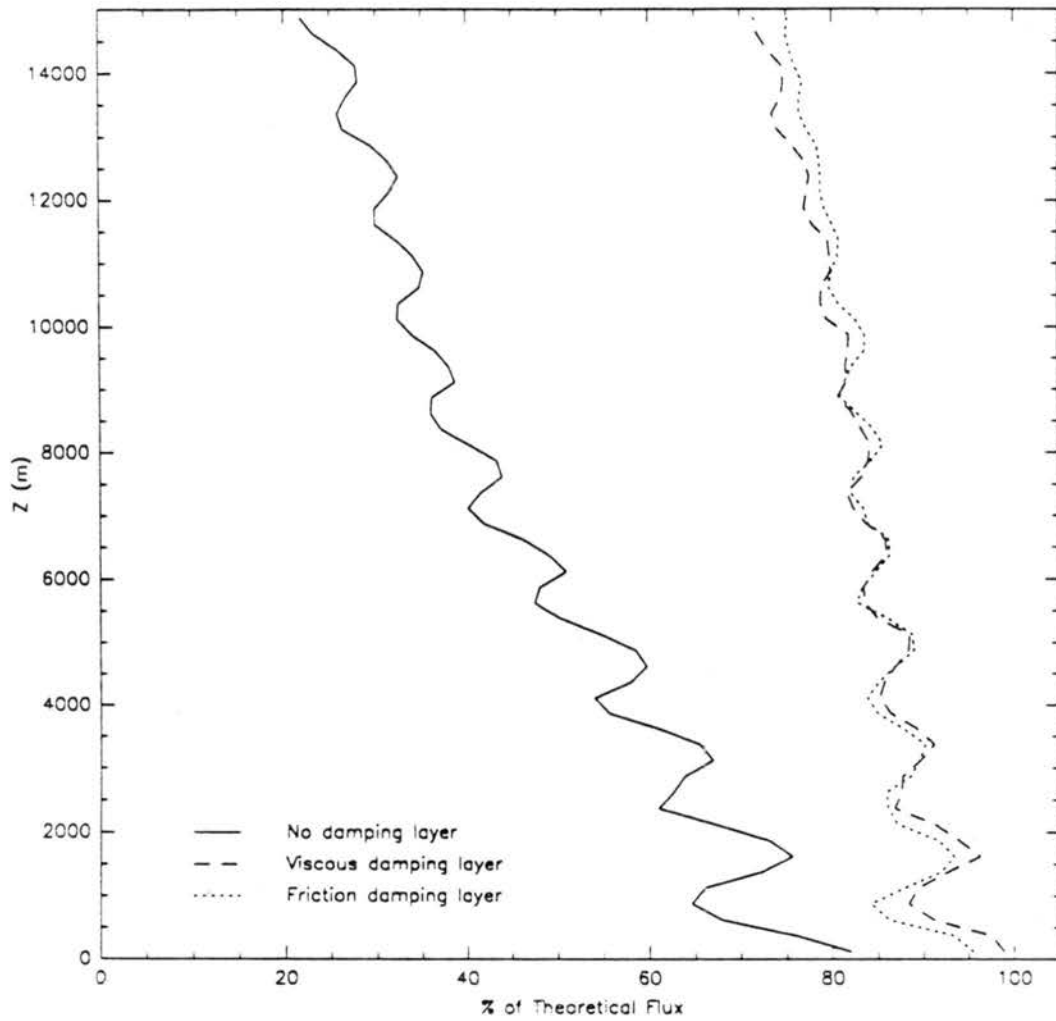
Figure 3.6: Vertical profiles of the vertical flux of horizontal momentum.

layer's strong damping for many wavelengths would appear to make it better suited for more vigorous vertically propagating waves. To test this hypothesis, non-linear mountain wave simulations were run. Since no analytical solutions were readily available, judgements were made on the appearance of the vertical motion field.

The test was run with the following changes to the linear case.

- Wind speed constant at $20m/s$.

- $1km$ bell shaped mountain with $50km$ half width.

- $5km\Delta x$.

This resulted in a 40 fold increase in maximum vertical velocities and a change to the vertical wavelength.

Klemp and Lilly (1978) show that linear and non-linear cases are very similar except for the amplitude of the perturbations.

The 24 hour vertical motion fields, shown in Figures 3.7a- 3.7b, for both the viscous and friction layers display strong similarities to their linear test counterparts. The friction layer motion pattern appears less distorted than that for the viscous layer. This is to be expected because viscosity damps $2\Delta x$ waves most while virtually ignoring all others. The wave in this test is on the order of $20\Delta x$. In contrast, the friction damps these wavelengths approximately 4% every time step.

3.3.3 Synoptic case

The point of this exercise was to create a non-reflective upper boundary condition for use with variably initialized mesoscale simulations; specifically of cirrus clouds. Synoptic scale tests would determine the model solution's sensitivity to these upper boundaries when used in a case study simulation.

Three simulations were run for the first 12 hours of the 28 Oct 86 case study day. The control run had no damping layer. The viscous and friction layers in the other runs were made eight points deep.

The $300mb$ height, temperature, humidity and wind speed fields were chosen for comparison between the runs. This height was chosen because it is at cirrus cloud level while
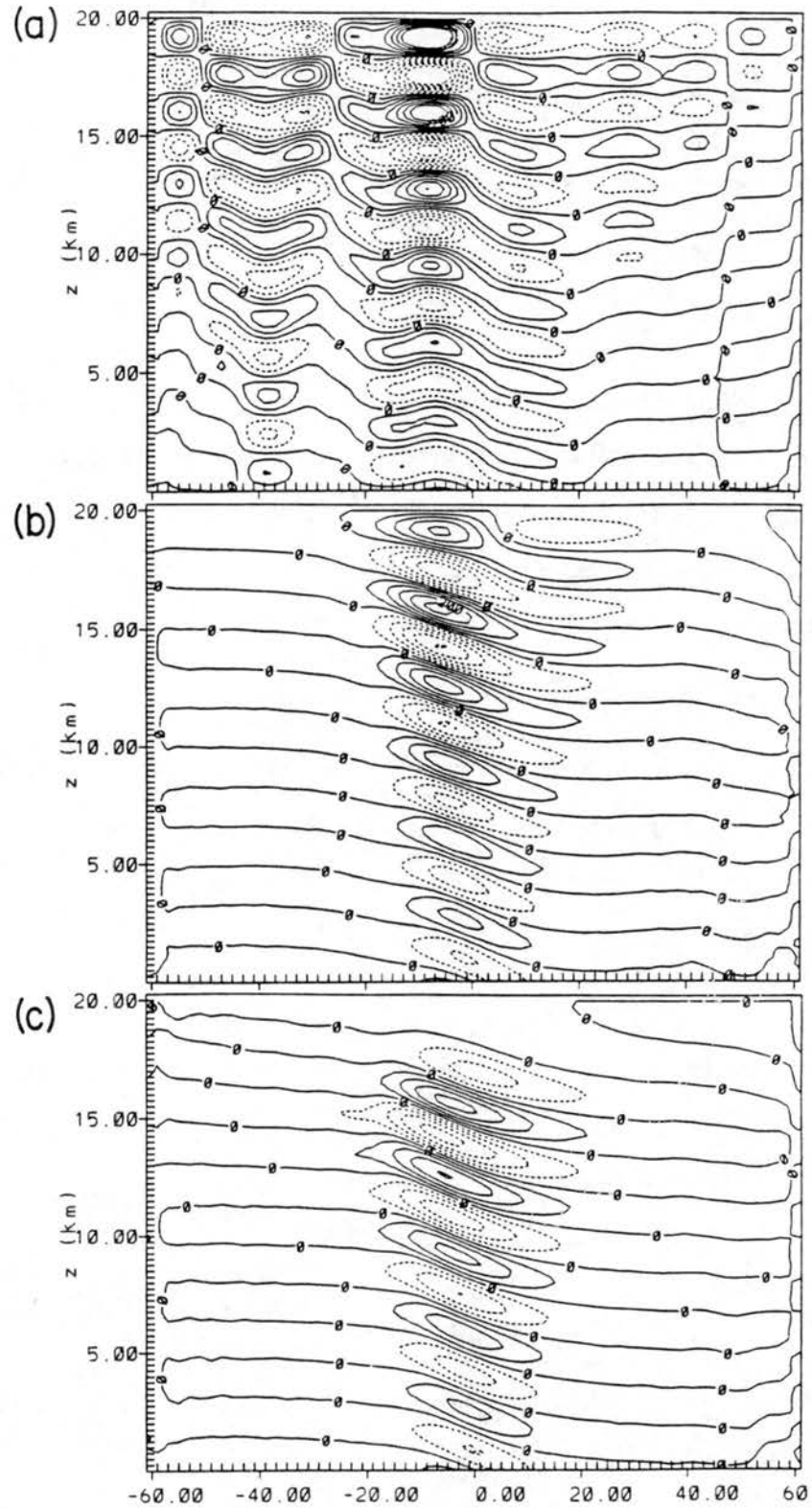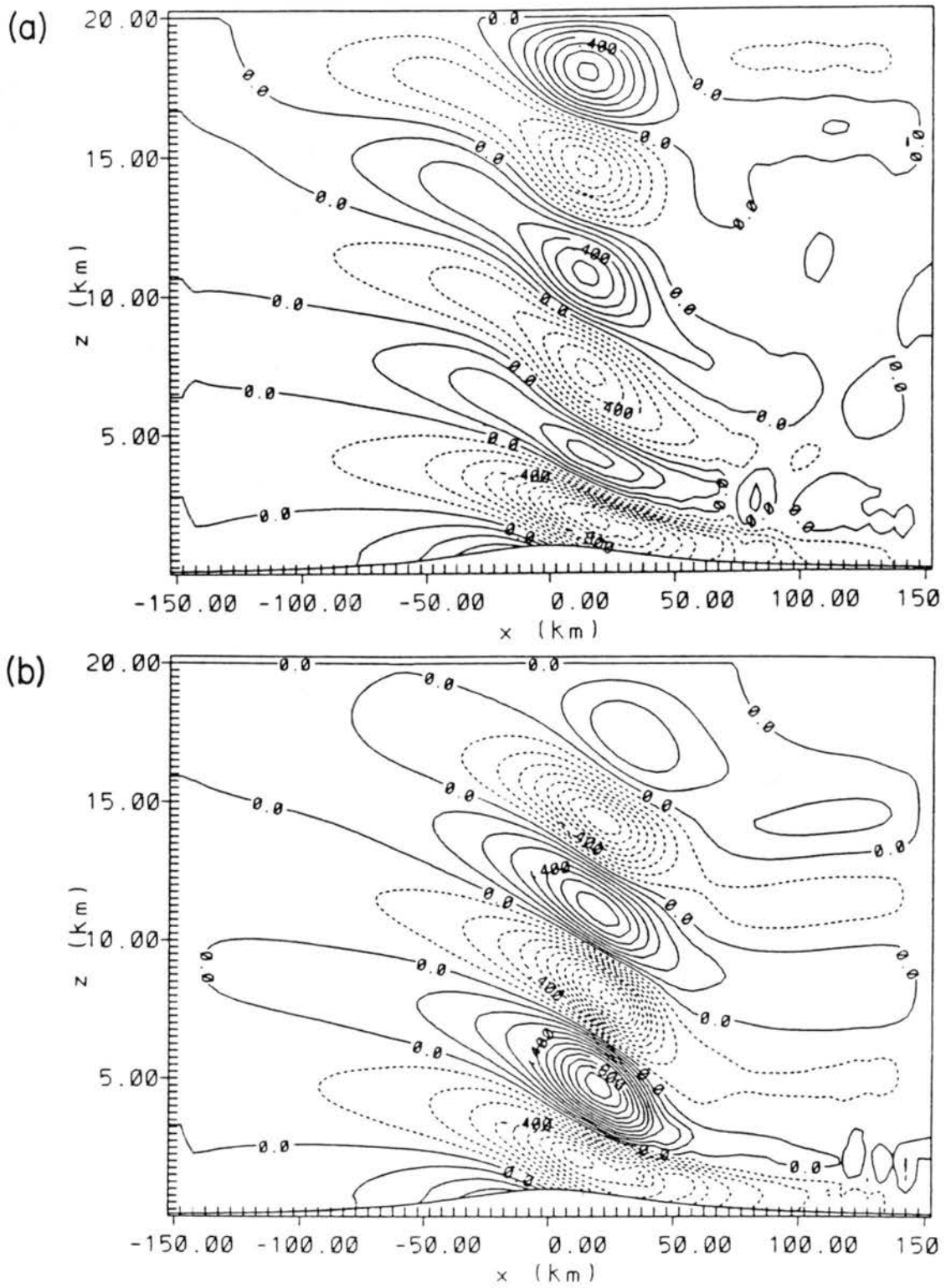
Figure 3.7: Steady state vertical motion at 24 hours for the case of (a) viscous damping layer, (b) modified Rayleigh friction layer.

remaining in the troposphere. The various fields were chosen because they could be readily verified against standard rawinsonde data. In addition, $300mb$ vertical motion was compared because it is the field most likely affected by the top boundary and it could be verified against ECMWF archived data. Finally, the ice water path (LWP) integrated from $6-12km$ was used to describe the upper level clouds. This value provides a first order approximation to the satellite observed infrared radiance field. The details of this calculation are left to the verification section in Chapter 5.

For this synoptic case, broad flow was perpendicular to the continental divide through a deep layer, providing mountain wave energy.

The dynamic field comparisons showed almost no difference after 12 hours. Clearly the upper boundary condition had no effect on the evolution of the large scale features present on this day. There is so little difference, no figures will be presented.

The vertical motion fields showed somewhat more variation between runs, but still very little. No pattern was better than the others in terms of comparing to the ECMWF analysis. Magnitudes and locations are very similar.

The ice water path calculations for the high clouds in Figures 3.8a- 3.8c show very little difference between runs. The clouds, then, appear not to be sensitive to reflections off the model top at least for this case.

3.3.4 Discussion

From this test, the model solution in this synoptic case does not appear to be sensitive to the upper boundary condition. There are two possible explanations. First, the vertical motions near the model top at $19.2km$ are very small, only $1-2cm/s$. Second, the eight points used in the damping layer for the synoptic study may not be enough to effectively damp the motions. Vertical cross sections of vertical motion for the three cases are shown in Figures 3.9a- 3.9c show that the vertical motions are indeed very small near the top boundary.

These figures do not show any significant reflection from the top boundary, suggesting that vertically propagating wave energy was small in this case. The modified Rayleigh friction scheme added approximately 6% to the total cost of the simulation while the viscous
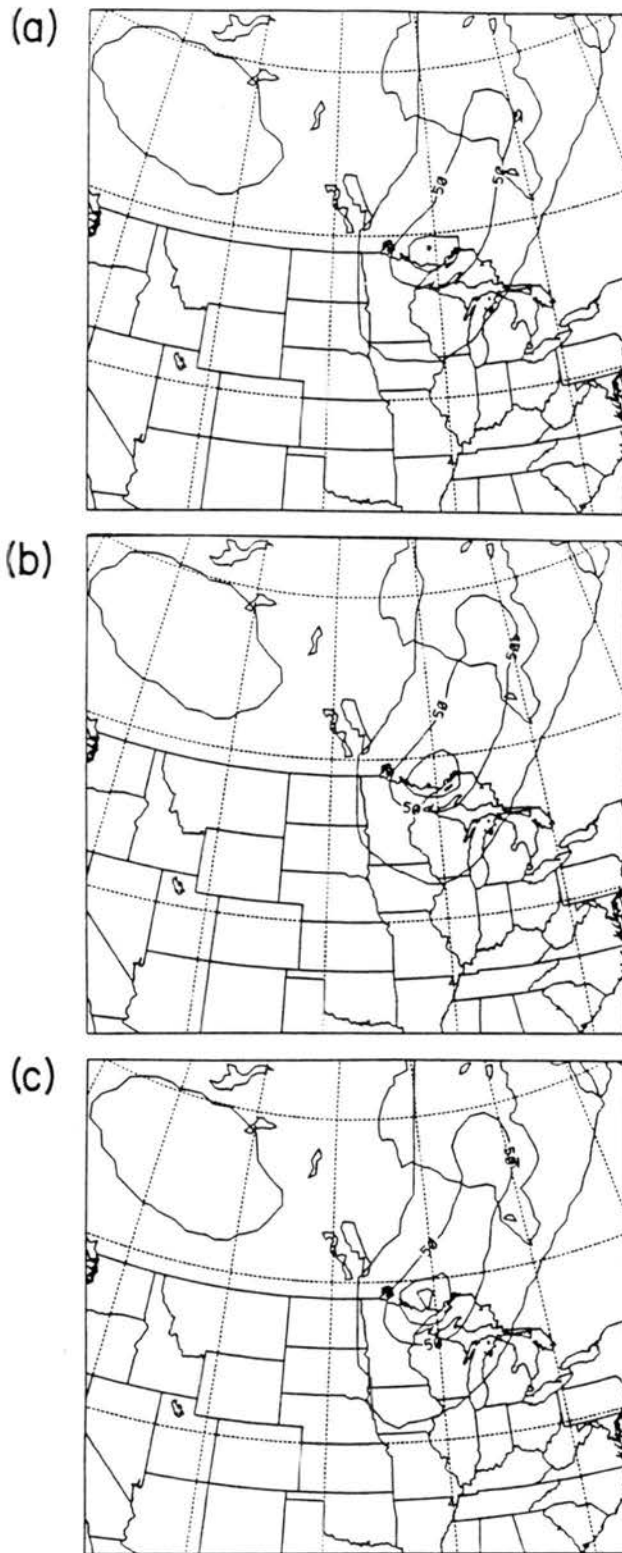
Figure 3.8: Model predicted ice water path at 1200 UTC for the simulation (a) no damping layer, (b) viscous damping layer, (c) modified Rayleigh friction layer.

layer added less than 1%. Although the modified Rayleigh friction scheme seemed to be the better damper in mountain wave studies, these synoptic tests showed it not to be necessary in this case. The "wall on top" is still unacceptable, even though the results were not unreasonable. Therefore, the viscous layer was used for the case study simulations.
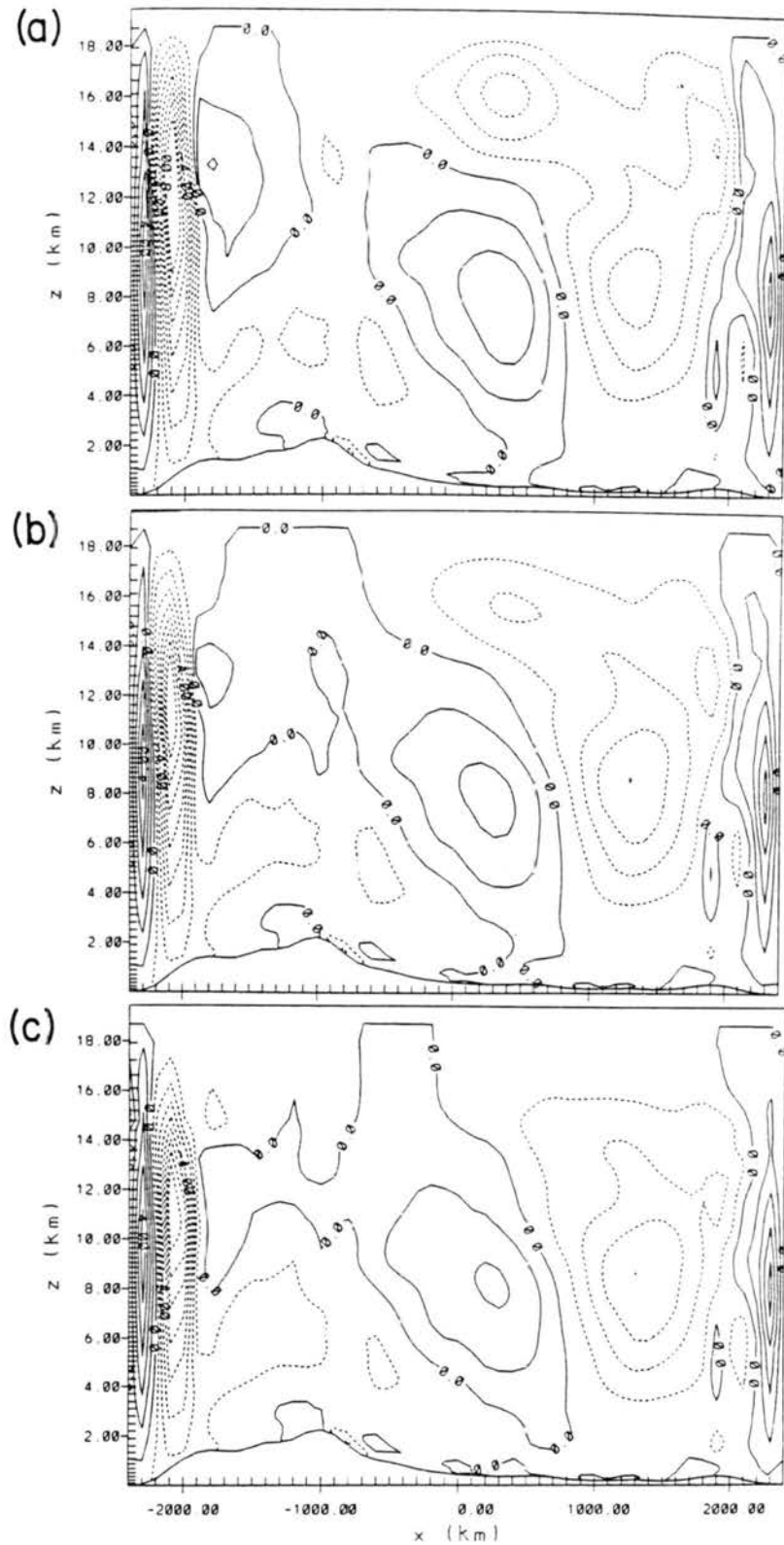
Figure 3.9: Vertical motion (cm/s) at 1200 UTC in east-west crossection for the simulations with (a) no damping layer, (b) viscous damping layer, (c) modified Rayleigh friction layer.

Chapter 4

28 OCTOBER 1986

For this case study, the primary concern is scales of motions that are well represented by the model grids. Synoptic scale flow is represented by a 100km horizontal resolution coarse grid covering most of the United States and Canada. Mesoscale features are simulated on a 33km grid nested over Wisconsin, Minnesota and the Great Lakes. See Chapter 5 for exact locations.

The weather events of 28 October 1986 are discussed by separating the broad scale flow, measured at 12 hour intervals, from the mesoscale events over Wisconsin, which are measured at 3 hour intervals. Maps, soundings and satellite imagery are divided in this manner.

The chapter first describes the data sets used and any processing required. The synoptic scale flow patterns of the entire 24 hour period are discussed. And finally, the mesoscale features over Wisconsin are described for the period between 1200 UTC and 0000 UTC. Because of the volume of data, the analyses shown will be limited to those deemed most representative of the overall circulation. References will also be made to Starr and Wylie's (1990) discussion of the same subject.

4.1 Observational Data

Surface and upper air observations from the NMC archived data sets at NCAR were retrieved and plotted using the NCAR graphics CONRAN plotting/contouring routine. All available upper air observations were used. Surface observations were eliminated based on a 0.5^o station separation. Approximately 100 upper air soundings and 750 surface observations were retrieved for the maps in this chapter.

Temperature, relative humidity, wind speed and direction, and height were plotted on mandatory level pressure surfaces. In addition, vertical motions from the WMO archive of the ECMWF model were plotted to provide insight and a means of verificiation. Although the data sets do not match exactly, they are close enough to give an idea of the synoptic scale flow patterns. This data set also substituted for 300 mb relative humidity observations which are not kept in the NMC archived soundings because of the known accuracy problems with humidity measurements made below $-40^{o}C$.

Satellite images were collected as part of the ISSCP global collection program and as part of the FIRE IFO itself. Images were taken off tape at the CSU satellite ground station and displayed.

The infrared (IR) images are from GOES channel 8 and the raw data has been gridded to 10 km resolution. The maximum resolution for GOES IR, at the equator, is 4 km by 8 km. These images provided a more than adequate picture of the cloud system being studied. Figures A.1- A.5 show the time evolution of the cloud system at 6 hour intervals.

For the mesoscale analysis, higher resolution and some processing was required. This cloud study required detailed knowledge of cloud height and type. Infrared imagery displays cloud top temperature but can be fooled by low-lying clouds with temperatures equal or warmer than the Earth's surface. Cloud height can be deduced from visible images only at low sun angles. By combining the two channels on the same image, more height information can be retrieved. Visible data, displayed at roughly 2 km by 2 km per pixel resolution is assigned to the green and red colors of the display. The infrared is displayed in differing intensities of blue. The result: cold, dark clouds (cirrus) appear with a bluish tint; warm, bright clouds (stratus,fog) appear yellow. Warm, dark areas (earth's surface) appear brown. Although this is a rather simple visual technique, it is roughly the same idea used in the ISSCP retrieval techniques and is similar to that described by Minnis (1990).

The resulting images are much more useful in determining cloud type, height and location. Figures A.6- A.10 display clouds over the FIRE IFO region during daylight hours. Data from 1500 UTC to 1900 UTC could not be obtained.

4.2 Synoptic features

4.2.1 Surface

The upper midwest region of the United States was under the influence of a Canadian low pressure system that began just north of North Dakota at 0000 UTC and gained strength while progressing northeastward over Hudson Bay by 0000Z on the 29th. This system had a weak cold front extending into eastern Montana and western Wyoming. A weak warm front extended to the north of Lake Superior. See Figure 4.1.

As the system strengthened and moved away, the cold front and the associated pressure trough moved into northwestern Minnesota by 0000 UTC and into southeastern Wisconsin by 00Z on the 29th. Low clouds and light rain were reported in Minnesota and northern Wisconsin late in the period. The front displayed a marked wind shift but very little temperature gradient or dewpoint gradient.

4.2.2 · Upper air

Associated with the surface system, a $500mb$ shortwave trough developed and deepened. The trough axis moved from western Montana to western Wisconsin during the period. This developing wave had strong cold air advection behind the axis and moderate warm air advection ahead at 0000 UTC on the 28th. The cold air advection continued at the trough axis through out the period. The differential advection strengthened the temperature gradient associated with the trough to produce a frontal zone that included a weak confluence line at the leading edge. This frontal boundary stayed to the northwest of the surface front, in the cold air. Inspection of the 850 and $700mb$ temperature fields (not shown) shows similar zones of strong horizontal gradient that support the argument that these zones are indeed connected to the surface front. Figure 4.2 shows the $500mb$ temperatures and winds.

At $300mb$, a weak troughing existed over Idaho at 0000 UTC on the 28th. The trough deepened slowly and was over western Minnesota by 0000 UTC on the 29th. The downstream ridge axis passed over Wisconsin by about 1500 UTC. The jet flow was fairly uniform around the base of the trough, increasing to $35m/s$. The exit of this jet made it's way into

Figure 4.1: Sea Level pressure (mb) and wind barbs (m/s) for (a) 0000 UTC on 28 Oct 86, (b) 1200 UTC on 28 Oct 86, (c) 0000 UTC on 29 Oct 86.

Figure 4.1: Continued.

Figure 4.2: 500 mb temperature (K) and wind barbs (m/s) for (a) 0000 UTC on 28 Oct 86, (b) 1200 UTC on 28 Oct 86, (c) 0000 UTC on 29 Oct 86.

(c)

Figure 4.2: Continued.

Wisconsin between 1200 UTC and 0000 UTC on the 29th. Figure 4.3 shows the $300mb$ wind and height fields.

4.2.3 Clouds

The infrared imagery mentioned previously shows the cold cloud system in a line from near Hudson Bay to Wyoming. This northeast-southwest configuration was maintained as the cloud system moved to the southeast and into Wisconsin by 1200 UTC. This $500km$ wide cloud band coincided roughly with the strongest $500mb$ temperature gradient. By 0000 UTC on the 29th, the clouds had moved into Wisconsin and were clearing over Minnesota.

Some variability is evident in these images. Most obvious is the clearing event that took place over Wisconsin between 1200 UTC and 0000 UTC on the 29th. This consisted of a 500 km disturbance that produced greatly enhanced cold clouds ahead and cleared the clouds behind. This disturbance was of a scale that could be resolved by the model's $33km$ nested grid but not by the rawinsonde network. This feature will be discussed in detail in the regional section of this chapter as it marks the line between two different type of cirrus systems. All other variability, although explored in detail by Starr and Wylie, is not resolvable by the model and will not be discussed in this thesis.

4.2.4 Discussion

Although the surface feature appeared to be weak, exhibiting only a small temperature gradient, the cold front was well developed up to 500 mb. Above this, there is an upper level trough that was strongest at 300 mb. The combination of the frontal lifting and the lifting at the east side of the trough should have produced a broad area of vertical motion extending through much of the troposphere.

Vertical motions calculated directly from the observed soundings using the Bellamy triangle technique are given in Starr and Wylie for the FIRE region. They note major inconsistencies between the derived motion field and the observed cloud field. They also give an elaborate discussion of the causes of the errors.

ECMWF data from the WMO archive shows a deep upward motion area primarily associated with the east side of the troughing.

42
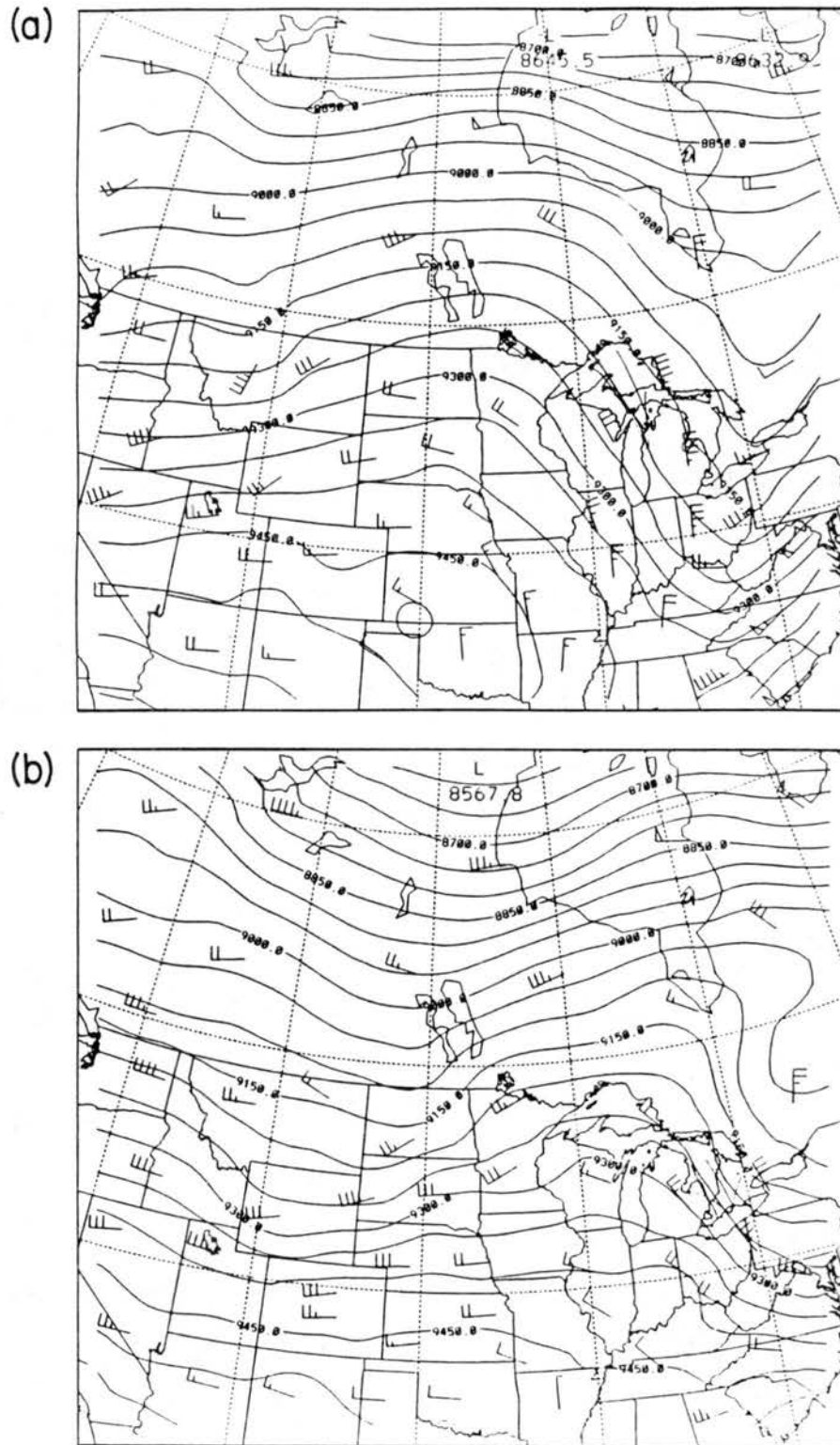
Figure 4.3: Height of the 300 mb surface and wind barbs (m/s) for (a) 0000 UTC on 28 Oct 86, (b) 1200 UTC on 28 Oct 86, (c) 0000 UTC on 29 Oct 86.
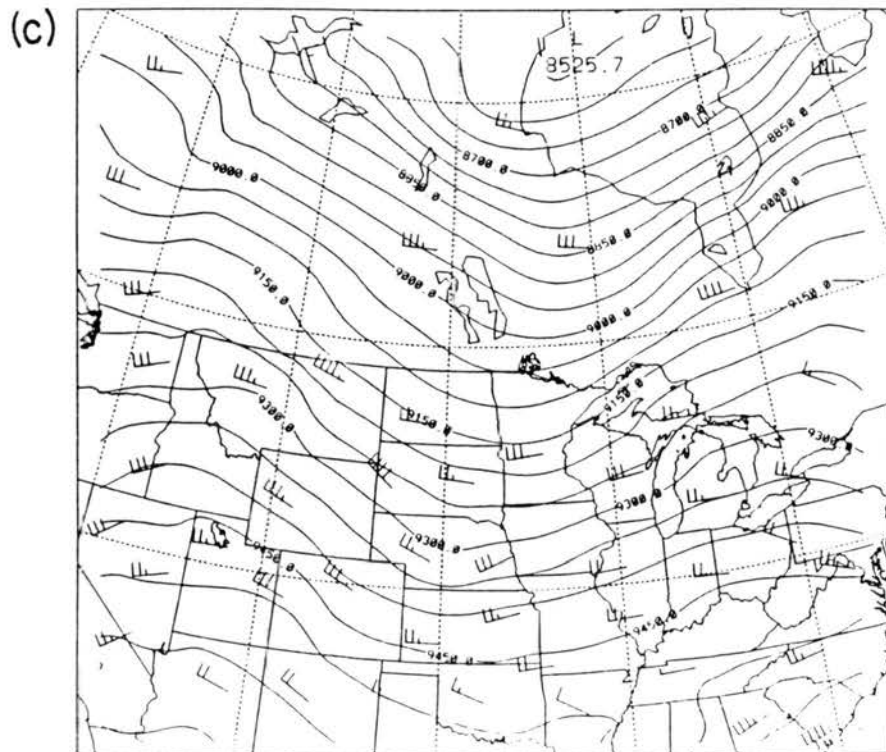
Figure 4.3: Continued.

More importantly, the $300mb$ vertical motion field matches the observed clouds, presented in the infrared imagery, almost exactly. (See Figure 4.4.) The scale of this frontal system suggests that the 2.5^o resolution of the ECMWF archive is adequate. Similar patterns are evident at 700 and $500mb$, but are not shown. From these analyses, a simple cause and effect relation can be deduced.

- The developing storm and upper level trough combined to produce a frontal region oriented northeast - southwest that propagated to the southeast.

- This frontal region had good organization and moderate strength up to 500 mb.

- The lifting ahead and above the frontal boundary, associated with the front and the upper level trough, concentrated moisture at high levels and produced clouds.

Although this is grossly simplified, lifting due to the trough and the cold frontal surface appears to explain the bulk of the clouds in this case.

4.3   FIRE area specifics: 1200 UTC - 0000 UTC

In this section, the smaller scale events over Wisconsin will be examined in detail to explore the causes of some of the variability in the cirrus cloud system. Again, Starr and Wylie present the observations in much greater detail, exacting as much information as possible. Since this modeling study can't hope to recreate all scales of motions, this discussion will be limited to describing the mesoscale clearing event that passed over Wisconsin between 1200 UTC and 0000 UTC on the 29th.

4.3.1   Surface

Figure 4.5 shows sea level pressure and wind fields for 1500, 1800, and 2100 UTC for the FIRE IFO region. The convergence line is obvious in the wind field at the leading edge of the pressure trough. Analysis of temperature and dewpoint failed to show the frontal zone. These figures show the steady southeasterly progression of the front.
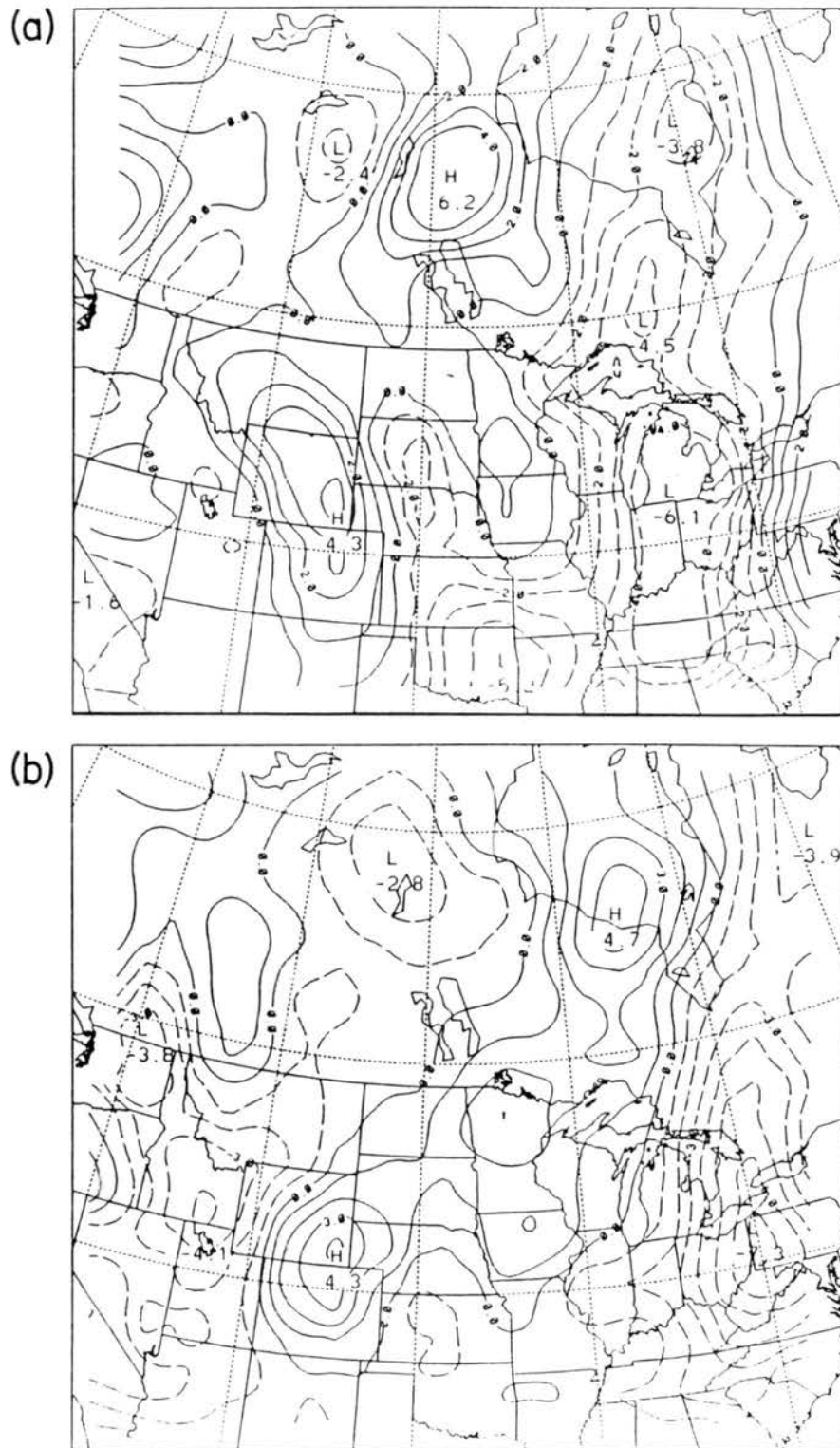
Figure 4.4: 300 mb vertical motion (cm/s) from the WMO archive of ECMWF model output for (a) 0000 UTC on 28 Oct 86, (b) 1200 UTC on 28 Oct 86, (c) 0000 UTC on 29 Oct 86.
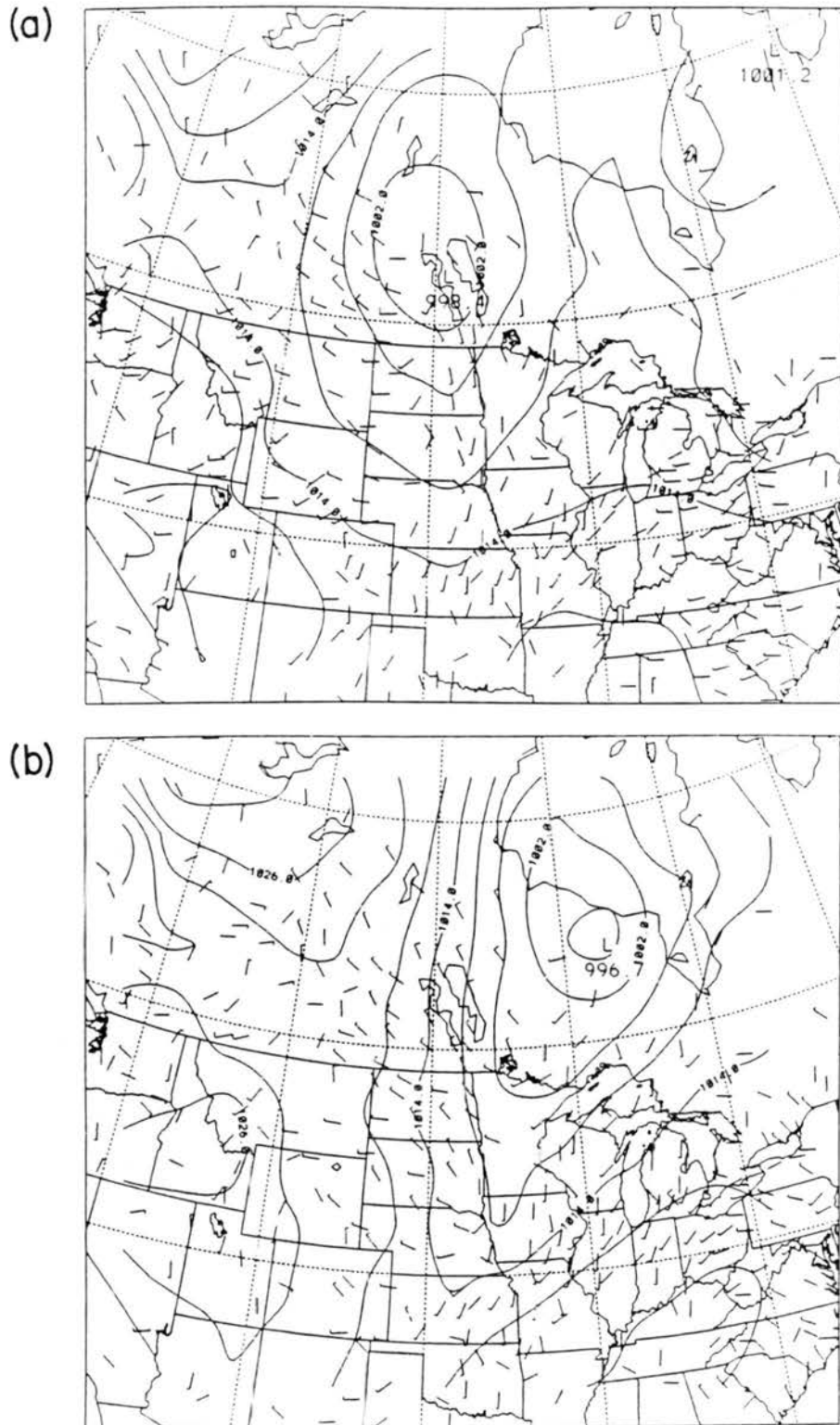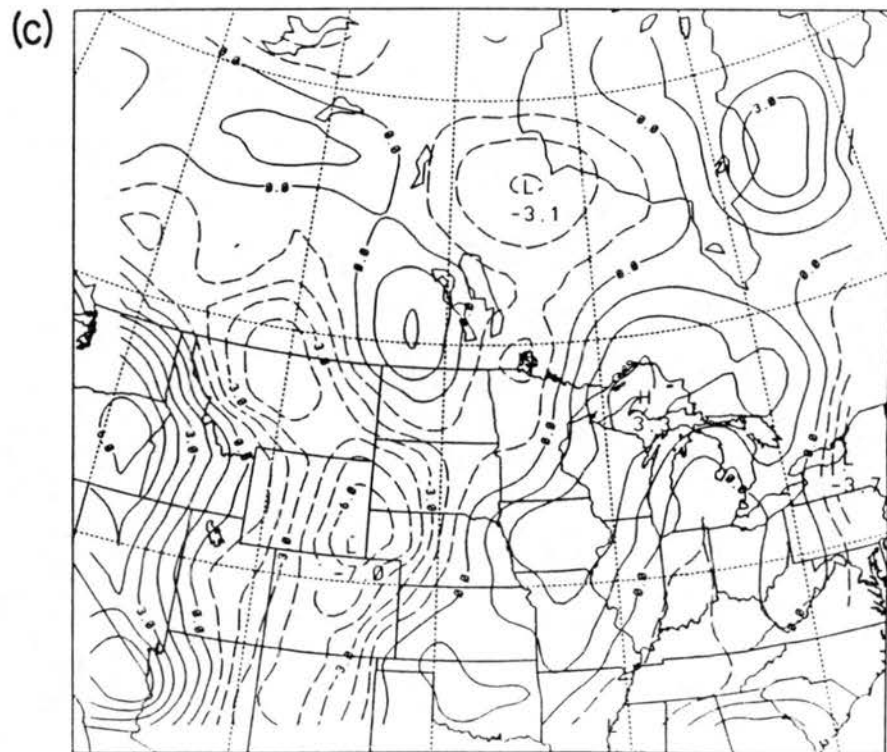
Figure 4.4: Continued.
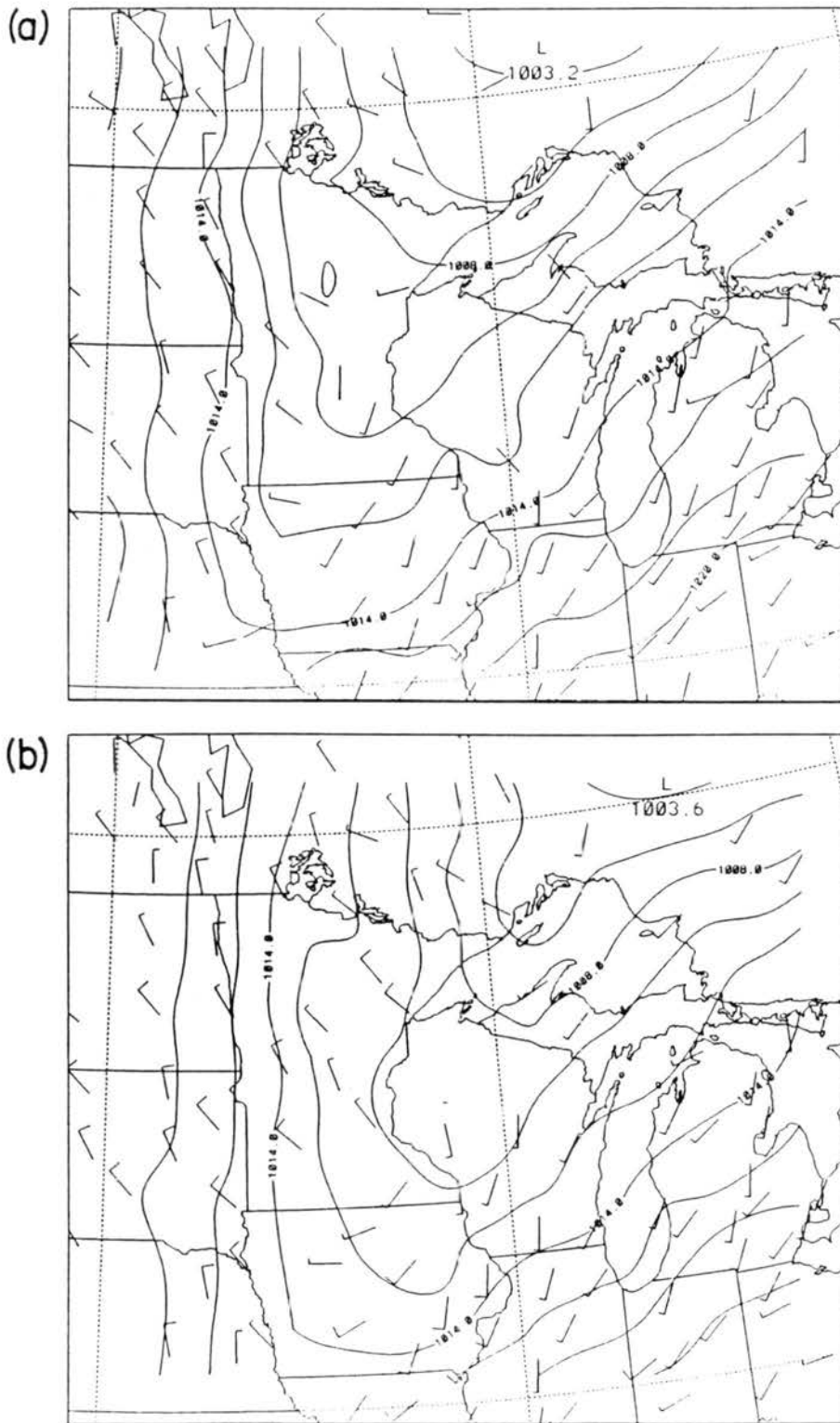
Figure 4.5: Sea Level pressure (mb) and wind barbs (m/s) for (a) 1500 UTC on 28 Oct 86, (b) 1800 UTC on 28 Oct 86, (c) 2100 UTC on 29 Oct 86.
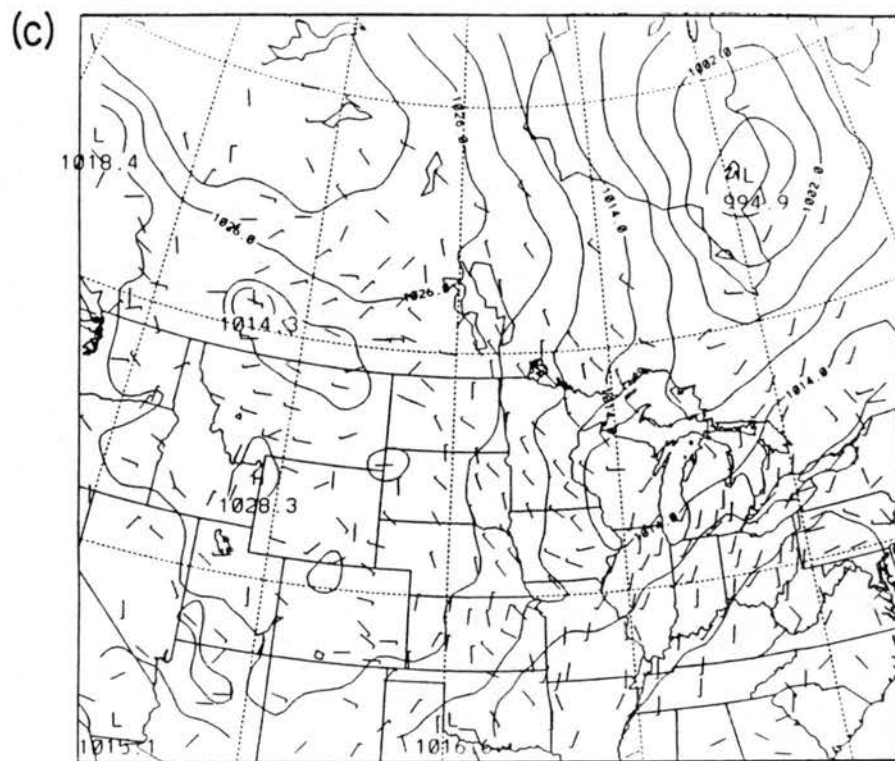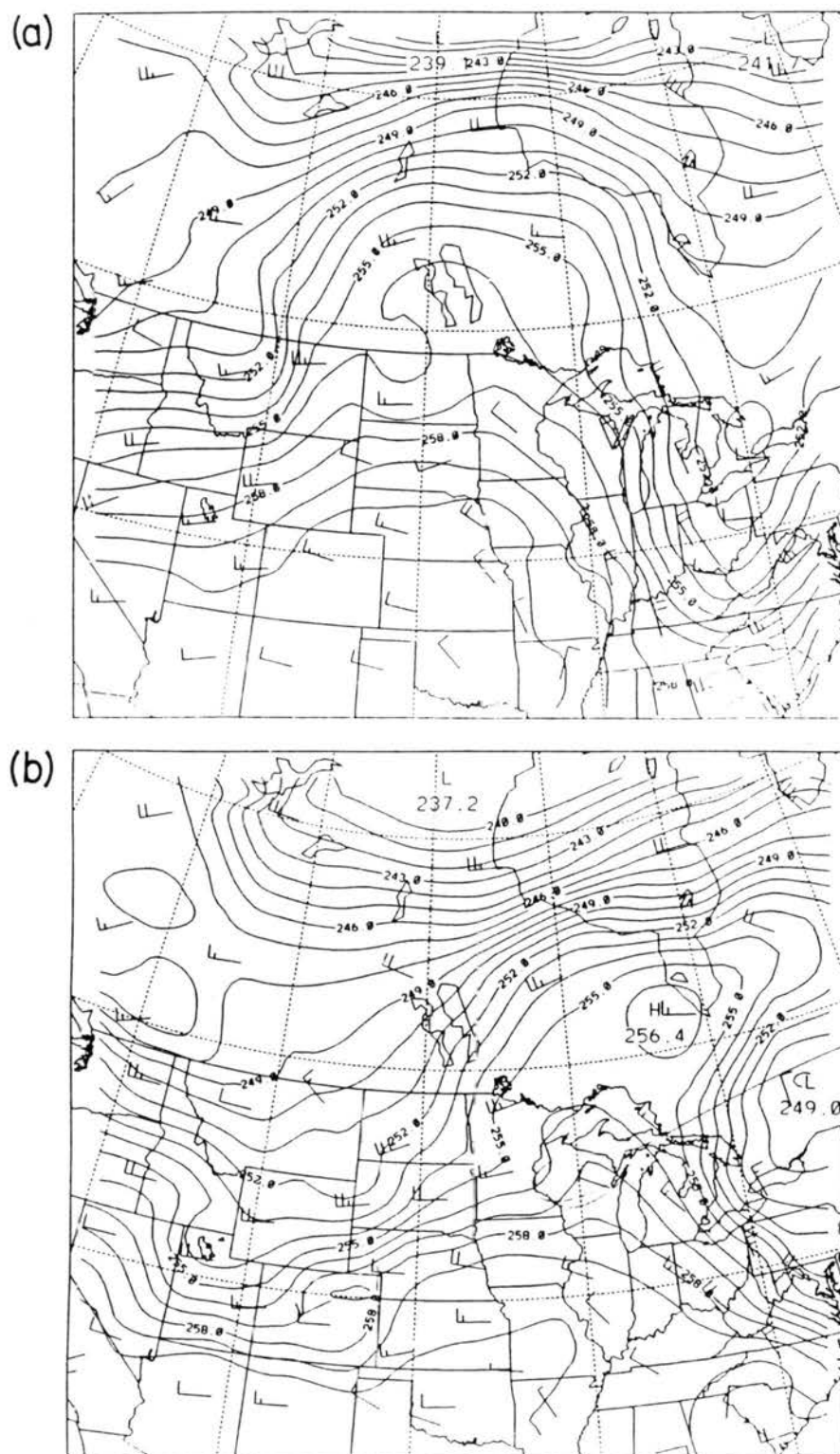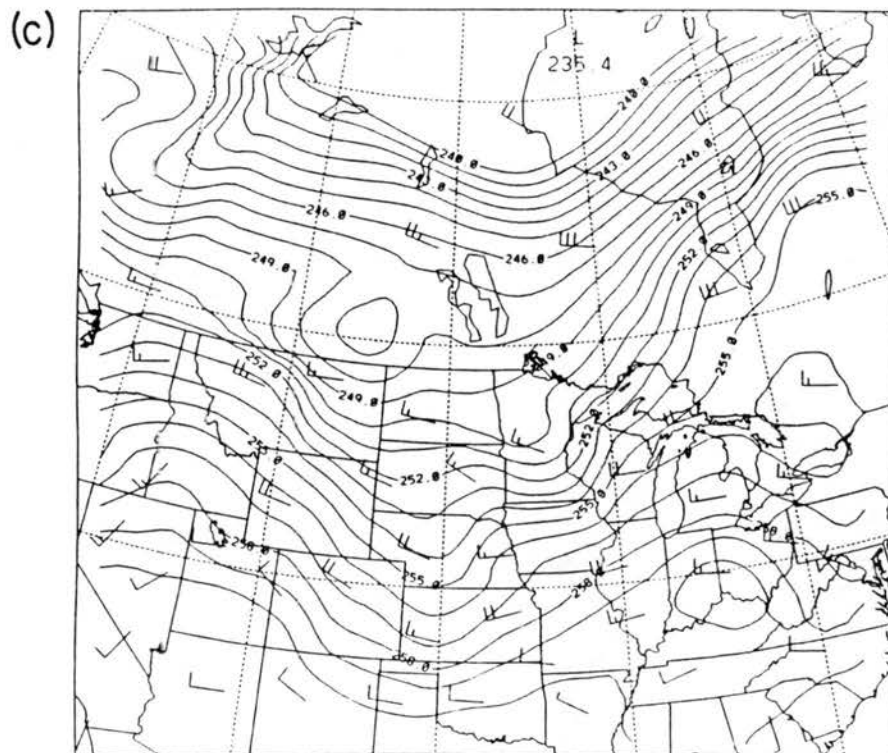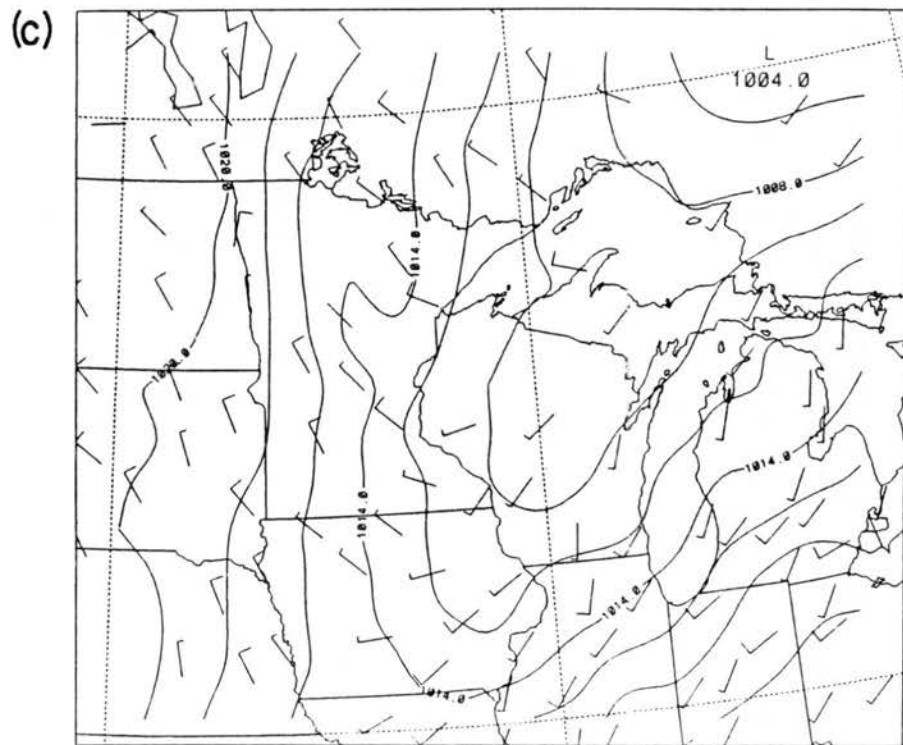
Figure 4.5: Continued.

4.3.2   Upper air

The clearing event in question, assuming it was dynamically-produced, did not appear in the 12 hourly analysis of rawinsonde data. For the FIRE experiment, standard and special rawinsonde were released every 3 hours. The increased time resolution resulted in evidence of a short wave disturbance, imbedded in the larger scale flow, that could have caused the clearing episode.

A time series of rawinsonde data from Green Bay, Wisconsin is used to explain the mesoscale events of 28 Oct 86. This time series (Figure 4.6) shows the middle tropospheric winds backing as the large scale ridge axis passed between 1200 UTC and 0000 UTC. But between 1800 UTC and 2100 UTC, the time of the clearing, winds veered indicating a troughing in the large scale ridge. Warming at $5 - 10km$ between 1200 and 1500 UTC is indicative of the warm air advection ahead of the shortwave trough. The accompanying vertical motion couplet produced the clearing episode. The enhanced cold air advection behind the trough decreased the stability in the $8 - 10km$ layer and as a result, the clouds that formed after the clearing event were much more convective in nature. This is evident in the 2032 UTC and 2200 UTC bispectral images over Iowa and later over southwest Wisconsin.

4.3.3   Clouds

Figures A.6 - A.10 show the cloud fields for the FIRE region at approximately 2 hour intervals 1330 UTC - 2200 UTC on the 29th.

The 1332 UTC image is a vivid example of the advantages of this method. Smooth, yellow clouds in Michigan and north of Lake Superior are large areas of fog or stratus. There is some evidence of low cloud over the western most top of Lake Superior, as well. The high cloud over the Minnesota/ Wisconsin border appears fibrous and has bluish tint, indicating cold cloud tops. There is an indication of the clearing shortwave in western Minnesota.

By 1502 UTC, the clear area had expanded and moved east to near the Wisconsin border. The fog and stratus remained while thicker, lower cold cloud had moved into northern Minnesota with the cold front.
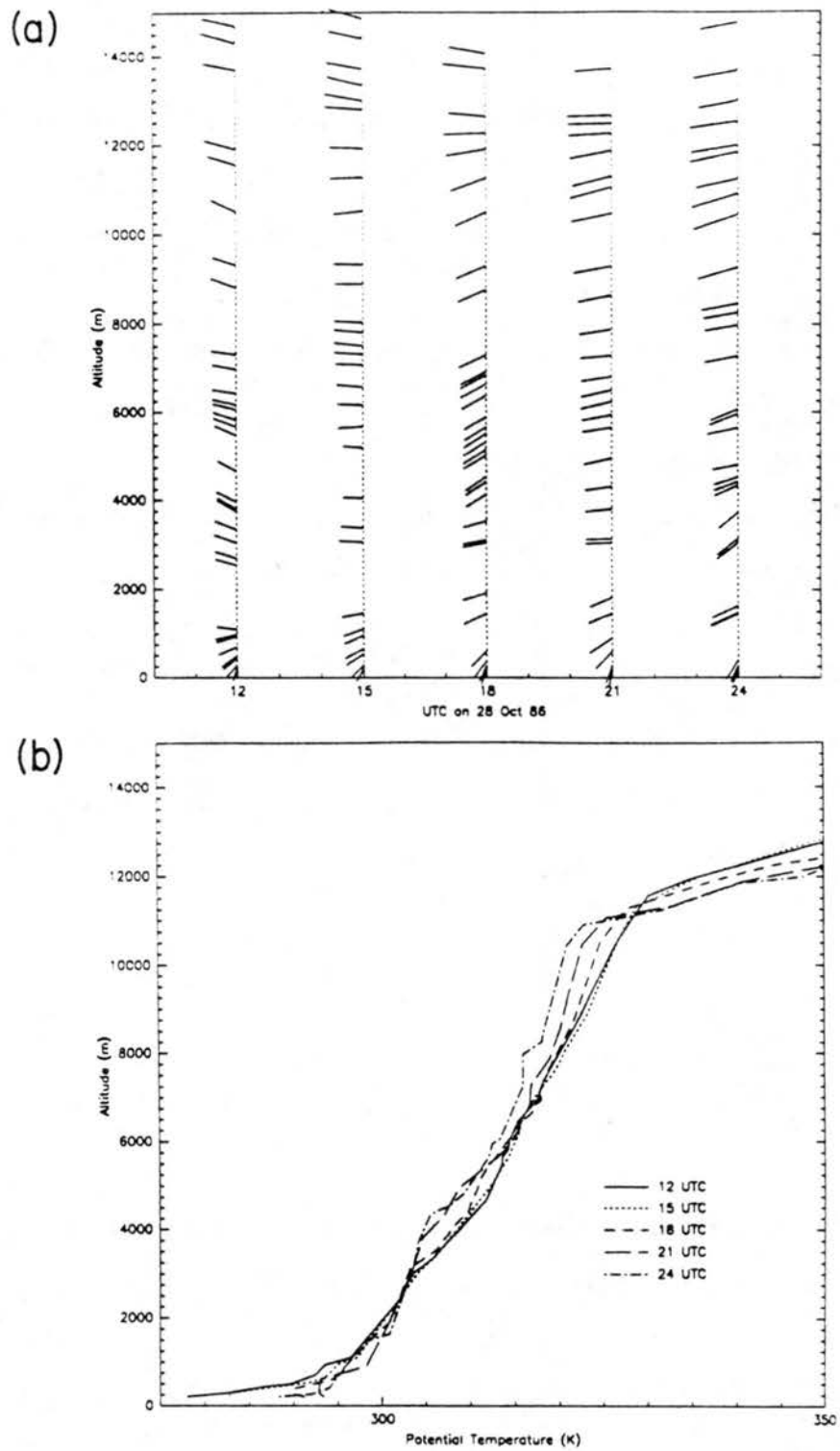
Figure 4.6: Observed sounding time series for Green Bay, WI. (a) Winds (m/s), (b) Potential temperature (K).

Because of data problems, the next image is 1902 UTC. At this time, the morning low cloud had burned off in Michigan but an extensive area had moved south across Lake Superior into northern Minnesota and the northern most portions of Wisconsin. This cloud was associated with the cold front but was behind the surface convergence line in the cold air. (See figure 4.5b) There was a smooth area of middle cloud in this area as well. The clearing line was well defined in eastern Wisconsin. To the east was a broad area of fairly homogeneous cirrus extending over Michigan. It appeared that the shortwave disturbance had enhanced the clouds ahead of the clearing line and changed the environment behind.

At 2032 UTC, the clearing line had progressed to the east over Lake Michigan. The low cloud had slowly moved to the southeast into the Upper Peninsula of Michigan. The area of smooth mid cloud to the north of Lake Superior had grown. The fibrous, convective cirrus in Iowa and southwest Wisconsin continued to grow.

As the sun set at 2200 UTC, the clearing line was still intact and had moved into central Michigan. Low clouds persisted in northern Wisconsin and light rain was reported. This image is a particularly good example of the cellular nature of some cirrus. Even at 2km resolution, cirrus generating cells are evident in central Wisconsin.

4.3.4 Vertical structure of clouds

Aircraft observations of the cirrus clouds on this day are presented in Heysfield et al. (1990). These observations were from the NCAR King Air and NCAR Saberliner aircraft. The aircraft were flown north and east of Madison, Wisconsin between 1530 UTC and 1730 UTC. The data presented is for approximately 1530 UTC when both aircraft, the NASA ER-2 research aircraft, and the LANDSAT satellite were in roughly the same location sampling the pre-clearing cirrus cloud system.

These papers described the microphysical characteristics of these clouds. In the clouds above $8.5km$, as measured by the Saberliner, total concentrations were less than 10 crystals per liter, IWC ranged from zero to $0.02g/m^3$ at $9km$, and particles smaller than $125\mu m$ constituted most of the mass. In clouds below $8.5km$, measured by the turboprop King Air, concentrations were higher at 20 crystals per liter, IWC was maximum at $7km$ at $0.2g/m^3$, and more of the total mass was in particles larger than $125\mu m$.

Starr and Wylie (1990) combine the aircraft data with lidar and satellite data to describe the pre-clearing cloud system as three layers. The highest layer is a thin, $200m$ thick, patchy layer at $11.3km$. Below this, there was a thicker, horizontally homogeneous generation layer from 10 to $10.5km$ with precipitation streamers extending to an indistinct cloud base to $8.5km$. They also describe an altocumulus layer from 6 to $8km$ that had a cloud base descending toward the clearing line. Lidar at Wasau showed cloud base dropping from $6.5km$ at 1500 UTC to $6.0km$ at 1800 UTC. This cloud layer exhibited strong internal cellularity.

After the clearing event, patchy cirrus occurred from 8.5 to $9.5km$ as evident in satellite imagery. Lidar also reported thin cirrus from 10 to $11km$.

4.3.5 Discussion

The clearing episode had all the characteristics of a shortwave disturbance with upward vertical motion on the east side and downward on the west. Although it was not measured completely by standard observations, the 3 hourly soundings and satellite coverage provided enough information to infer its existence.

Chapter 5

CONTROL SIMULATION

In order to draw useful conclusions from a modeling exercise, the model's ability to portray the phenomena must be established. This chapter describes the control simulation, an attempt to accurately simulate the events of 28 October 1986. The following sections describe the model initialization process, model configuration, and finally, the control simulation verification against observed data.

5.1 Assimilation

The model initial fields and lateral boundary tendencies were created with the RAMS Isentropic Analysis program (Tremback, 1990). This program accessed archived gridded, rawinsonde, and surface data sets at the National Center for Atmospheric Research (NCAR).

5.1.1 Data sources

The gridded data were the 2.5^o WMO archive of mandatory level winds, temperature and moisture from the European Center for Medium Range Forecasting (ECMWF) (Trenberth and Olson, 1988). This data set is regarded as very high quality and provided moisture values above $300mb$, unlike it's National Meteorological Center (NMC) counterpart. Significant and mandatory level winds, temperatures and relative humidities were taken from the archived rawinsonde data at NCAR. At the surface, the 6 hourly synoptic reports archived at NCAR were accessed to provide winds, potential temperature and relative humidity.

5.1.2 Procedures

The RAMS assimilation program was run at NCAR and accessed the aforementioned data sets from their tape archives. The data were interpolated to a latitude/ longitude

grid covering 177°W to 9°W and 3°N to 81°N at 1.5° spacing. This grid used potential temperature as the vertical coordinate with 1°K resolution from the 260°K to 300°K, 2° resolution to 360°K, 5° resolution to 460°K and 10° resolution to 500°K.

The Barnes (1973) objective analysis scheme was applied to these variables. The parameters in the scheme were set to allow a 2000 km wavelength to be retained at 90% of it's original amplitude. The response was chosen to retain only the features adequately resolved by the rawinsonde network. Based on an average station separation (Δs) of 500 km, waves with a $2\Delta s$ wavelength would be heavily damped. The Montgomery streamfunction was hydrostatically-integrated from a 360°K boundary condition.

After completing the isentropic analysis, the model variables were interpolated to the model's outermost or coursest horizontal grid. The wind components, streamfunction and humidity were interpolated horizontally on the isentropic surface to model grid points. The height of the isentropic surface was determined, allowing linear vertical interpolation of wind, potential temperature and humidity to the models σ_z coordinates. A hydrostatic integration determined the pressure at the model grid points.

The model topography was interpolated from a Navy 10 minute averaged data set archived at NCAR. The Barnes analysis scheme was applied as a smoother to the terrain, with a response that retained $1000km$ features at 90% of their original amplitude. Since this study didn't concern itself with the effects of topography, the simplified representation in Figure 5.1 is appropriate, where the assumption is made that synoptic scale effects of the Rocky Mountains are retained.

The RAMS soil model also required initial data. Since soil temperature and moisture measurements are not made routinely, a first order estimate based on the air temperature and humidity was made. The simulation started at 0000 UTC, approximately 1 hour after local sunset. The soil temperature profile was assumed to be warmer than the air by 3°K at the soil surface and decreasing to equal temperature at a depth of 50cm. The soil moisture profile was set at 10% of it's surface value. A clay loam soil type was used for all land areas.

The surface effects on this study would appear to be limited since we are concerned with upper level ice clouds. The soil model is the lower boundary condition and determines
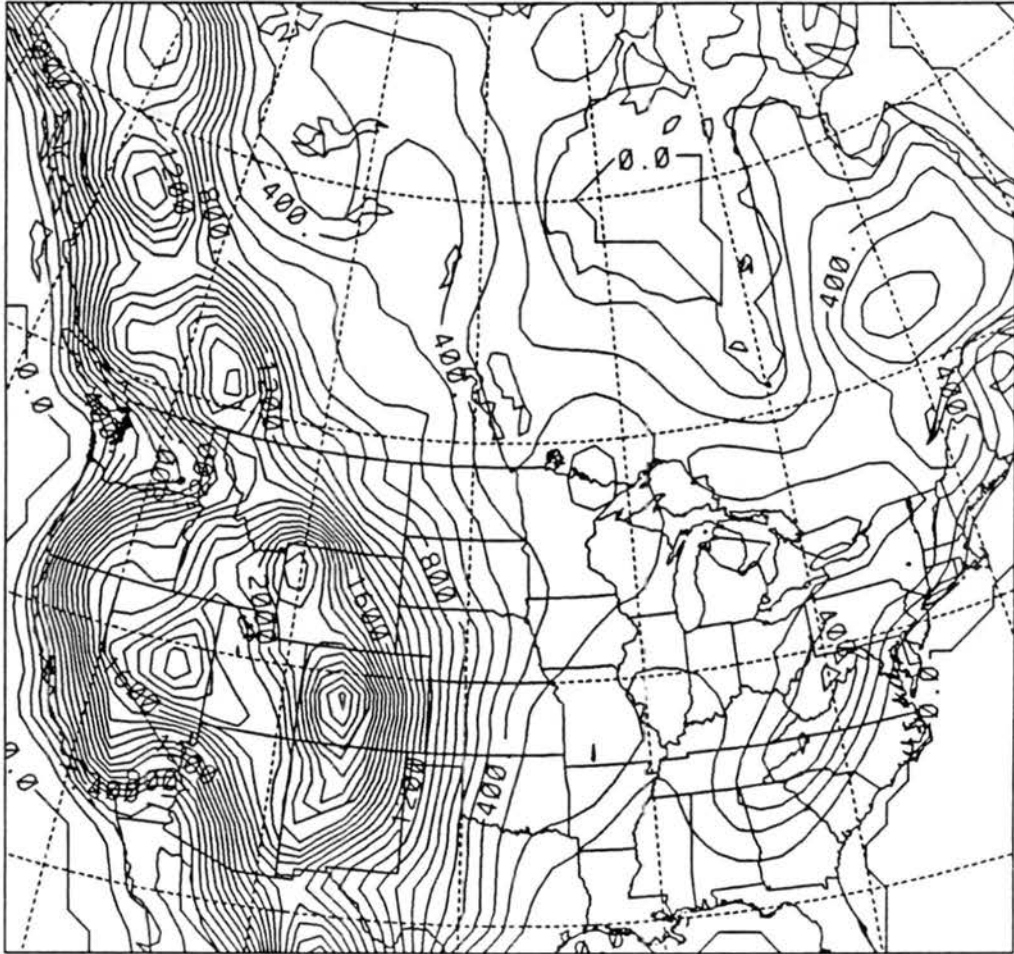
Figure 5.1: Smoothed topography used for all simulations.

the surface heat and moisture fluxes as well as the temperature used as a lower boundary condition for radiation calculations. This soil model initialization is highly simplified. Cram (1990), however, showed very limited sensitivity to a much more complicated soil initialization scheme when simulating a strongly forced squall line weather system.

The initial conditions on the model grid were then used to load the model variables at the initial time and to provide lateral boundary tendencies in the Davies nudging areas. Model initialization files were created for every 12 hours and the lateral boundary tendencies were assumed to be a linear fit between the two.

5.2 Model grid configuration

In Chapter 3 we described the equations, numerical schemes, and parameterizations chosen for this study. The following describes the grid location, spacing and nesting used for all the simulations presented. In Chapter 7 the sensitivity studies will be described by listing the differences from the control simulation.

The outermost grid was set on a polar-stereographic plane tangent at 97.5^oW and 48.5^oN. It contained 49 points in the x-direction and 45 in y-direction with $100km$ grid spacing on the polar-stereographic plane. Figure 5.2 shows the grid point locations.

The vertical grid spacing was designed specifically to allow maximum resolution at cirrus altitudes. The spacing was set to minimize the total number of points, reduce the amount of stretch or shrink, and still provide $200m$ resolution between 5 and $11km$. The result is 69 points from the surface to $19.2km$.

Grid stretching is known to affect wave propagation, especially if the stretch ratio is large. This can act to reflect or refract waves if the wave cannot be resolved with the coarser grid spacing. To determine the magnitude of this effect in this case, a linear mountain wave test like that performed for the radiative top boundary condition was run. This test showed some reduction of the vertical momentum fluxes in areas where the grid spacing was coarser than the 250 m used in the previous tests. It also showed an improvement in areas where it was less than 250 m. The vertical motion field showed very little effect. As a result, it appears that the chosen grid spacing is subtle enough that wave propagation is more affected by a reduction in the number of grid points per wavelength.
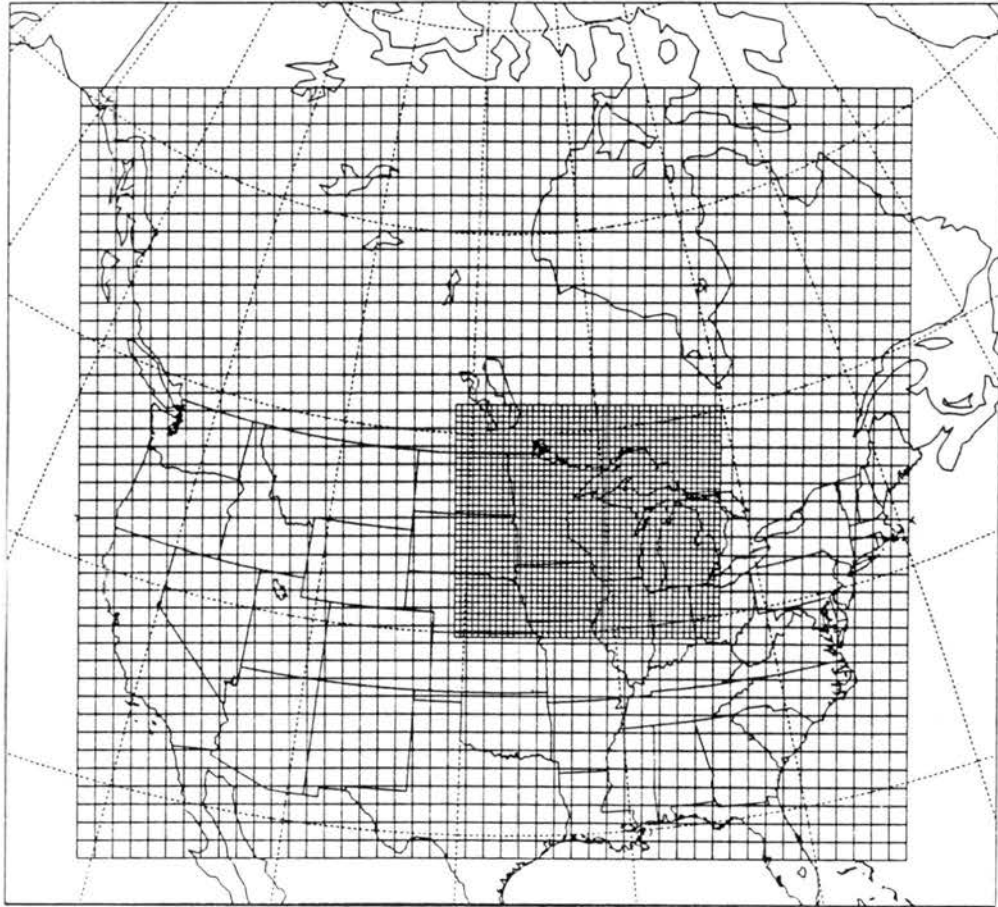
Figure 5.2: Model grid locations.

The nested grid used 47 x-points and 41-y points with a 3 to 1 nest ratio to provide $33km$ horizontal resolution over the FIRE IFO region (See Figure 5.2). The nest shared the vertical grid configuration with the course grid.

5.3 Verification

There is no end to the number of different verification possibilities. Any combination of time, space, and variables would be useful in determining the ability of this model to accurately simulate this case study day. However, time and space in this thesis are limited, so only the fields and perspectives used to describe the case study day will be used here. Once again, the output will be divided by scale with output from the $100km$ grid representing the synoptic scale and output from the $33km$ grid representing the mesoscale.

To be complete, the 0000 UTC 28 October 86 fields are presented to show the capabilities and short comings of the assimilation process.

5.3.1 Synoptic features

Surface

The $100km$ grid surface analyses are shown in Figure 5.3a,b,c. The sea level pressure reduction algorithm is based on the U.S. Standard atmosphere and does not match that used by the National Weather Surface.

At the 0000 UTC initial period, the model shows the Canadian low at more than $4mb$ lower central pressure. There also appears to be some problems with the reduction algorithm over the Rockies of western Montana and Idaho. Overall, however, the pattern and location were very similar and the surface wind patterns match nicely.

After 12 hours, the low has deepened and the center has moved over Hudson Bay, away from observations so no direct comparison of the central pressure is possible. The surface convergence line extending to the southwest of the low is apparent in the surface observations and the model output. This wind shift line and pressure trough matches almost exactly from Minnesota down into the Texas panhandle.

By 0000 UTC on the 29th, the low has crossed Hudson Bay and is away from the dense observing network. The central pressure seems reasonable given the lack of exact

59
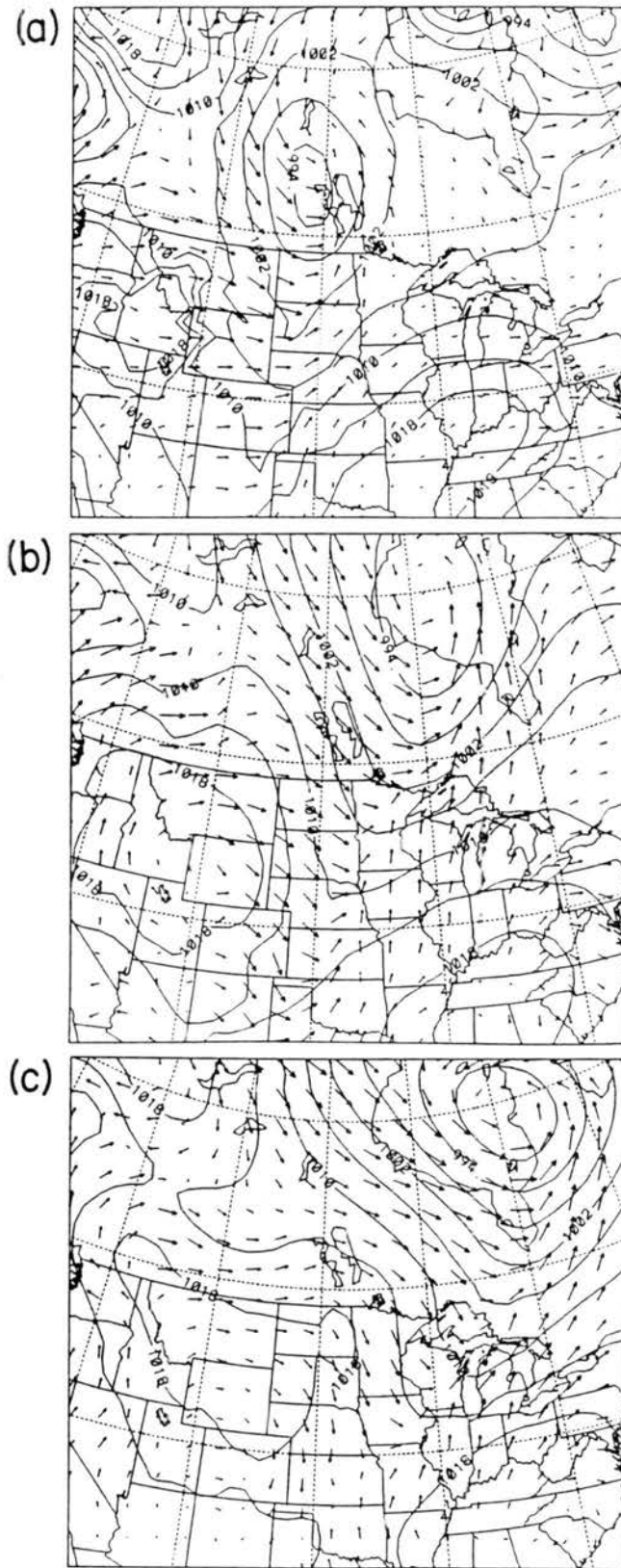
Figure 5.3: Sea Level Pressure (mb) and winds (m/s) at (a) 0000 UTC, (b) 1200 UTC, (c) 2400 UTC.

measurement. Even after 24 hours, the surface pressure trough and convergent line matches nearly perfectly from the center of Wisconsin to the center of Oklahoma.

Overall, the model handled these surface features extremely well. Although only part of the total atmospheric picture, this represented a very good simulation of the evolving mass field.

Upper Air

Comparison of the $500mb$ temperatures (Figures 5.4a,b,c) at the inital time shows that the middle tropospheric flow and thermodynamics are initialized very well. The model field is smoother but the observed contours could be biased because of the lack of stations.

At 1200 UTC on the 28th, the model has moved the cold air south into Montana and has pushed warm air into Canada building the ridge there. The sharp gradient zones that appear in the observed analysis are smoothed somewhat by the model.

After 24 hours, the model patterns match very well again. For example, the $255°K$ contour matches almost exactly on the two figures. In both cases, this line appeared to mark the front edge of the 500 mb frontal zone.

At $300mb$ (Figures 5.5a,b,c), the height and wind fields initialized well. The jet moving over Michigan is very evident on both analysis as well as the jet on the East Coast.

At 1200 UTC, the ridge axis is passing over Wisconsin and the model represented this well. As an example, the $9300m$ contours match very well.

By 0000 UTC on 29 Oct 1986, the trough had deepened and the west side of the ridge was passing Wisconsin. Again, this field was very well represented. Note the wind minima over Arkansas and Tennessee.

Overall, this simulation recreated the synoptic patterns extremely well. From this, one would expect the synoptic scale forcing to be well represented as well. The $300mb$ vertical motion field is shown for 1200 UTC and 0000 UTC on the 29th in Figures 5.6a,b. The model is not initialized with w so, it is not available for the starting period.

The comparison between the RAMS generated upward motion and the ECMWF analysis for 1200 UTC shows basic agreement in magnitude. As an example, the $2cm/s$ area over Minnesota appears on both analysis. The magnitude of the other maxima and minima
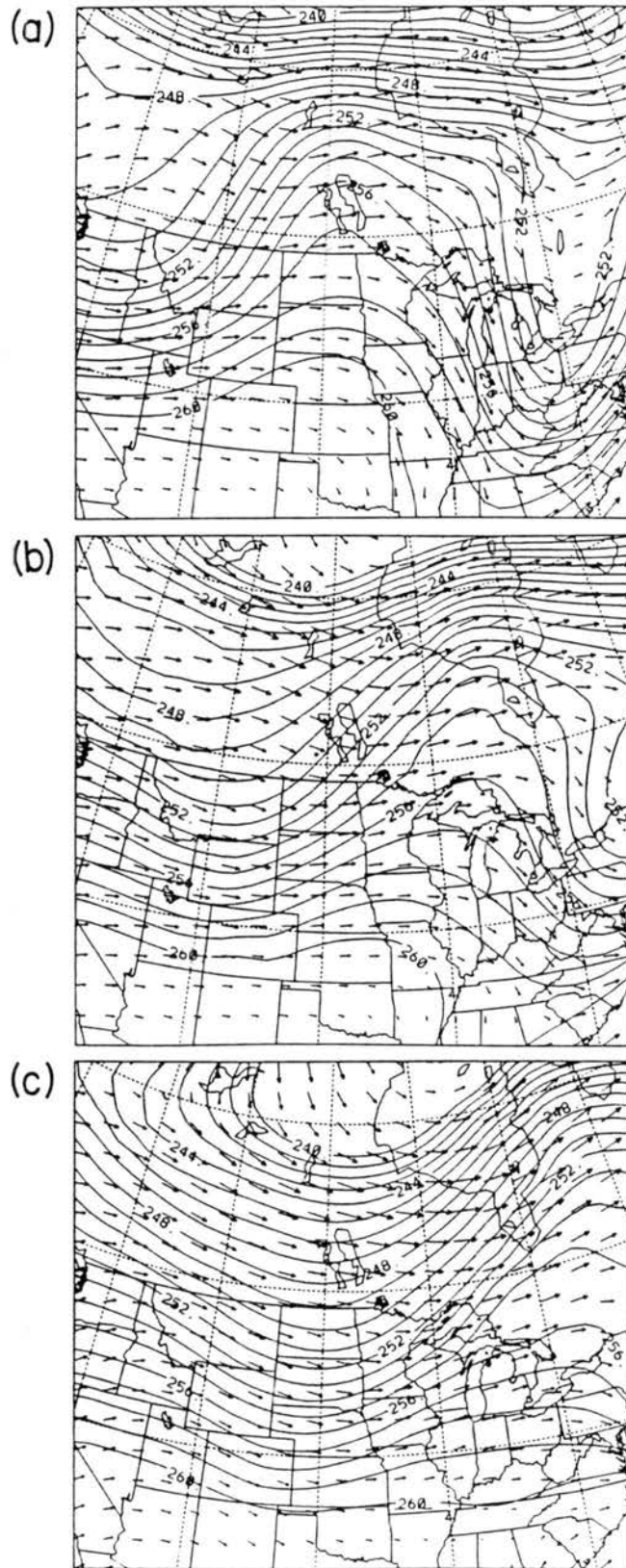
Figure 5.4: 500 mb temperature (K) and winds (m/s) at (a) 0000 UTC, (b) 1200 UTC, (c) 2400 UTC.
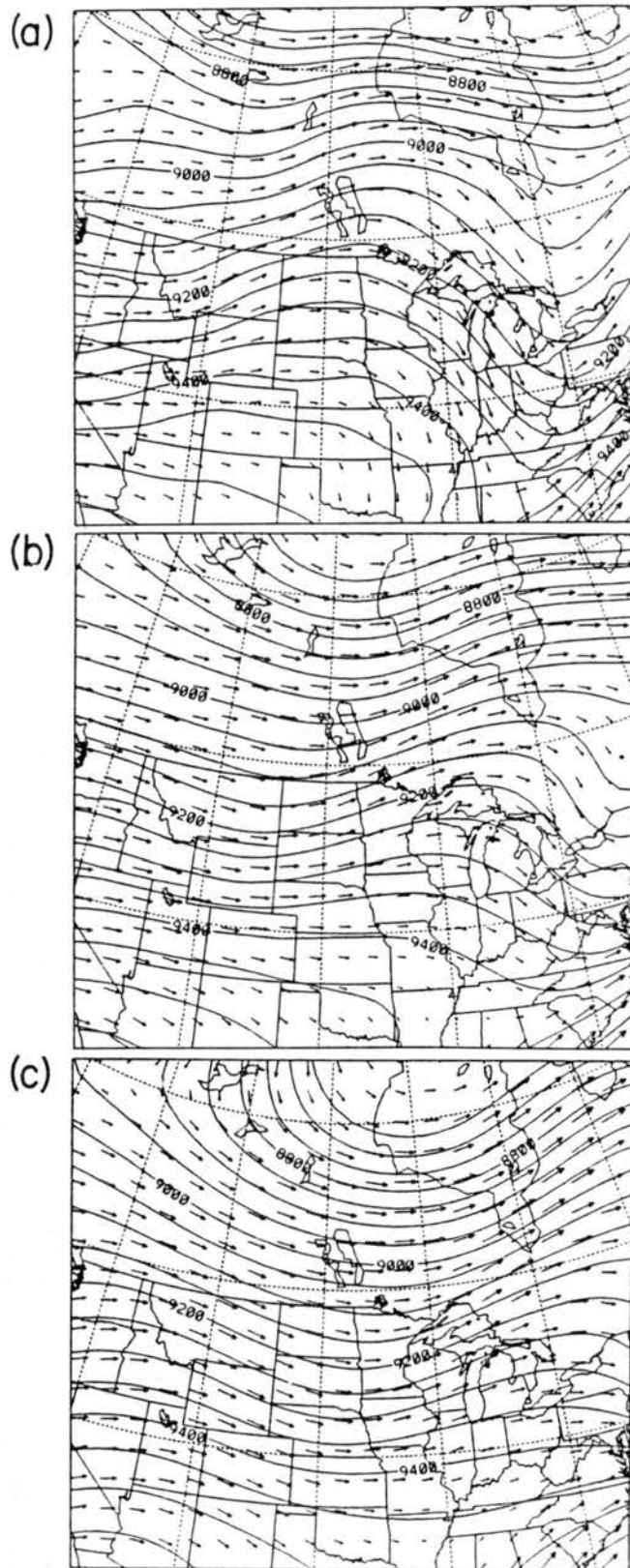
Figure 5.5: 300 mb height (m) and winds (m/s) at (a) 0000 UTC, (b) 1200 UTC, (c) 2400 UTC.
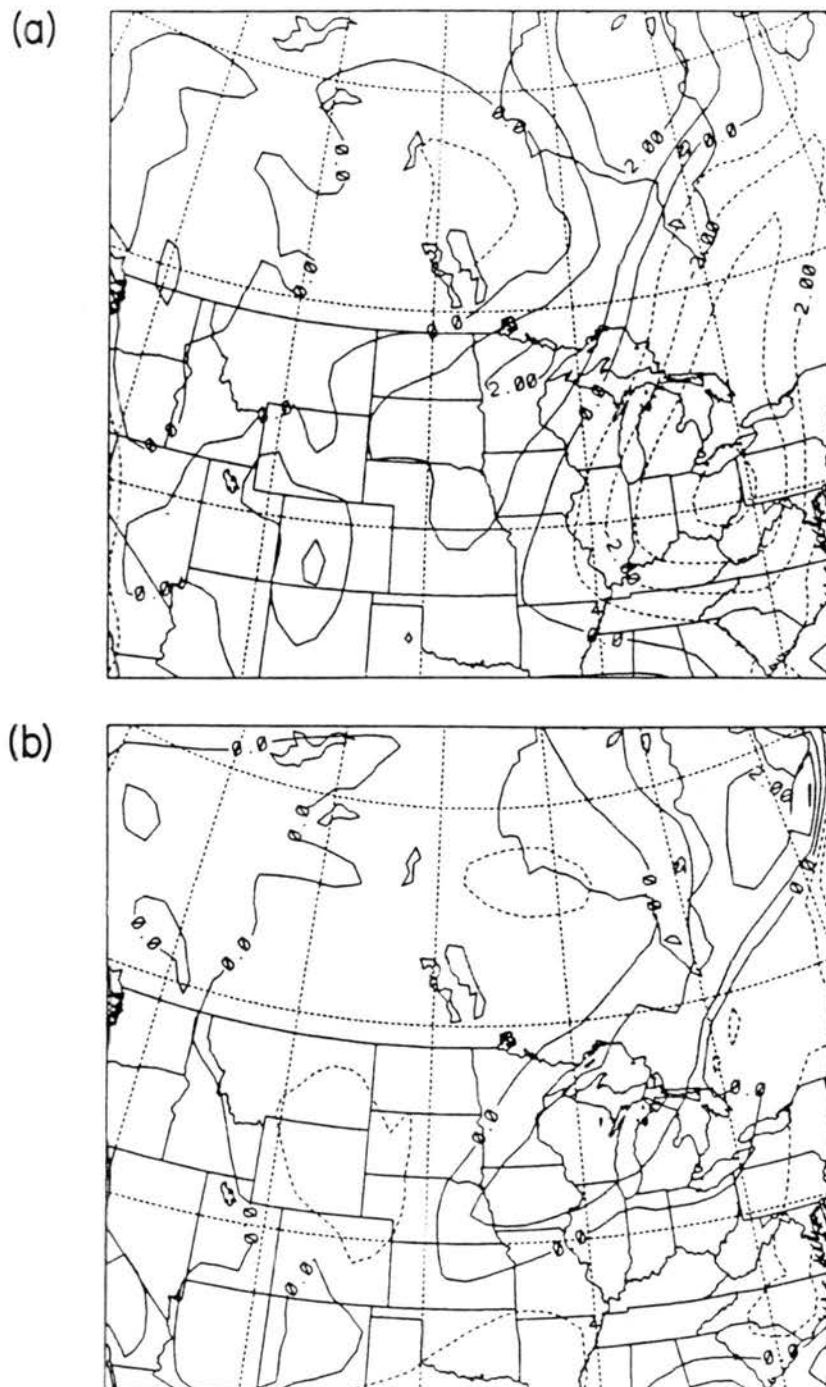
Figure 5.6: 300 mb vertical motion (cm/s) at (a) 1200 UTC, (b) 2400 UTC.

may disagree because the ECMWF model is global and thus can predict on systems for a long period of time. The systems near the edge of the model grid are stongly effected by the grid boundaries. Since these weren't the systems being studied, this doesn't appear to pose a problem.

By 0000 UTC, the maxima over the Great Lakes matches fairly well, as does the one over Hudson Bay. However, the large motions in the western United States are not represented in the model. These motions are the result of a strong Pacific storm moving onshore. Since the model would have had to manufacture this system as a boundary condition, it is not surprising that it is not simulated very well.

Clouds

In order to compare model-generated clouds with satellite imagery, ice water path (IWP) was used as a substitute for actual calculations of upwelling longwave radiation. Such calculations are a thesis topic by themselves and are not the main emphasis here. However, arbitrary horizontal cross sections through the model atmosphere would be completely unrepresentative as well.

IWP is defined as:

$$IWP = \int_{z_b}^{z_t} r\rho dz \qquad (5.3.1)$$

where r is the ice mixing ratio and ρ is the dry air density. This quantity, integrated over a certain layer of the atmosphere, is a measure of optical thickness.

For our purposes, horizontal variations in this quantity will match, to a great extent, horizontal variations in the upwelling irradiance if the following assumptions are made:

- Horizontal variations in the surface and atmospheric temperatures are small.

- Horizontal variations in emitting gases (CO_2, O_3) are small.

- Horizontal variations in water vapor match that of the condensate to some degree.

If these are fair assumptions, which they appear to be, horizontal differences in the upwelling irradiance will be due to changes in the cloud IWP. The changes in the upwelling

irradiance due the vertical position of the cloud are roughly accounted for by splitting the atmosphere into two layers, $0 - 6km$ and $6 - 12km$. The results are shown in Figures 5.7a,b,c,d for high cloud and in Figures 5.8a,b,c,d for the low cloud.

As a final note about IWP, this calculation included the rare occurence of liquid water as well. Thus the mixing ratio in the above equation is the condensate mixing ratio. IWP was chosen because it represents most of the cases and use of it exclusively avoided introducing a condensed water path quantity.

When compared to the IR satellite imagery at 0600 UTC and 1200 UTC, the model high cloud area is roughly the same as the bright white, cold cloud tops in the imagery. The thin cloud, shown by very low values of IWP, covers more area than is obvious in the imagery but the higher values match the thick cloud very well.

Low cloud areas are maximum over Hudson Bay, associated with the low center, but lingering clouds are apparent over Ohio, West Virginia, and Pennsylvania. The low cloud IWP matches this area very well.

By 1800 UTC, the clearing event is occuring over Wisconsin. While this doesn't appear exactly in the model, the highest IWP values match the bright, thick pre-clearing cloud mass extremely well. The new generating clouds over Nebraska are not simulated.

Low cloud is particularly obvious in northeastern Minnesota associated with the cold front. These also appear as high IWP values. Clouds also continue over West Virginia and Pennsylvania.

And finally, at 0000 UTC, high IWP values for high clouds are found in northern Michigan and across Lake Huron. This roughly matches the dense cloud ahead of the remnants of the clearing line. Thinner cloud remains in Wisconsin, Illinois and Iowa. Note that the western edge of this new cloud matches the lowest IWP contour almost exactly.

Low cloud still remains over Minnesota and is shown in the low cloud IWP field. Notice the familiar comma shape to the low cloud pattern over Hudson Bay associated with the deepening low pressure system.

Discussion

The dynamical fields of 28 Oct 1986 were extremely well represented by this control simulation. It is hard to expect any better results in this regard. The cloud fields are also

Figure 5.7: Ice water path 6-12km at (a) 0600 UTC, (b) 1200 UTC, (c) 1800 UTC, (d) 2400 UTC.
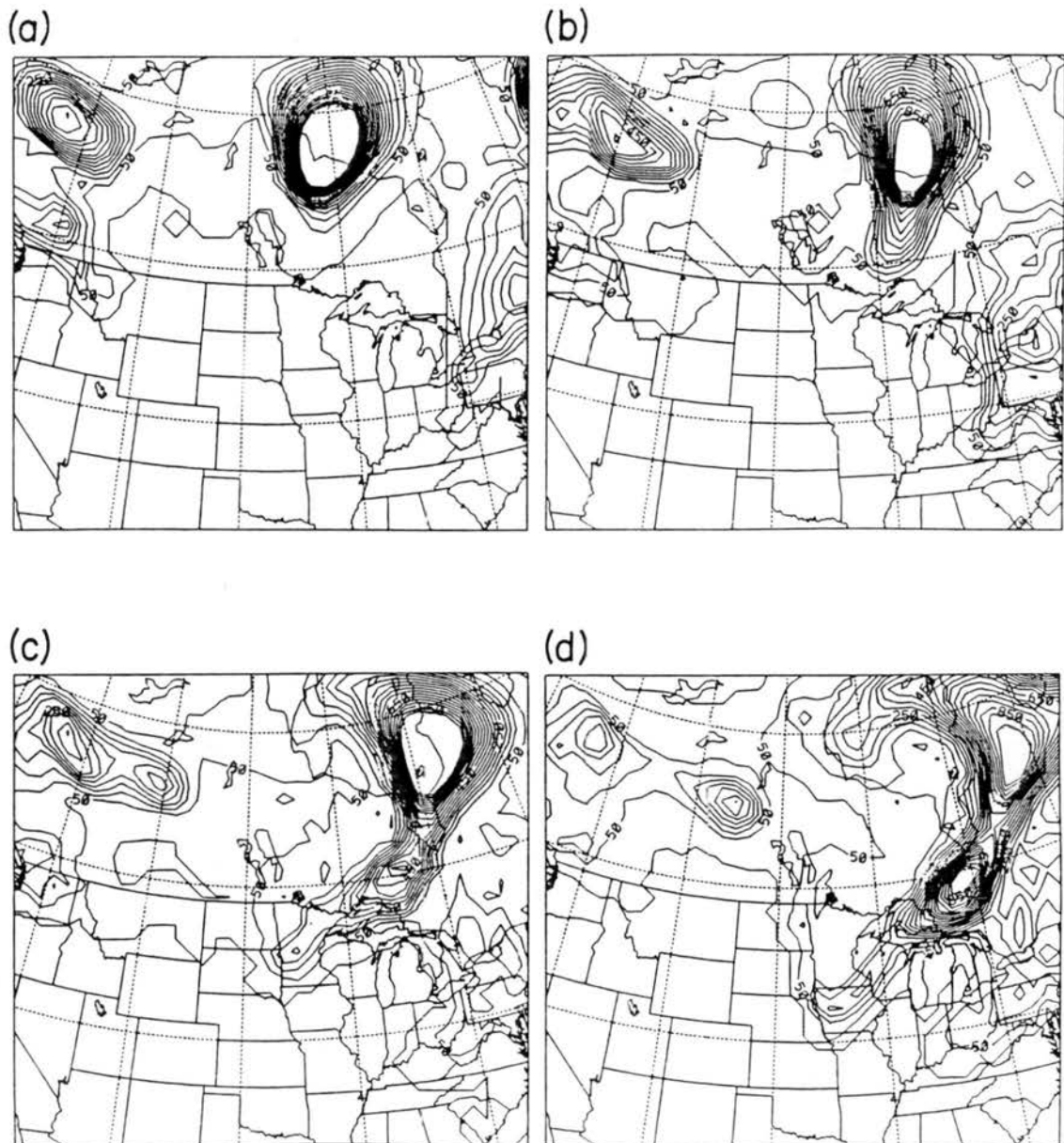
Figure 5.8: Ice water path 0-6km at (a) 0600 UTC, (b) 1200 UTC, (c) 1800 UTC, (d) 2400 UTC.
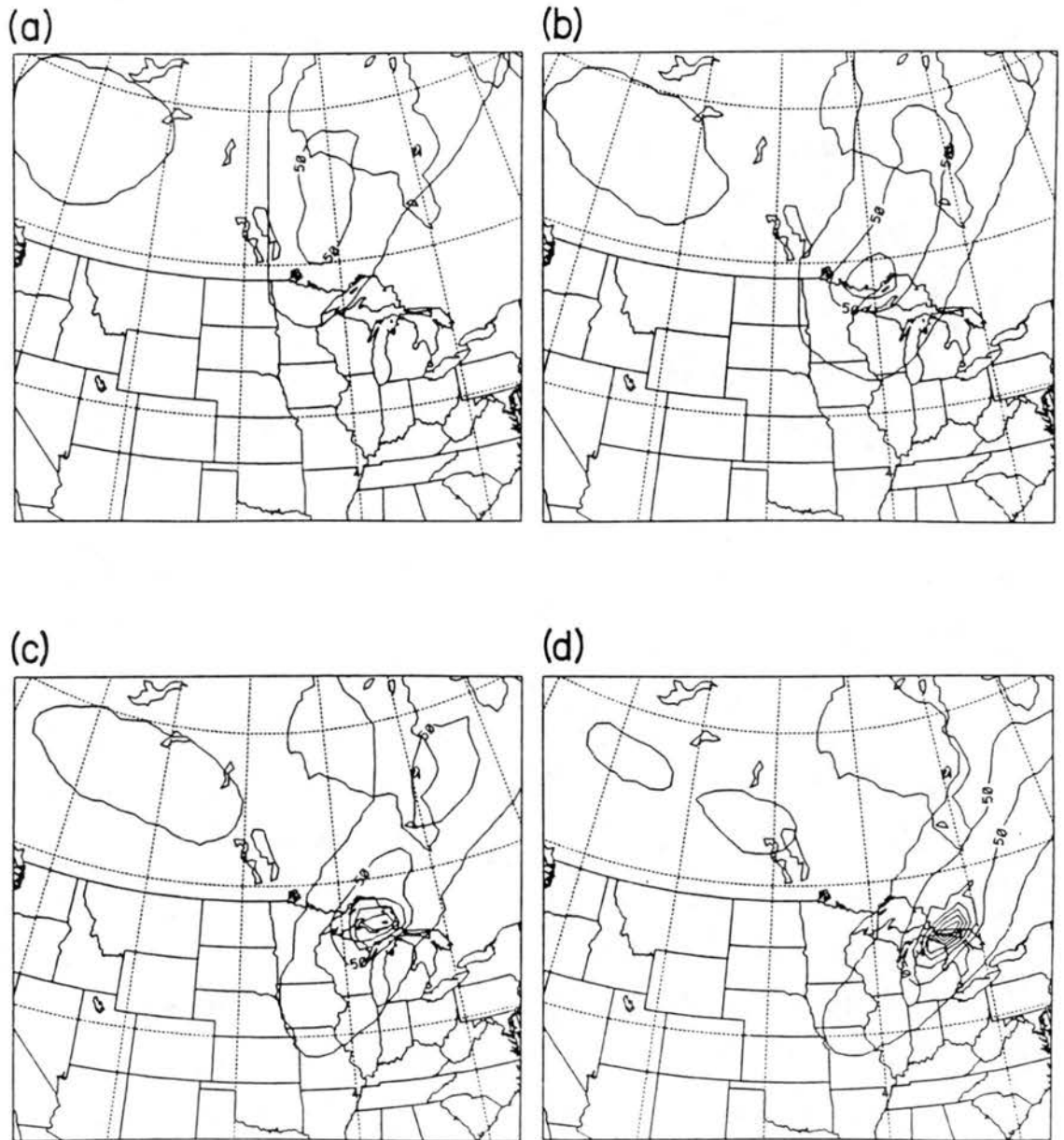
very well simulated with the exception of the mesoscale clearing event over Wisconsin. This will be discussed in more detail in the next section. The clouds appeared thick where they should and thin elsewhere. One could not expect to see changes in the nature of the clouds on a $100km$ grid. The bulk microphysics code used to represent these clouds predicts values representative of the grid volume. Variations in the volume are not taken into account.

5.3.2 FIRE area specifics 1200 UTC - 0000 UTC

As was shown in the previous section, the control simulation recreated the large scale features of 28 Oct 1986 very well. On a smaller scale, that of the $33km$ nested grid, the model produced some but not all of the observed features. In this section, verification of the $33km$ grid is presented and discussed.

Surface

The sea level pressure and wind analyses for the nested grid are shown in Figures 5.9a,b,c for 1500, 1800, and 2100 UTC. The convergence line associated with the surface front is clearly seen as a windshift in these figures. This feature moves from near the northern border of Wisconsin at 1500 UTC to the midsection of Wisconsin by 2100 UTC. There also appears to be a secondary pressure trough developing and so, two windshift lines. The primary trough extends from the Canadian surface low, through the upper peninsula of Michigan, through central Wisconsin near Green Bay, and down into Iowa. The secondary trough extends across Lake Superior. Once again, the reduced pressure appears to be lower than the observed values. The agreement between the overall patterns remains very good with the convergent lines matching almost exactly.

Upper Air

Unlike the observations in Chapter 4, the model produced more than enough output to detect the presence of a short wave disturbance. However, it also appears from these data that the model underforecast this feature to the point that very little effect was seen in the cloud fields. To be consistent, Figures 5.10a,b show a model-derived sounding for Green Bay, Wisconsin for comparison with Figure 4.6. This was created by interpolating the model data to the latitude and longitude of Green Bay. These data do not represent

69

Figure 5.9: Sea level pressure and winds from the model $33km$ nested grid at (a) 1500 UTC, (b) 1800 UTC, (c) 2100 UTC.
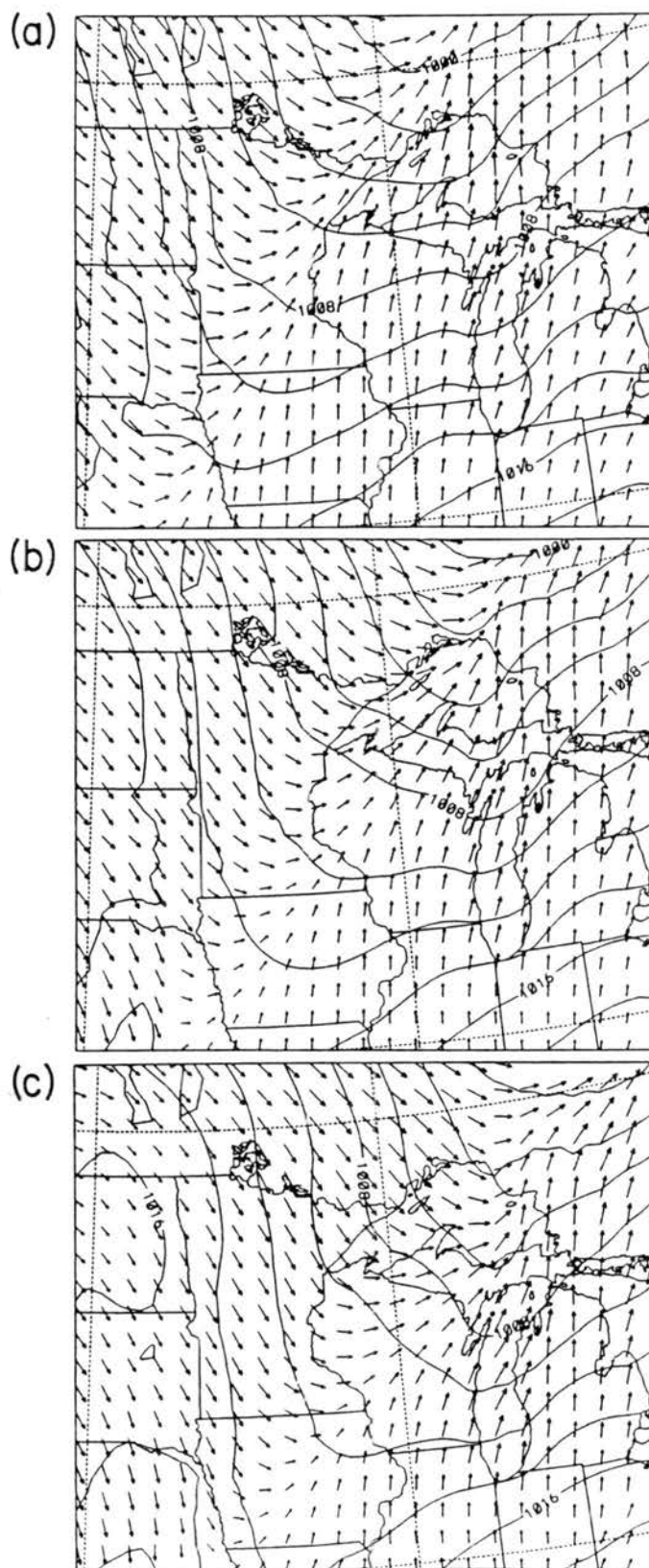
the flight of the rawinsonde balloon either in time or space but rather is a snapshot of the approximate station location.

The model-derived winds match the observed winds very well in both speed and direction, but the abrupt backing and veering evident in the observed mid level flow is not represented in the model data.

A comparison of the potential temperature profiles shows good overall agreement. The model sounding appears to have smoothed the tropopause discontinuity but still retains the tropopause lowering tendency. The model sounding shows warming in the $7 - 9km$ layer between 1500 and 2100 UTC. This matches very well with observed warming in the $6 - 8km$ region. There are some noteworthy discrepancies, however. The surface inversion is well represented at 1500 UTC but there is no evidence of a well-mixed boundary layer developing in the model. Perhaps more important for this case study, the destabilization that was observed to occur in the $8 - 10.5km$ layer, does not occur in the model simulation. The lapse rate that decreased due to the $7 - 9km$ warming returned to pre-disturbance levels by 0000 UTC on the 29th. The observed sounding destabilized tremendously in the $5 - 10.5km$ layer after 1800 UTC.

Clouds

Cloud area coverage has been discussed on the synoptic scale by using the simulated ice water path and satellite imagery. This does not provide a detailed picture of the vertical structure of cirrus, a very important aspect of these types of clouds.

The FIRE Cirrus IFO made extensive use of vertically-pointing lidar systems capable of providing detailed cloud base, depth, and optical property information on very short time scales (Sassen et al., 1990). Grund and Eloranta (1990) operated the University of Wisconsin High Spectral Resolution Lidar (HSRL) in Madison, Wisconsin and generated a seven hour time series of backscatter cross section as a function of height. A high value of backscatter cross section is indicative of a thick cloud. This information as a function of range for a vertically- pointing system provides cloud base, an indication of how optically thick the cloud is and cloud top. Figure 5.11a is figure 10 from the Grund and Eloranta (1990) FIRE article. Compare this to a model- generated time/height cross section for a
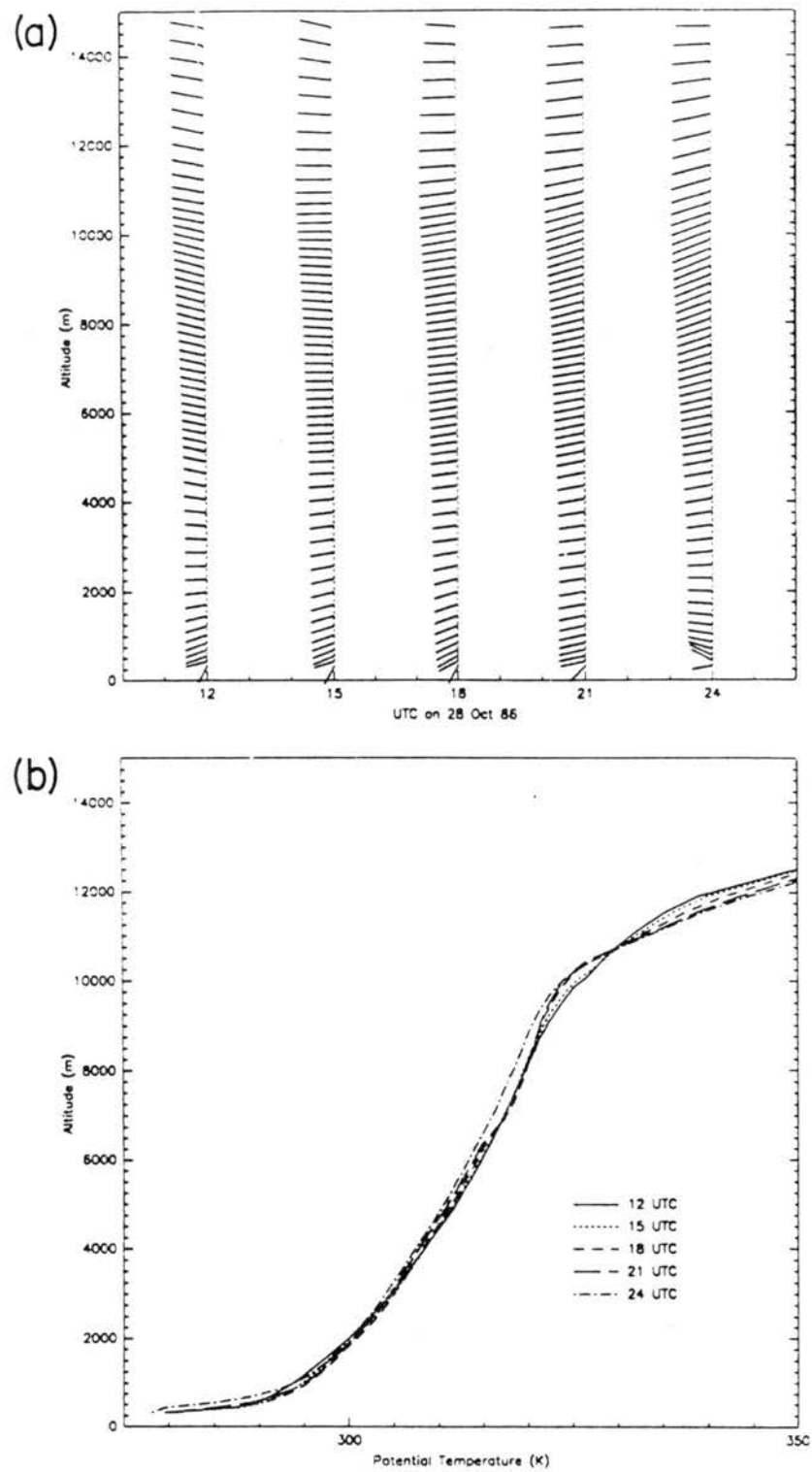
Figure 5.10: Model derived sounding time series for Green Bay, WI. (a) Winds (m/s), (b) Potential temperature (K).

grid point near Madison (Figure 5.11b). While the lidar data shows much more detail in time, the model cloud base, depth and top are very close to that observed. The passage of a period of thicker cloud is also representative of the actual conditions on that day. The clear region observed between 1830 and 1930 UTC does not appear in the model time series.

As mentioned in Chapter 4, ice crystal concentration and ice water content were measured in the pre-clearing cloud layers shortly after 1500 UTC. This roughly coincides with the nested grid cross sections presented in Chapter 6 (Figures 6.4a,b,c,d,e,f). The model predicted maximum concentrations in the generation layer of 30 crystals per liter compared with the 10 per liter measured. It produced 100 per liter in the thicker, altocumulus layer while Heysmfield et al. (1990) measured only 20 per liter. It is very possible that the aircraft missed some areas of higher concentrations but overall, the model compares well. Heysfield et al. measured IWC of 0.02 g/m^3 in the upper cloud at this time. The model produced a value less than 0.05 g/m^3 in this same area (See Figure 6.4f). In the lower cloud, 0.2 g/m^3 was measured and a maximum of 0.6 g/m^3 was simulated.

From Starr and Wylie's summary, there were three layers in the pre-clearing cloud mass. A thin layer at 11.3km, a thicker generation zone at 10 to 10.5km with precipitation streamers extending to an indistinct cloud base at 8.5km. There was also an altocumulus layer from 6 to 8km. This cloud layer exhibited strong internal cellularity. The crystal concentrations shown in Figure 6.4a exhibit such a layering tendency. There are high concentrations at 10km with what seem to be fall streaks extending to 8.5km. Below this there is a thick layer from 6 to 7.5km. The corresponding vertical motion pattern shows convective-like cells.

In addition to a synoptic scale comparison to satellite imagery, it is necessary to compare on a finer scale using higher resolution, more detailed bispectral imagery. This will help determine the models ability to simulate the areal coverage of high and low clouds on the mesoscale.

Figures 5.12a,b,c,d,e show high cloud ice water path from the 33km grid at the times of the bispectral images (Figures A.6 - A.10). Figures 5.13a,b,c,d,e show low cloud ice water path.
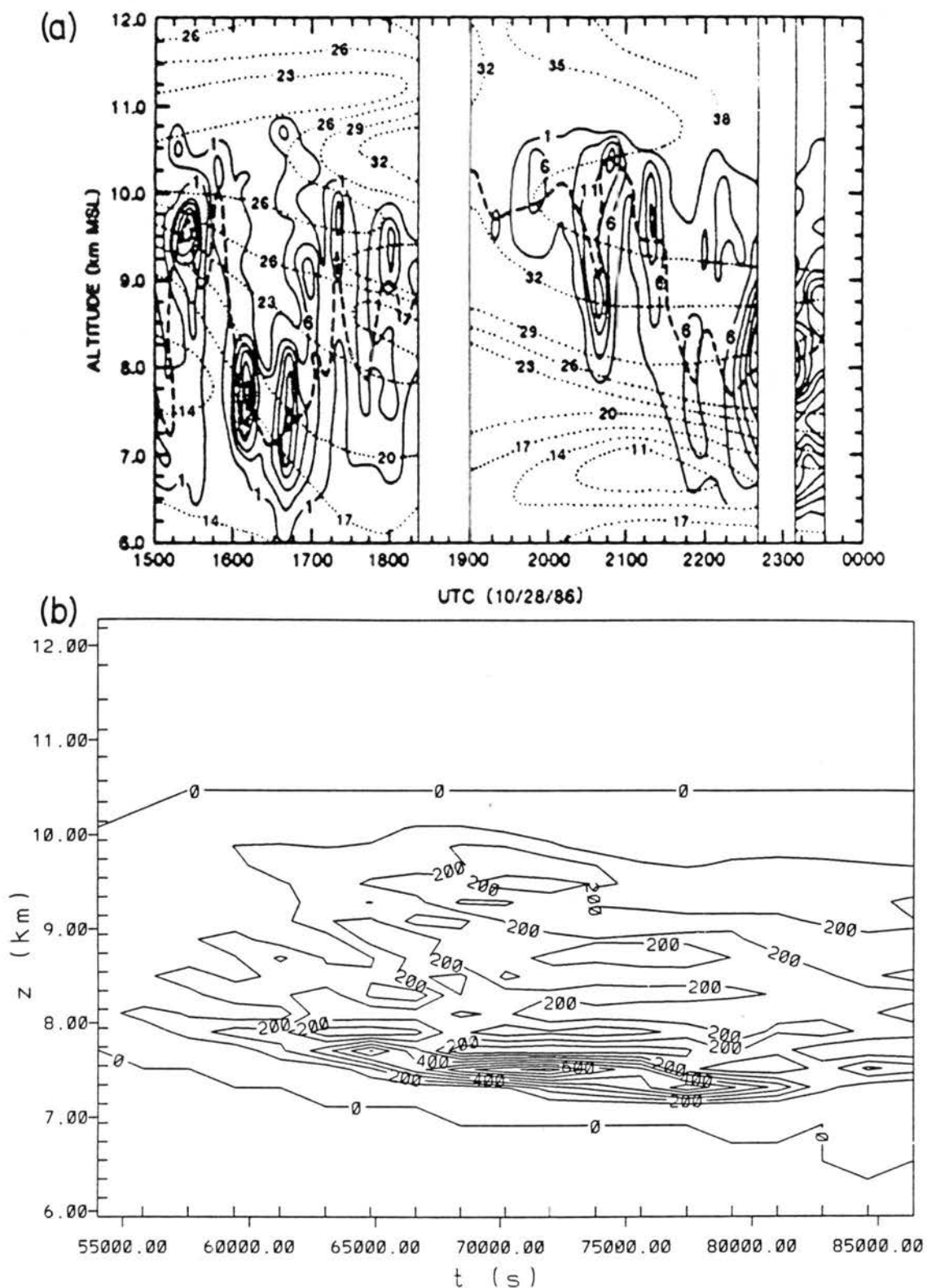
Figure 5.11: Time/height series of (a) backscatter cross section from the HSRL lidar at Madison, WI. Figure taken from Grund and Eloranta, 1990. (b) ice crystal concentration for the grid point nearest Madison, WI. Values are in number of crystals per liter.

Figure 5.12: Ice water path 6-12km at (a) 1330 UTC, (b) 1500 UTC, (c) 1900 UTC, (d) 2030 UTC, (e) 2200 UTC.
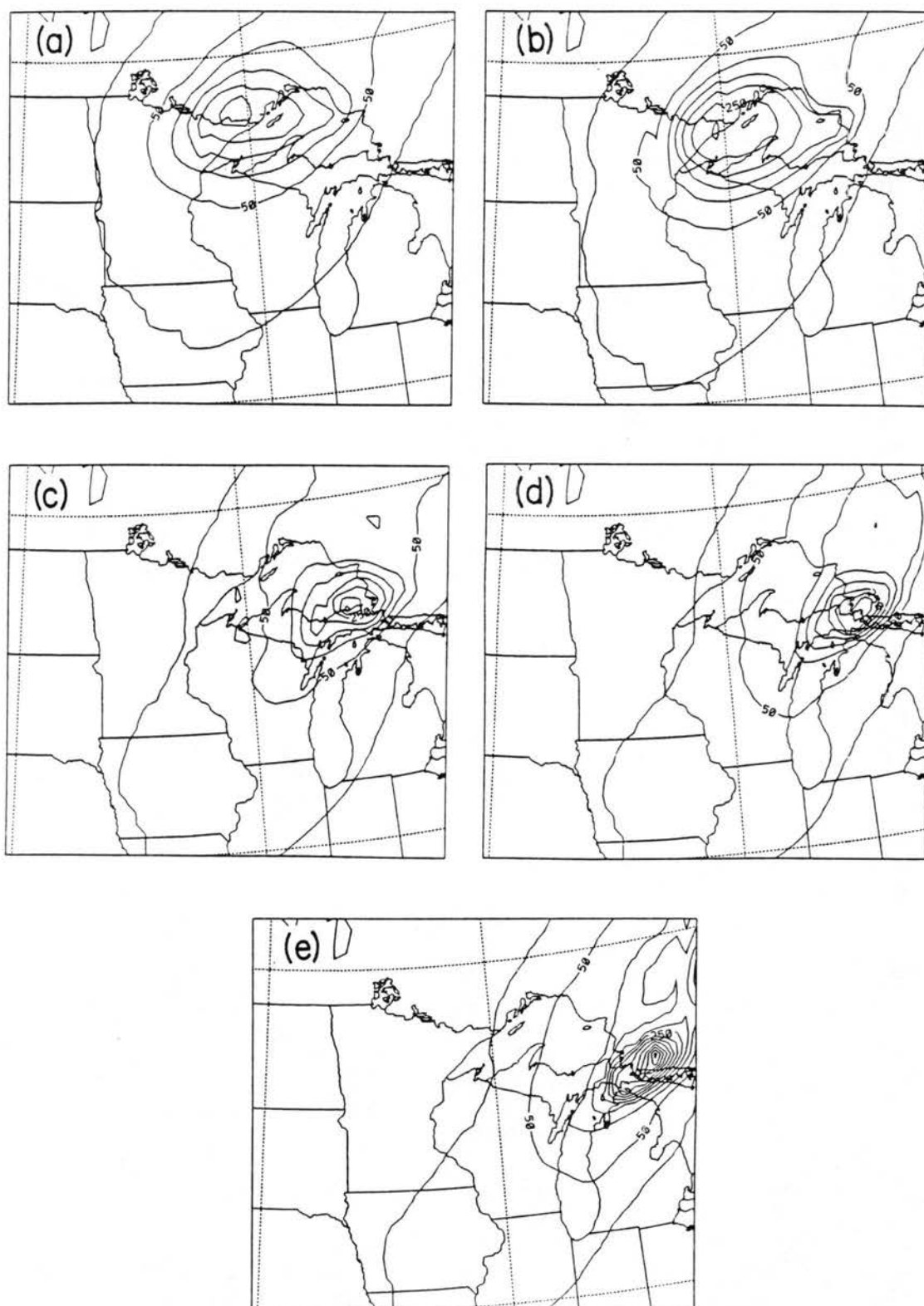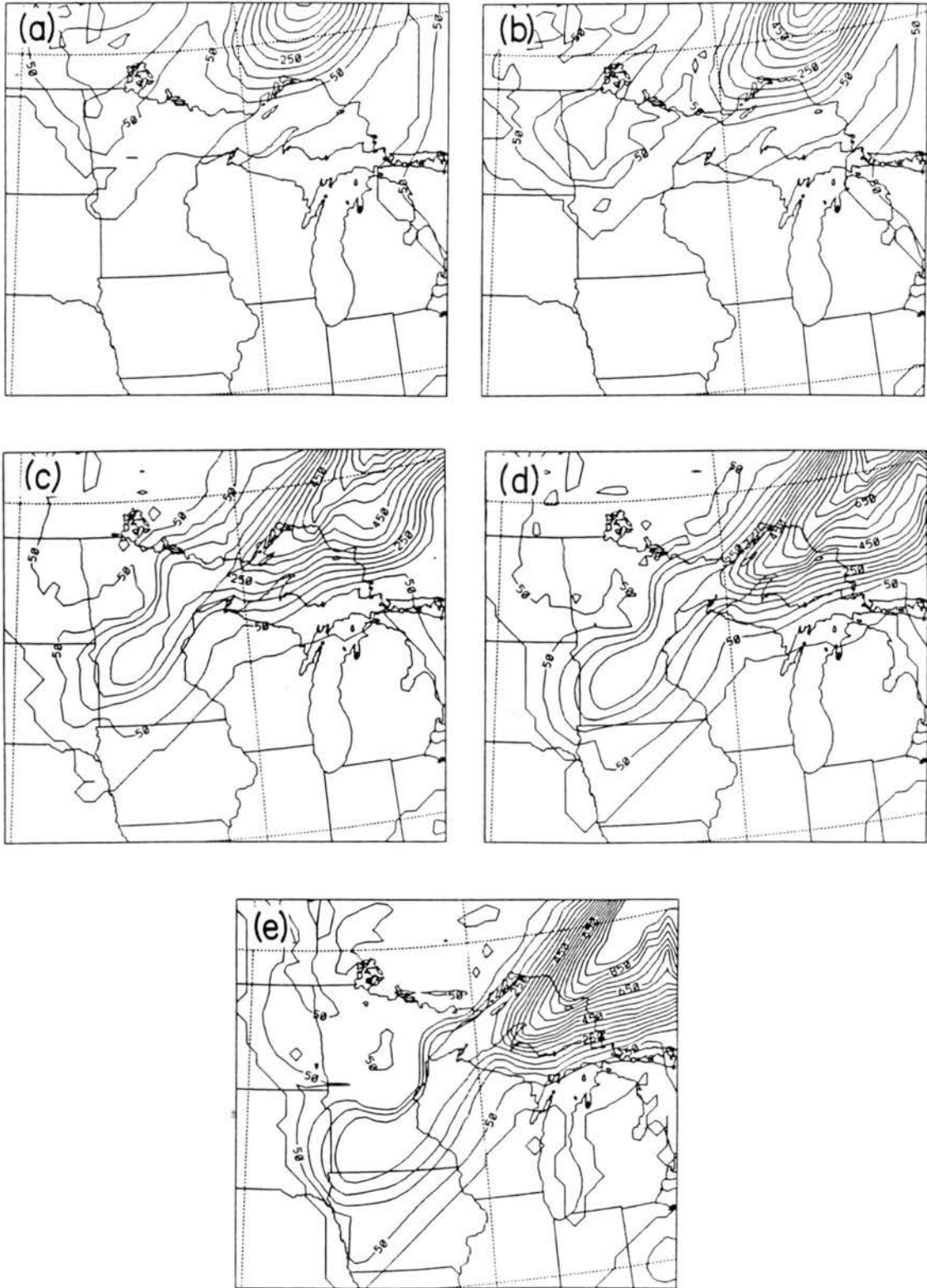
Figure 5.13: Ice water path 0-6km at (a) 1330 UTC, (b) 1500 UTC, (c) 1900 UTC, (d) 2030 UTC, (e) 2200 UTC.

At 1330 UTC, a broad area of high cloud covers most of the FIRE region with the thickest high cloud occuring over northern Minnesota and Lake Superior. This matches particularly well with model simulated IWP. The yellow low cloud/fog (Figure A.6) in Michigan is somewhat evident over Lake Huron in the model IWP output (Figure 5.13a).

By 1500 UTC, the high cloud shield in Figure A.7 has moved east and now covers most of Lake Superior. Thinner cloud extends into Illinois and Iowa. Again, this matches Figure 5.12b very well. There is also some evidence of thick low cloud beneath the thick cirrus shield to the north of Lake Superior and in northern Minnesota. Figure 5.13b shows the model low cloud IWP at 1500 UTC.

Figure A.8 shows the cloud patterns for 1900 UTC. The clearing event is moving out to the east of Wisconsin with an area of enhanced cloudiness ahead over the Upper Peninsula of Michigan, lower Michigan and Lake Michigan. While the high cloud IWP predicted by the control simulation does not go to zero completely, the very lowest contour next to zero matches the clearing line in eastern Wisconsin pretty well. Note the thick low cloud in Minnesota associated with the surface cold front. This feature is also evident in Figure 5.13c.

By 2030 UTC, (Figure A.9) the clearing line has passed over into Lake Michigan but is not as sharp as it was at 1900 UTC. The models high cloud IWP field has spread somewhat but the high IWP matches the thick cloud in the north of Michigan. The newly generated, convective looking cirrus in Iowa and Wisconsin is not generated here but some cloud remains. The thicker generating cells are, of course, much too small for the model to resolve directly.

The low cloud IWP seem to move into Iowa while there is no indication of low cloud there in the 2030 UTC image. However, the broad band of low cloud in Minnesota is represented very well.

2200 UTC is a continuation of the previous images. The high cloud over Iowa and Wisconsin appear thicker although that could be due to the sun angle. The thickest cloud continue to move northeast of Lake Superior and the high cloud IWP moves as well. There is no corresponding IWP maxima over Iowa and Wisconsin. This area of new generation does not appear to be simulated at all. The low cloud pattern continues as before.

Discussion

The control simulation recreated the area of enhanced high cloud that appeared ahead of the clearing line. It did not show a clearing area in the IWP associated with a shortwave disturbance. There is some evidence that the model produced such a disturbance but it was so weak it did not affect the moisture field.

This disturbance appeared in the 1200 UTC satellite imagery and lasted through the period. The simulations in this study did not start the nested grid until 1200 UTC, 12 hours into the simulations. It may be that the information necessary to produce this disturbance in it's full form, was not available on the $100km$ outer grid. It may also be that the pre-disturbance environment was not adequately resolved by the initial data sets. It certainly is not resolved adequately in the standard archived data presented in Chapter 4.

5.4 Comparison with previous RAMS studies

As mentioned in Chapter 2, Nicholls et al. (1990) used RAMS to run a preliminary simulation of the cirrus clouds on 28 Oct 1986. The simulations used version 2A of RAMS and the previous ice nucleation scheme described in Flatau et al. (1989). It had only $500m$ vertical resolution but added a third nested grid with $15km$ resolution. These simulations suggested that the $15km$ grid provided little additional information. This section is a brief comparison of the Nicholls et al. simulation and the control simulation of this study.

Both simulations represented the vertical position of the pre-clearing cloud mass quite well. While there is a hint of layering in the Nicholls simulation, it is obvious in the higher-resolution control simulation. Both represented the fact that the lower altocumulus clouds had a much higher ice water content.

In terms of vertical motion, both simulations show a hint of the shortwave disturbance responsible for the clearing episode. Nicholls et al. show a $0.5cm/s$ downward motion at $8.25km$ over Wisconsin at 1800 UTC while the control simulation showed an area of $1.0cm/s$ downward at $7.5km$ over Wisconsin at 1900 UTC. Neither showed the strong subsidence necessary to evaporate the cloud. The Nicholls simulation continued to show downward motions over Wisconsin at 2100 UTC while the control simulation returned to a broad area of upward motion.

The Nicholls et al. paper showed crystal mixing ratio at $8.25km$ which gives some idea of cloud coverage. These figures match fairly well with infrared imagery except for the post-clearing cirrus. Neither simulation generated the post clearing cirrus at $9 - 11km$.

The control simulation of this study appears to be an improvement. The layering seems to be a result of the higher vertical resolution. It's hard to tell how much of the areal differences are due model changes, different grid configurations or simply different initial conditions. The exact reproduction of the clearing episode may be impossible without a much more complicated data assimilation technique.

Chapter 6

CHARACTERISTICS OF THE SIMULATED CIRRUS LIFECYCLE

In Chapter 4, we described the weather events of 28 Oct 1986 paying particular attention to synoptic and mesoscale features. We described the control simulation from this study in Chapter 5 and showed that there was good agreement between the model solution and the observations of that day. Because of this good agreement, we have some confidence that RAMS, in this configuration, is capable of simulating cirrus clouds on synoptic and mesoscales. As a result, we should be able to use RAMS to determine characteristics of the cirrus lifecycle.

In this chapter, we describe the time and space evolution of the simulated cirrus clouds and their surrounding environment by presenting space cross sections of these variables on the $33km$ nested grid, at 1500 UTC, 1900 UTC and 2200 UTC. Using cross sections we will attempt to show relationships between stability, humidity, vertical motion, horizontal motion, ice crystal concentration and ice water content between 5 and 10 km. Note also that the times selected match the bispectral satellite imagery in Figures A.7, A.8, and A.10.

Because of the volume of data produced by the control simulation, only a representative portion could be shown in it's raw form. The following sections refer to four cross sections of four different variables at three different times. While this can't be considered completely representative, it does allow some relationships to be shown and some conclusions to be drawn. Figures 6.1 - 6.4 are cross sections valid for 1500 UTC. Figures 6.5 - 6.8 are at 1900 UTC and figures 6.9 - 6.12 are for 2200 UTC. The remaining sections of this chapter will be organized around specific observations made from these figures.

(a)

Ice Conc per L

(b)

W cm/s

(c)

Rel Hum Ice

(d)

Figure 6.1: Horizontal cross sections at 10 km for 1500 UTC of (a) crystal concentration (*crystals/liter*), (b) vertical motion (*cm/s*), (c) RHi (%), (d) vector winds (*m/s*).

(a)

(b)

Ice Conc per L

W cm/s

(c)

(d)

Rel Hum Ice

Figure 6.2: Horizontal cross sections at 7.5 km for 1500 UTC of (a) crystal concentration (*crystals/liter*), (b) vertical motion (*cm/s*), (c) RHi (%), (d) vector winds (*m/s*).

Figure 6.3: Horizontal cross sections at 5 km for 1500 UTC of (a) crystal concentration (*crystals/liter*), (b) vertical motion (*cm/s*), (c) RHi (%), (d) vector winds (*m/s*).

83

Figure 6.4: Vertical cross section at $j = 25$ on the nested grid for 1500 UTC of (a) crystal concentration ($crystals/liter$), (b) vertical motion (cm/s), (c) RHi (%), (d) potential temperature (^oK), (e) ice water content (g/m^3), (f) horizontal windspeed (m/s).

Figure 6.4: Continued.

(a)

Ice Conc per L

(b)

W cm/s

(c)

Rel Hum Ice

(d)
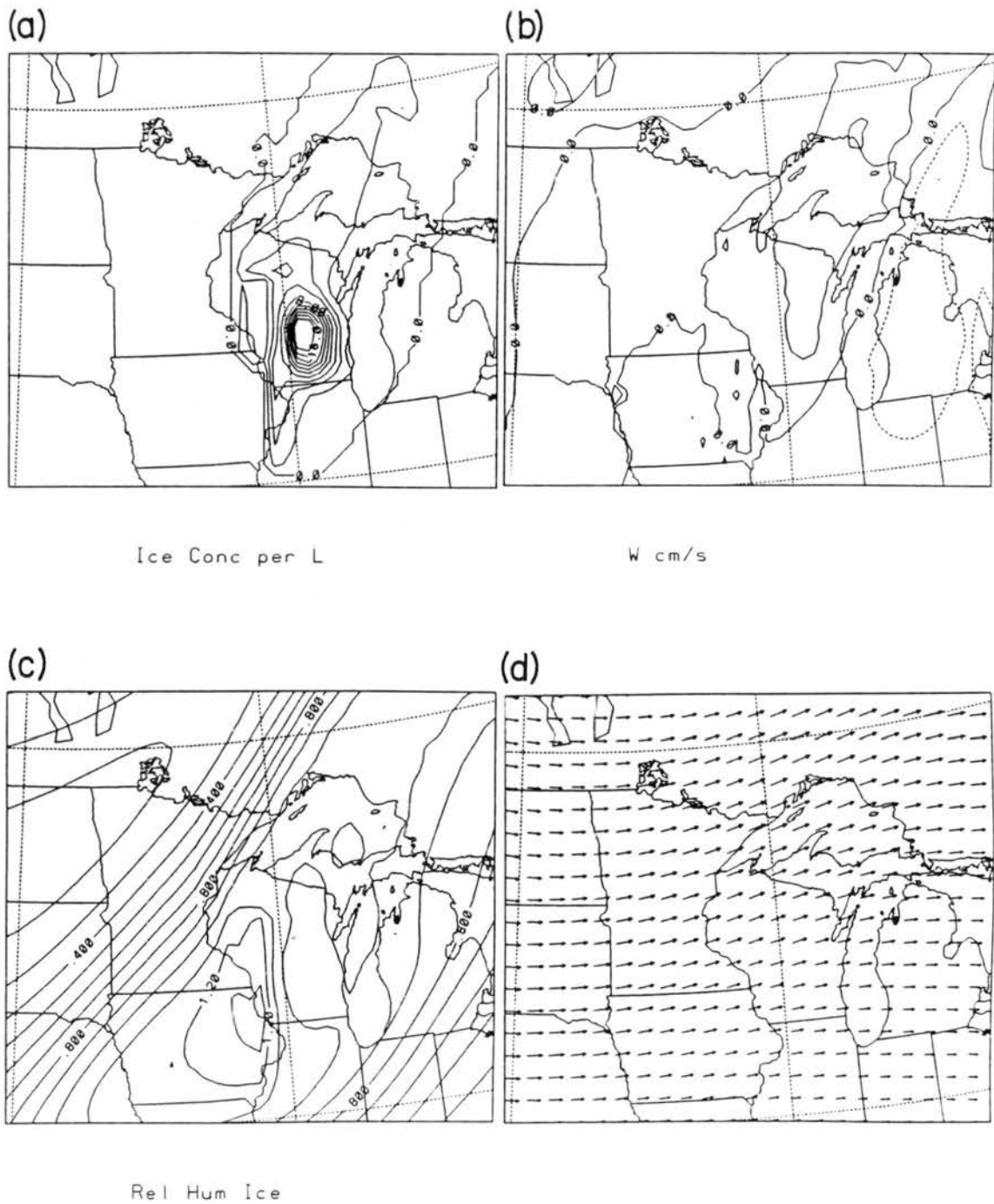
Figure 6.5: Horizontal cross sections at 10 km for 1900 UTC of (a) crystal concentration (*crystals/liter*), (b) vertical motion (*cm/s*), (c) RHi (%), (d) vector winds (*m/s*).
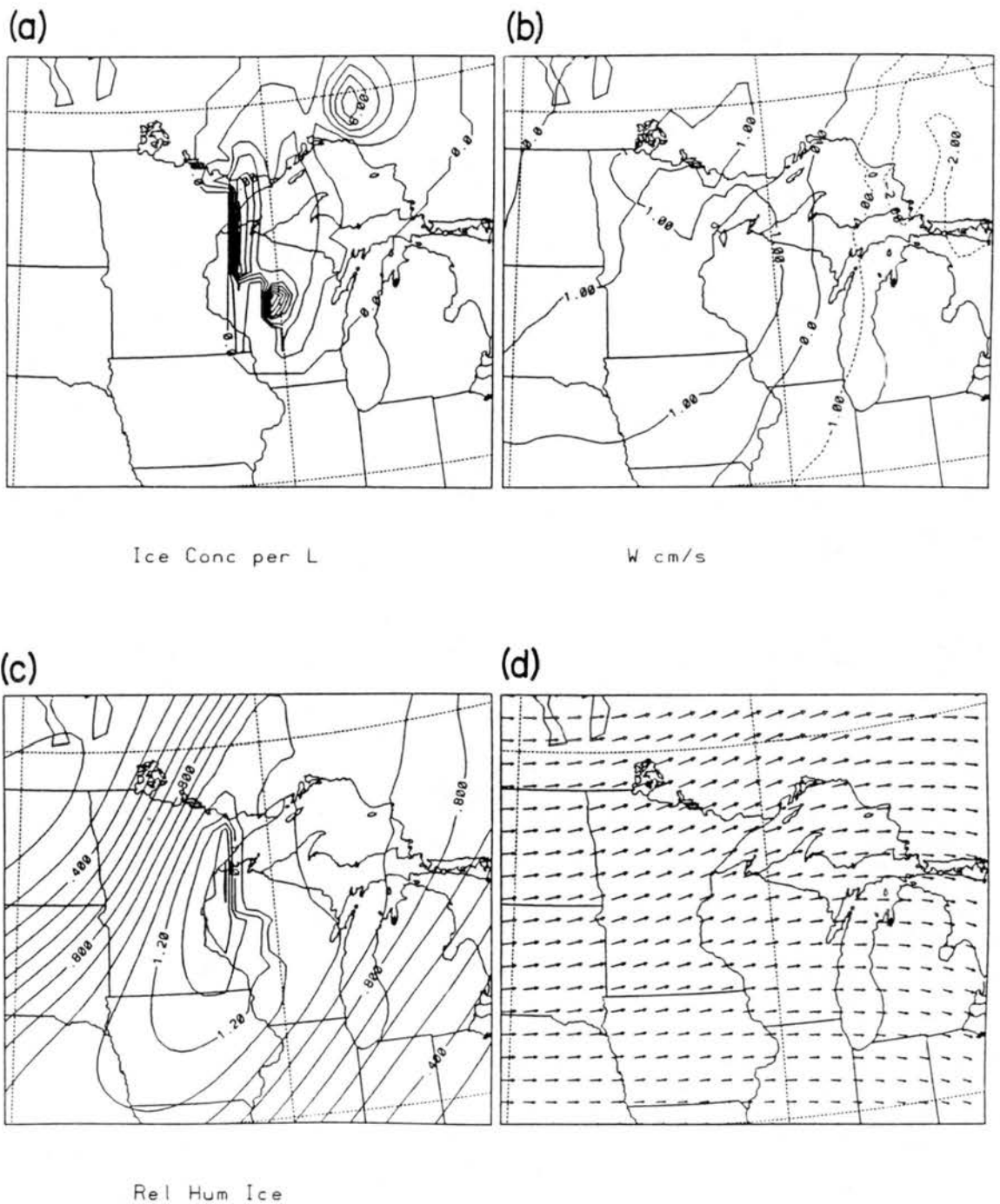
86

Figure 6.6: Horizontal cross sections at 7.5 km for 1900 UTC of (a) crystal concentration (*crystals/liter*), (b) vertical motion (*cm/s*), (c) RHi (%), (d) vector winds (*m/s*).

(a)

Ice Conc per L

(b)

W cm/s

(c)

Rel Hum Ice

(d)
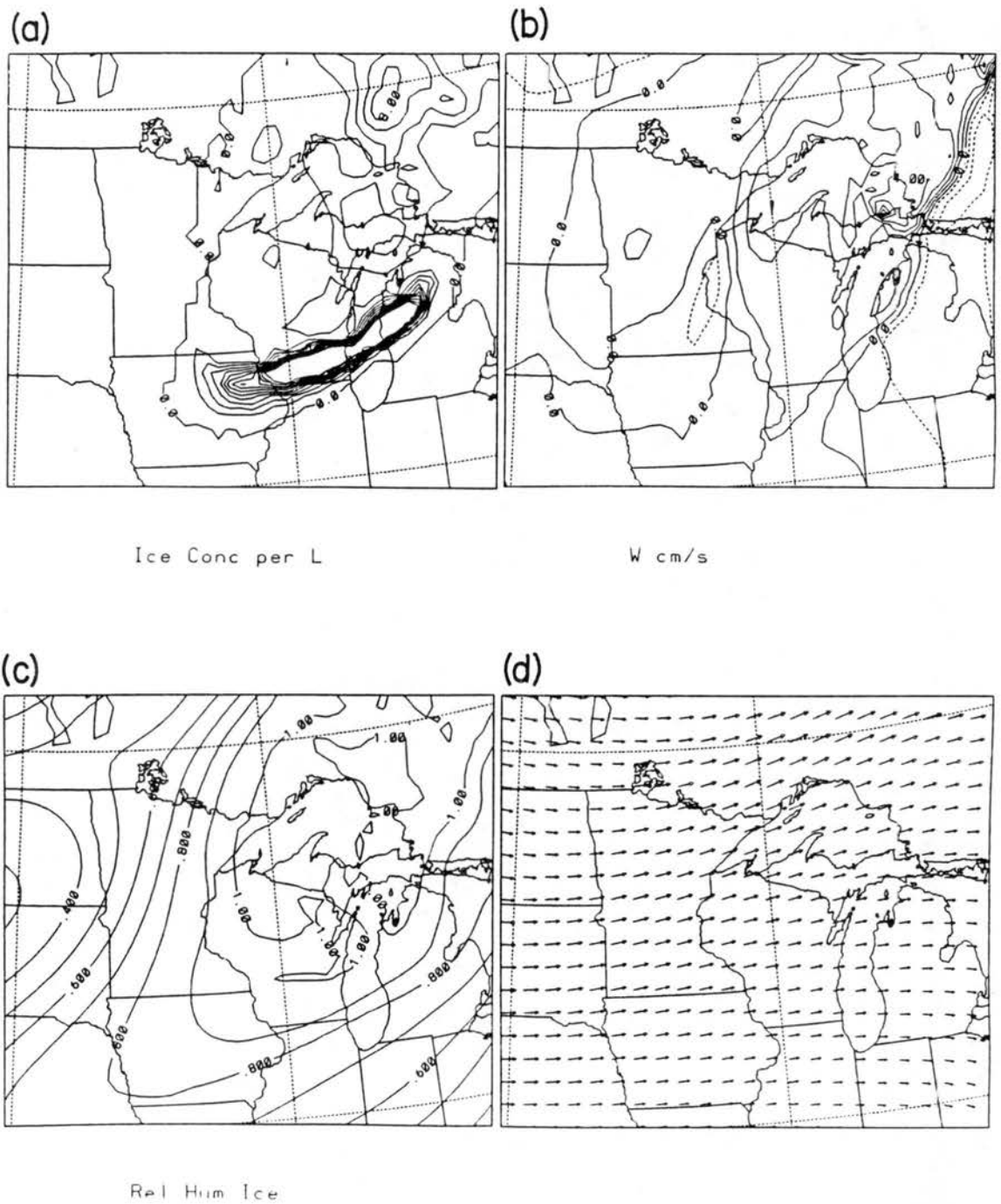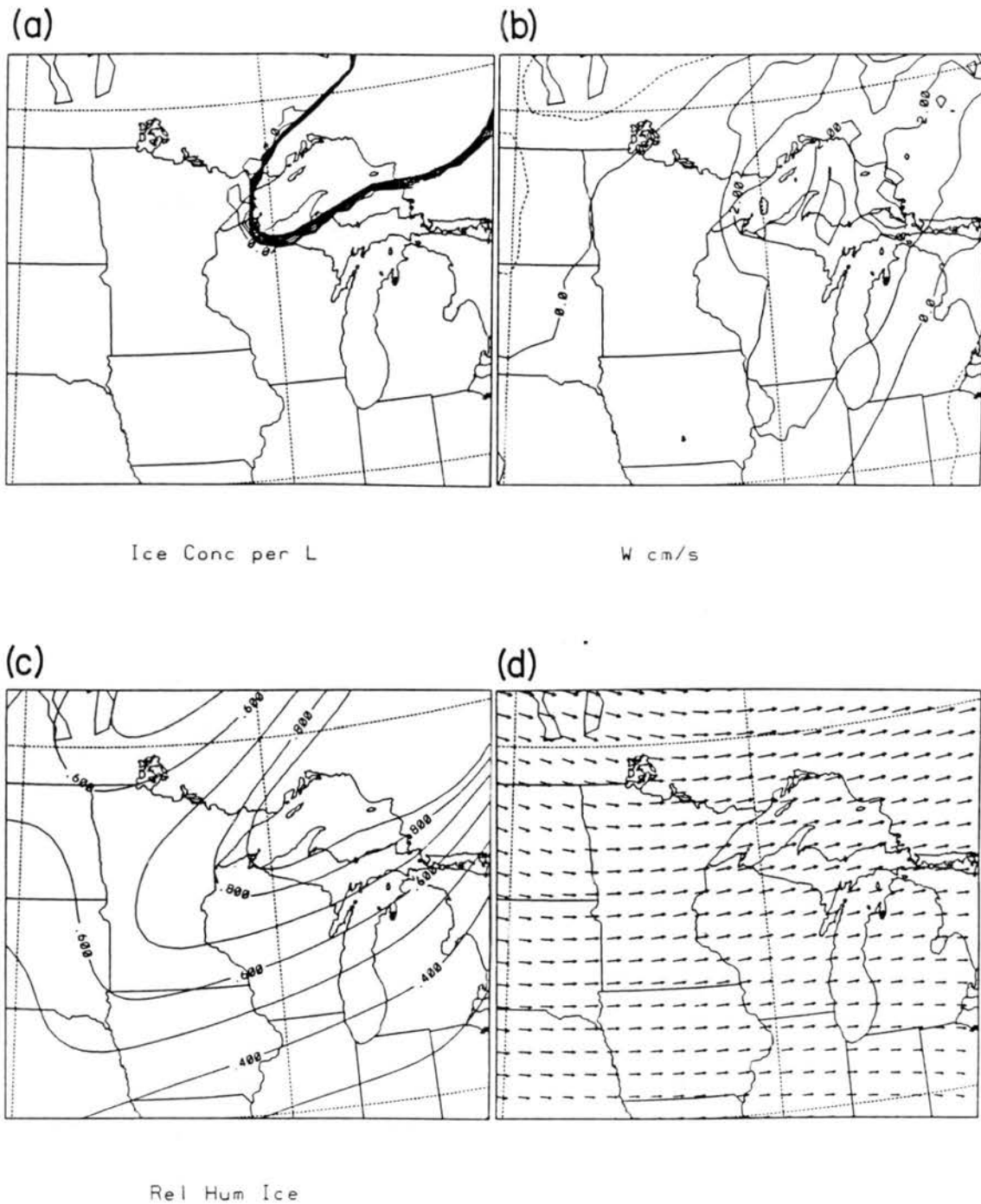
Figure 6.7: Horizontal cross sections at 5 km for 1900 UTC of (a) crystal concentration (*crystals/liter*), (b) vertical motion (*cm/s*), (c) RHi (%), (d) vector winds (*m/s*).
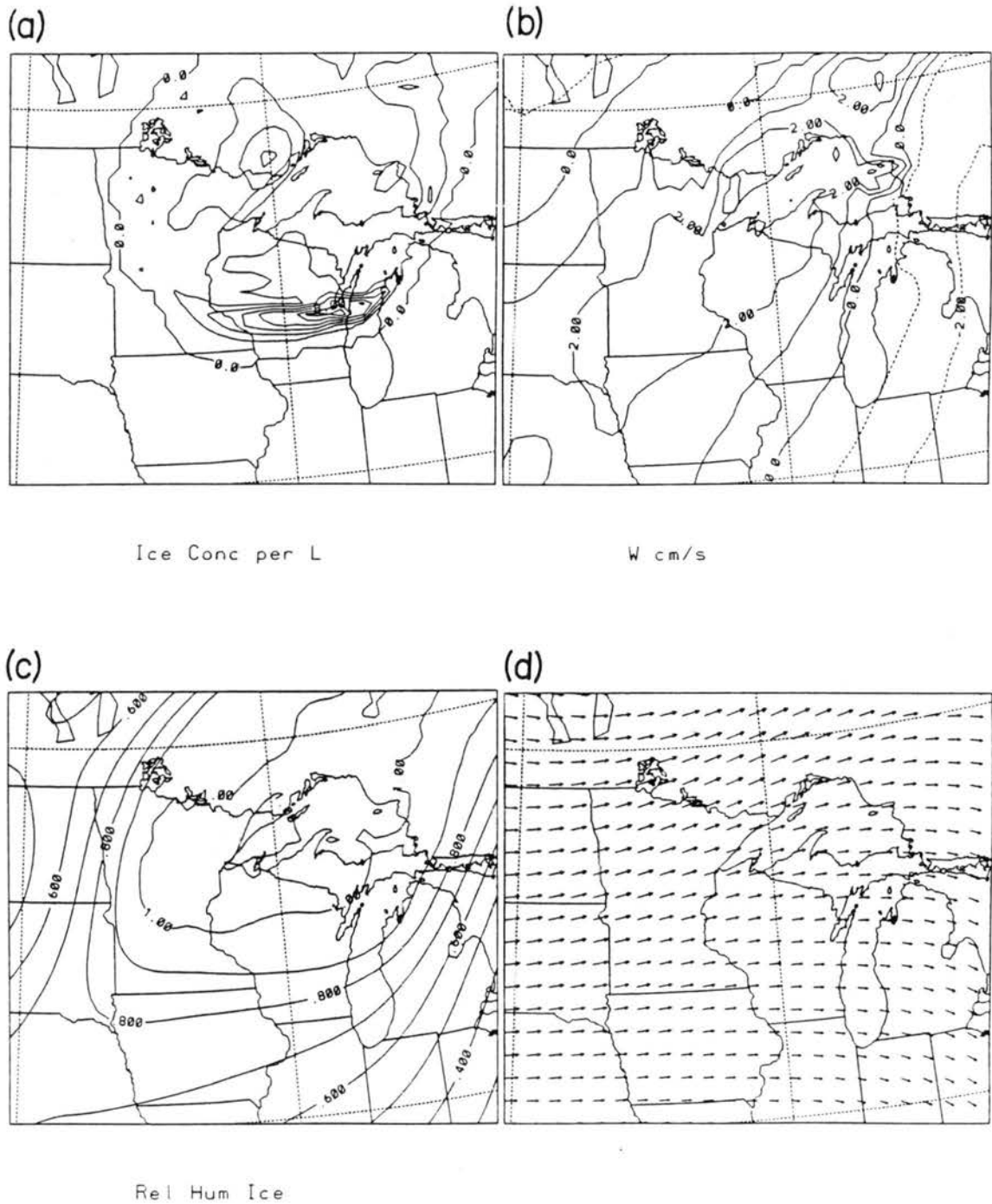
Figure 6.8: Vertical cross section at $j = 25$ on the nested grid for 1900 UTC of (a) crystal concentration ($crystals/liter$), (b) vertical motion (cm/s), (c) RHi (%), (d) potential temperature (^oK), (e) ice water content (g/m^3), (f) horizontal windspeed (m/s).

89

Figure 6.8: Continued.
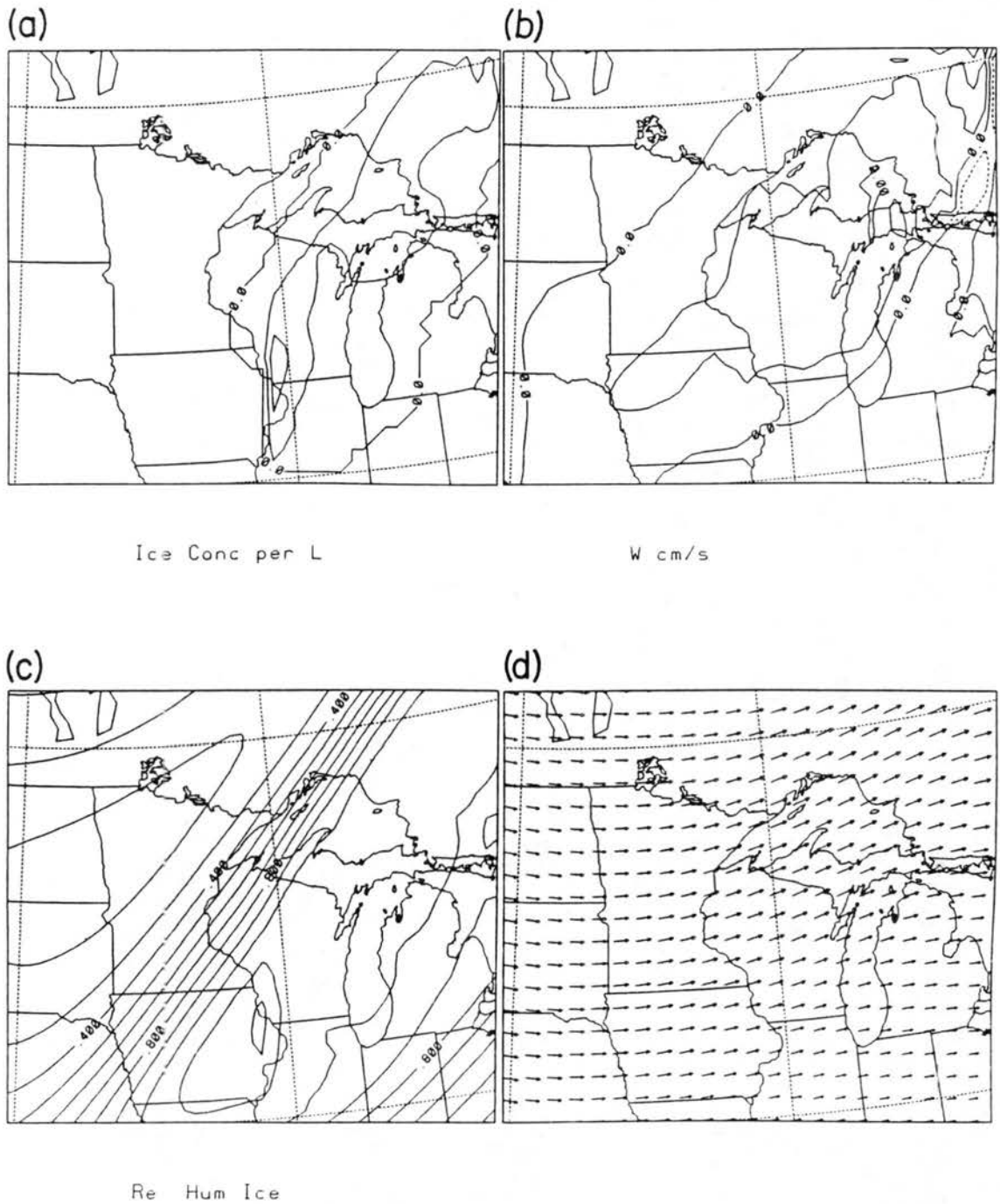
Figure 6.9: Horizontal cross sections at 10 km for 2200 UTC of (a) crystal concentration (*crystals/liter*), (b) vertical motion (*cm/s*), (c) RHi (%), (d) vector winds (*m/s*).
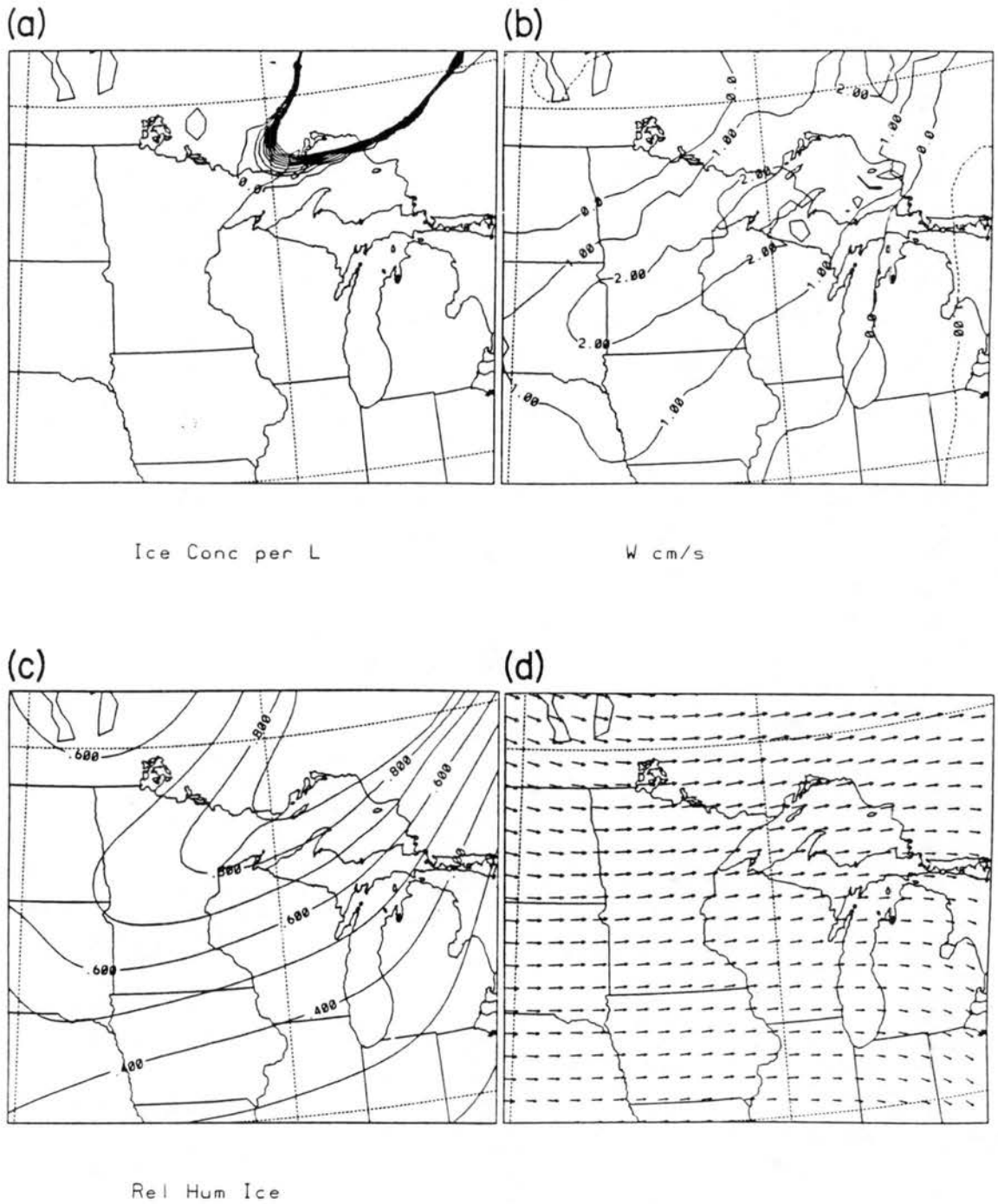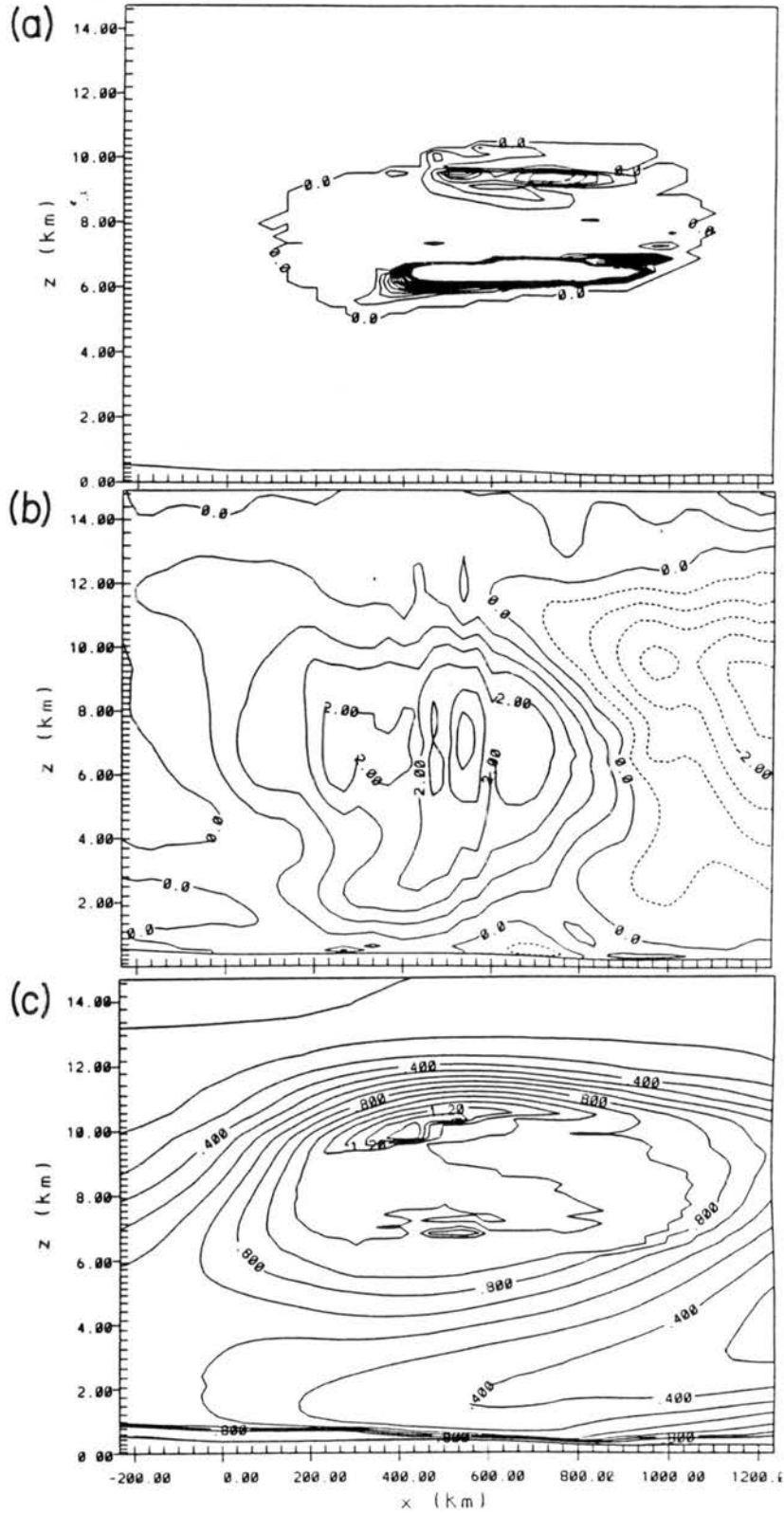
(a)

(b)

Ice Conc per L

W cm/s

(c)

(d)

Rel Hum Ice
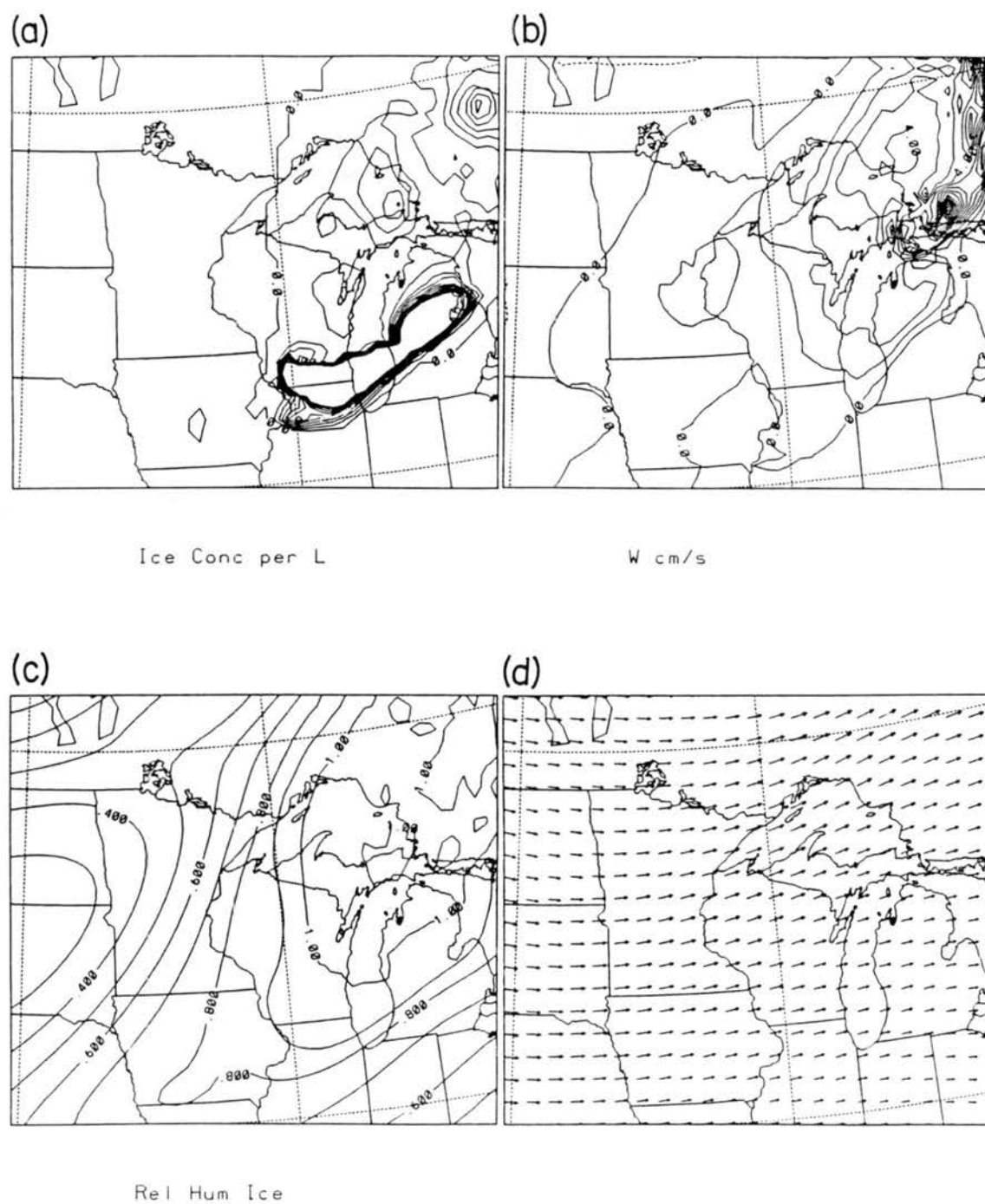
Figure 6.10: Horizontal cross sections at 7.5 km for 2200 UTC of (a) crystal concentration (*crystals/liter*), (b) vertical motion (*cm/s*), (c) RHi (%), (d) vector winds (*m/s*).
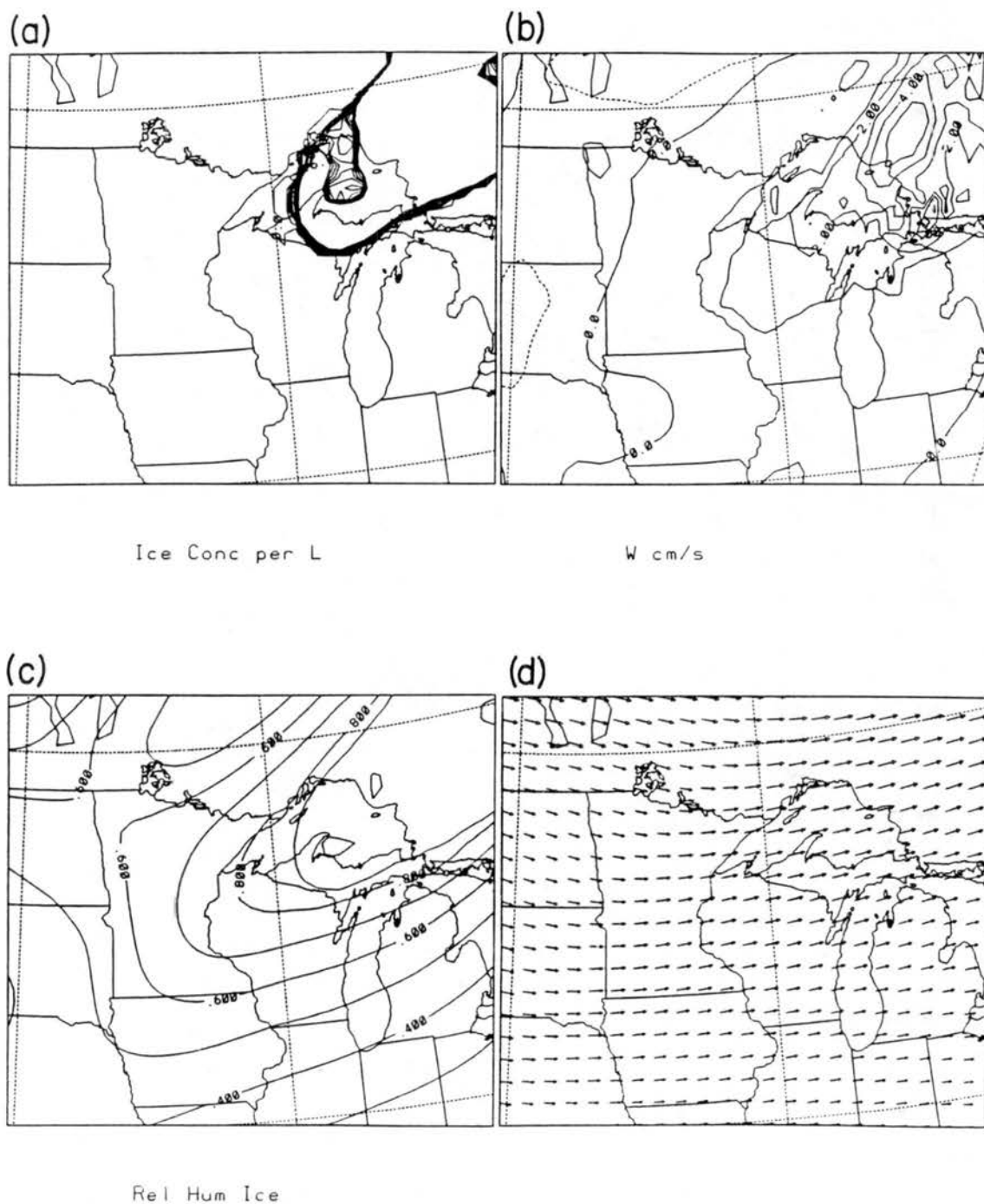
Figure 6.11: Horizontal cross sections at 5 km for 2200 UTC of (a) crystal concentration (*crystals/liter*), (b) vertical motion (*cm/s*), (c) RHi (%), (d) vector winds (*m/s*).

Figure 6.12: Vertical cross section at $j = 25$ on the nested grid for 2200 UTC of (a) crystal concentration ($crystals/liter$), (b) vertical motion (cm/s), (c) RHi (%), (d) potential temperature (^oK), (e) ice water content (g/m^3), (f) horizontal windspeed (m/s).
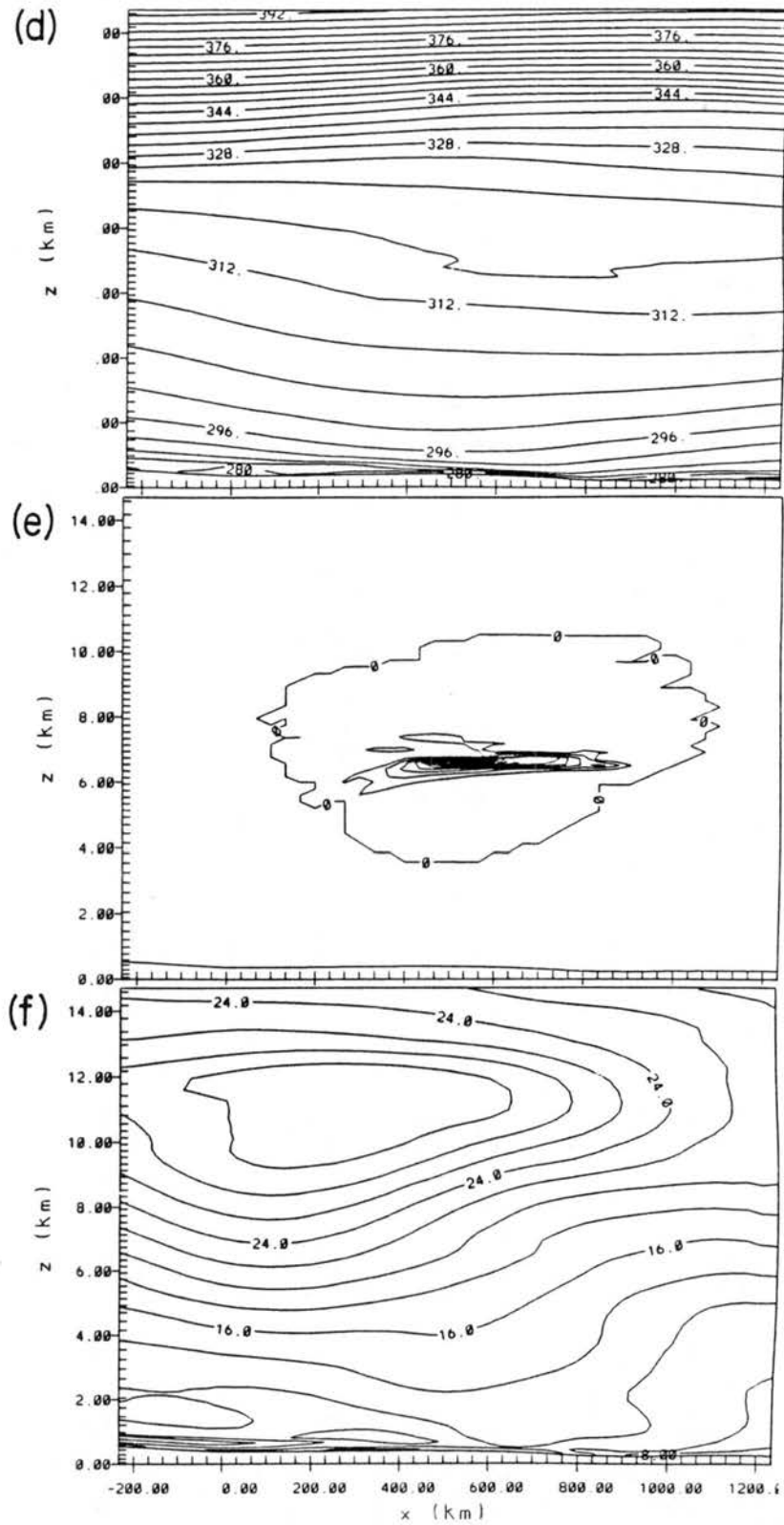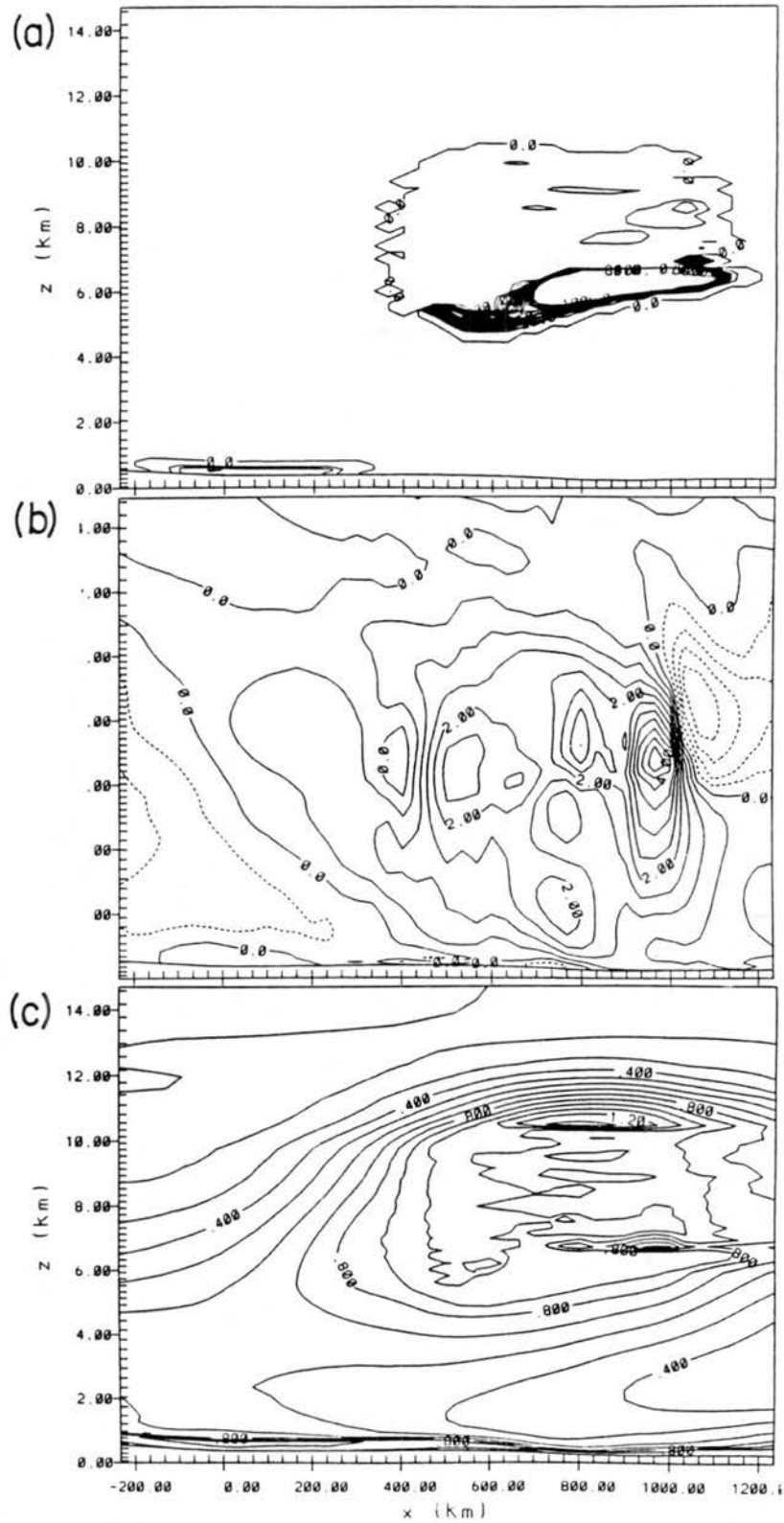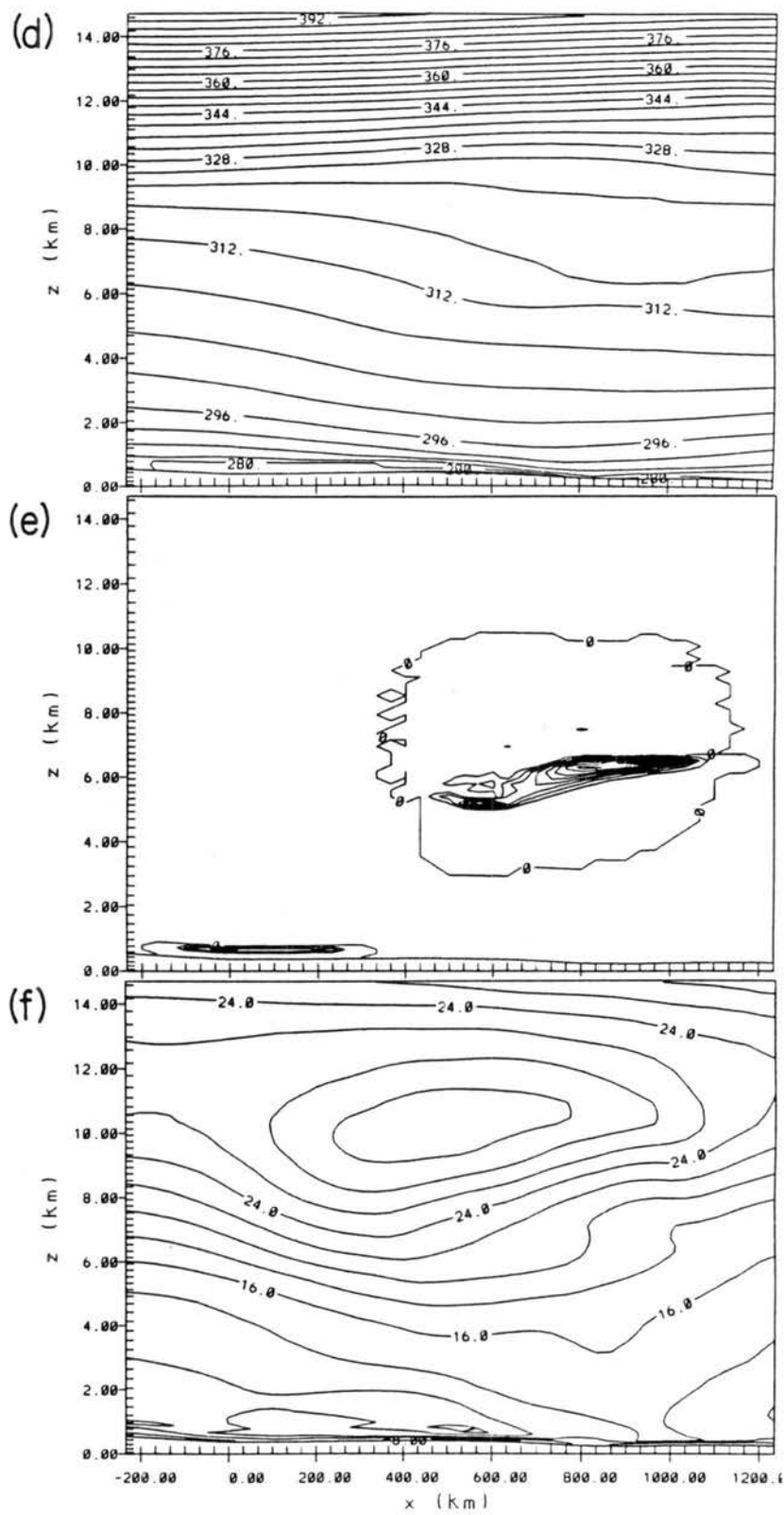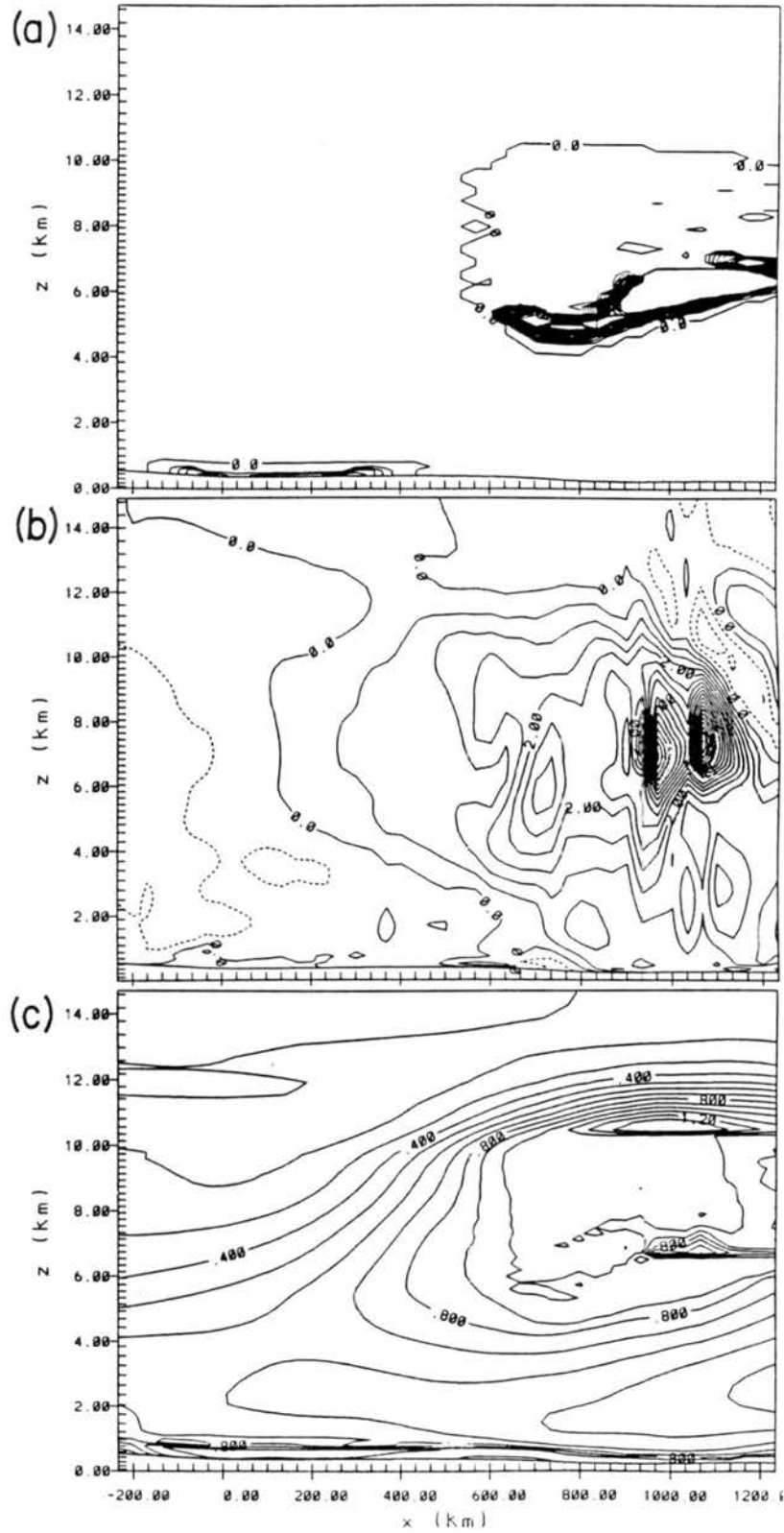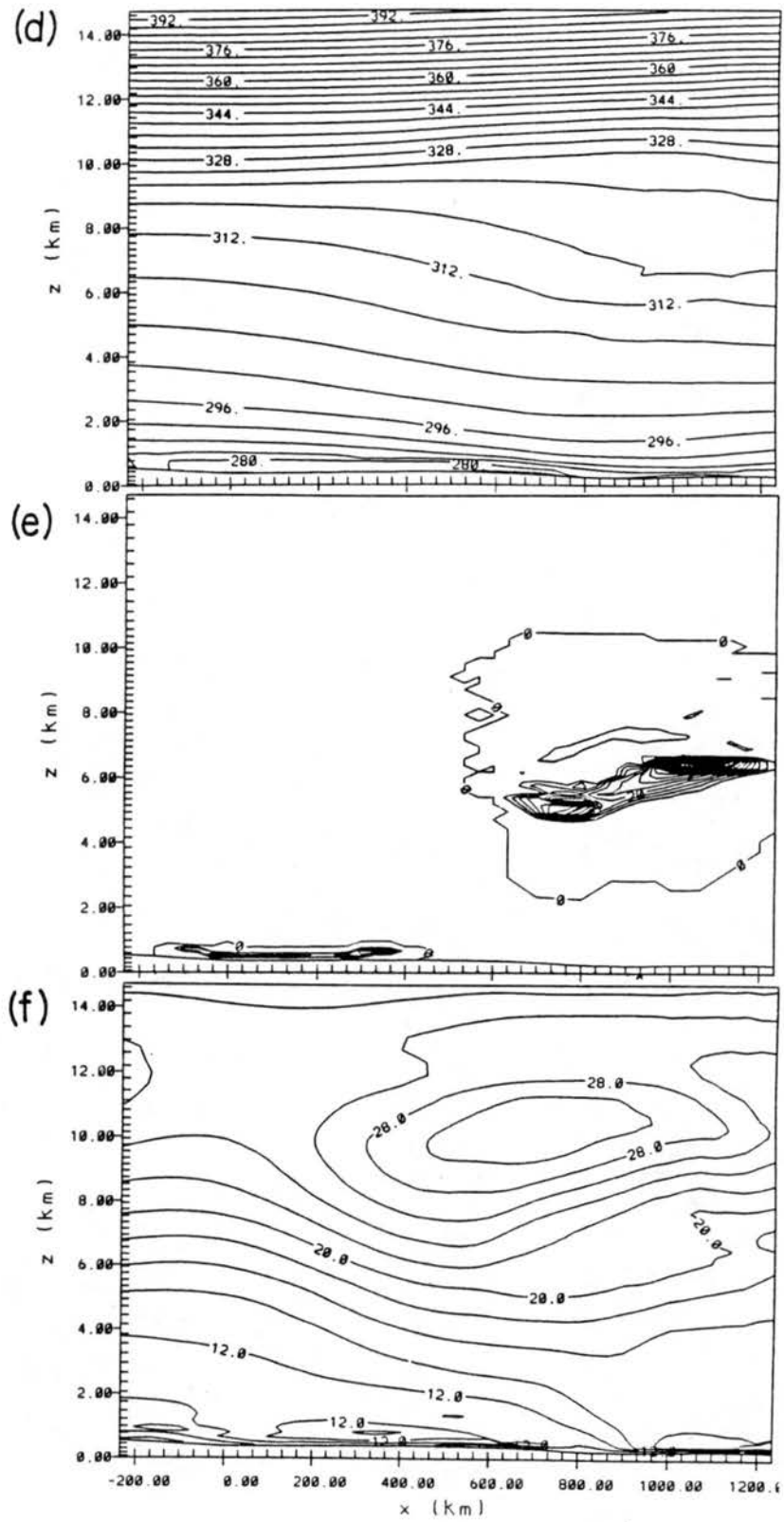
Figure 6.12: Continued.

6.1 Correlation between humidity and vertical motion

Figures 6.1b and 6.1c show that the broad area of upward motion corresponds roughly to the high humidity, but there can be low humidity in the upward air and high humidity in the downward air. These differences can be attributed to the humidity of the air parcels respective source regions. This argument has been used by Durran (1988) to explain the sharp edges of jetstream cirrus. This point may seem obvious, but it is important to realize when considering formulating a cirrus cloud parameterization based on vertical motion. Lifting may not always cause saturation and subsidence may not always cause evaporation.

6.2 Correlation between humidity and crystal concentration

There appear to be two relations between areas of high humidity and areas of high crystal concentration. Crystal generation appears to occur at cloud top in areas of 120% relative humidity with respect to ice (RHi) and crystals remain in areas of RHi greater than 80%. The vertical cross sections show this point best, although it is also evident in the horizontal cross section as well.

Figures 6.4a and 6.4b show vertical profiles of crystal concentration and RHi. The zero crystal contours stay within 80% RHi area as a rule. Crystal generation at cloud top occurs at maximum RHi. Crystals are generated at high RHi, and evaporated at low RHi. This may explain cirrus locations, variability, and layering as simply horizontal and vertical variations of moisture content.

The variable in this equation is activated ice nuclei. High humidities can exist without crystals as was observed in the FIRE experiment (Starr and Wylie, 1990). Ice saturated layers were observed outside of clouds. This is also observed in the model simulation where 120% supersaturation RHi occurs outside of the cloud.

Attempts to research the complexity of this relationship are further hampered by the lack of reliable humidity measurements at cirrus temperatures. New instruments are being designed and tested in preparation for the next FIRE field experiment.

6.3 Crystal generation, precipitation and evaporation

Crystal generation appears to occur adjacent to areas of high ice supersaturations through a depositional growth process. Ice crystal growth then reduces the local supersaturations to 100%. This generation area is located downwind of the maximum RHi at the top of the cloud.

Fall streaks appear as higher concentration areas below the generation zones in Figure 6.4a, and as high concentrations below and downwind of cloud top high concentration areas. (Note the area relationships in Figures 6.1a and 6.2a) These crystals fall through saturated air (100% RHi) into layers of high humidity below. This may initiate crystal generation in other layers and may be a mechanism for layering in these clouds. This natural seeding mechanism of cirrus generation is discussed in Starr and Cox (1985a)

As the crystals continue to fall, they reach an area of lower humidity and begin to evaporate. This increases the cloud base humidity and allows other crystals to fall further, lowering the cloud base. Starr and Cox (1985a) described this process in their cirrus modeling study. Note that the cloud base drops $1.5km$ between 1500 UTC and 2200 UTC in figures 6.4a and 6.12a.

What is much harder to explain is the apparent accumulation of crystals at cloud base. Concentrations here are 10 times that in the cloud top generating areas. There are several possible explanations. First, crystals are being slowed by stronger vertical motions causing convergence in the vertical. Second, horizontal convergence of crystals occurs at this location. Finally, crystals are being generated at this level.

The first may be occurring. The upward motion is stronger in the lower layer (Compare Figures 6.8a and 6.8b). However, the terminal velocity of these particles is dependent on the diameter. The diameter is diagnosed from the prognosed concentration and the prognosed mixing ratio. It could be that the particle fall velocities are slowing down in this region as well, causing crystal convergence in the vertical.

Horizontal convergence is unlikely. Figures 6.1a, 6.2a and 6.2d show that the higher concentration area does appear below and downstream of the generation area at $10km$. Crystals appear to follow a trajectory based on this flow and their fallspeed.

Higher vertical motions could be creating local supersaturations and therefore a preferred region for crystal generation.

So, it appears that the thicker $6 - 8km$ layer is a consequence of crystal convergence and some generation resulting from the locally higher vertical motions.

This precipitation and nucleation process would explain some instances of layering. Crystals generate at high levels in an area of high humidity. They fall through subsaturated air and into layers with higher humidity, where they initiate further crystal generation. High horizontal wind speeds and high static stability would create large shallow layers where these conditions would occur.

Generation of crystals appears to be a local phenomena. High horizontal winds spread these crystals over large areas. Figure 6.1a shows that lower concentrations of crystals occur well downstream of an organized generating zone.

6.4 Locations of high humidity areas

Figures 6.1c, 6.2c, 6.3c, and 6.4c show the location of the areas of high relative humidity. This is noteworthy because at temperatures below -40^oC, it cannot be measured accurately. These figures show that large areas of ice saturated air may exist at high altitudes, cut off from substantial dynamical forcing for long periods of time. Figure 6.9c shows an area over Iowa, far away from the Canadian storm system. Note that there is very little extension of this area to lower levels in Figures 6.10c and 6.11c.

This characteristic of the moisture field may explain the persistent nature of cirrus. Clouds that are generated can then remain in an area of favorable humidity for long periods of time. This would not be the case if not for the existance of large areas of weak vertical motion at these altitudes.

Chapter 7

SENSITIVITY STUDIES

Sensitivity studies are numerical modeling's strong suit. Once the phenomena has been simulated and verified, parameters and whole processes can be changed or removed altogether. Such is the case with this study. We've described the control simulation results in previous chapters and have compared them to the observed events. From these comparisons, we've concluded that the RAMS model did a good job simulating most of the cirrus-related weather phenomena. In this chapter, we describe three sensitivity simulations and their results. In the first, we excluded the longwave absorption and emission by condensate. The second simulation excluded the shortwave absorption by condensate. The third excluded condensate itself, allowing water vapor to remain.

For clarity, the various simulations are assigned acronyms. The control run will be referred to as CNTL. The run with the longwave effects of condensate turned off is NLW. The run that tested shortwave radiative effects is NSW. And finally, the run with no condensate is NC.

The results of these sensitivity studies are presented as comparisons to the control run. By performing this comparison, we hope to gain some insight into the effects the radiative processes have on cirrus clouds and the effects the cirrus clouds have on the atmospheric structure.

7.1 NLW - The longwave effects on clouds

7.1.1 Description

For this sensitivity study, we wanted to eliminate the absorption and emission of longwave radiation by clouds (condensate) without losing radiative heating/ cooling of the air and ground. In the Chen and Cotton (1983a) scheme, there is a section of code that checks

for condensate in the column. If it is found, then the radiative flux resulting from this condensate is determined at all levels.

As an aside, the computational costs of this section of computer code is proportional to the number of vertical levels squared and it doesn't vectorize well on a Cray supercomputer. As a result of using 69 vertical levels, this one section of code used roughly 70% of the total CPU cycles for these simulations. This computational penalty would obviously affect the number of levels that could be used in a forecast or climate model.

For the NLW simulation, the test for condensate was set to always fail so that no cloud effects would be calculated.

7.1.2 Results

Figure 7.2a shows the high cloud IWP for 1900 UTC of the NLW simulation and should be compared with Figure 5.12c. The most obvious difference is the much smaller IWP value found in the maxima over the upper peninsula of Michigan. There apparently was less crystal generation in this area without longwave radiative effects.

Compared with Figure 5.13c, the enhanced clouds associated with the surface front are not simulated (Figure 7.2b).

Figure 7.3a shows that the cloud base maximum in ice water content is substantially less than that in the CNTL run which is shown in Figure 6.8e.

The 1900 UTC cross section of vertical motion is shown in Figure 7.3b. Compared to Figure 6.8b, this vertical motion pattern is lower amplitude and less cellular in the $6 - 8km$ region.

The potential temperature pattern at 1900 UTC is in Figure 7.3c. (Compare to Figure 6.8d.)

A comparison of lapse rates for all the simulations and the observed case is shown in Figure 7.1. This shows the potential temperature as a function of height in the cirrus cloud layers. It should be noted that from satellite imagery, it seems Sault Ste. Marie, Michigan was not overcast at the time of the rawinsonde flight at 2100 UTC. This comparison shows the NLW cloud base to be $\approx 2.5^oC$ cooler and the cloud top to be $\approx 1.5^oC$ warmer than the CNTL cloud. The result is a much more stable lapse rate.
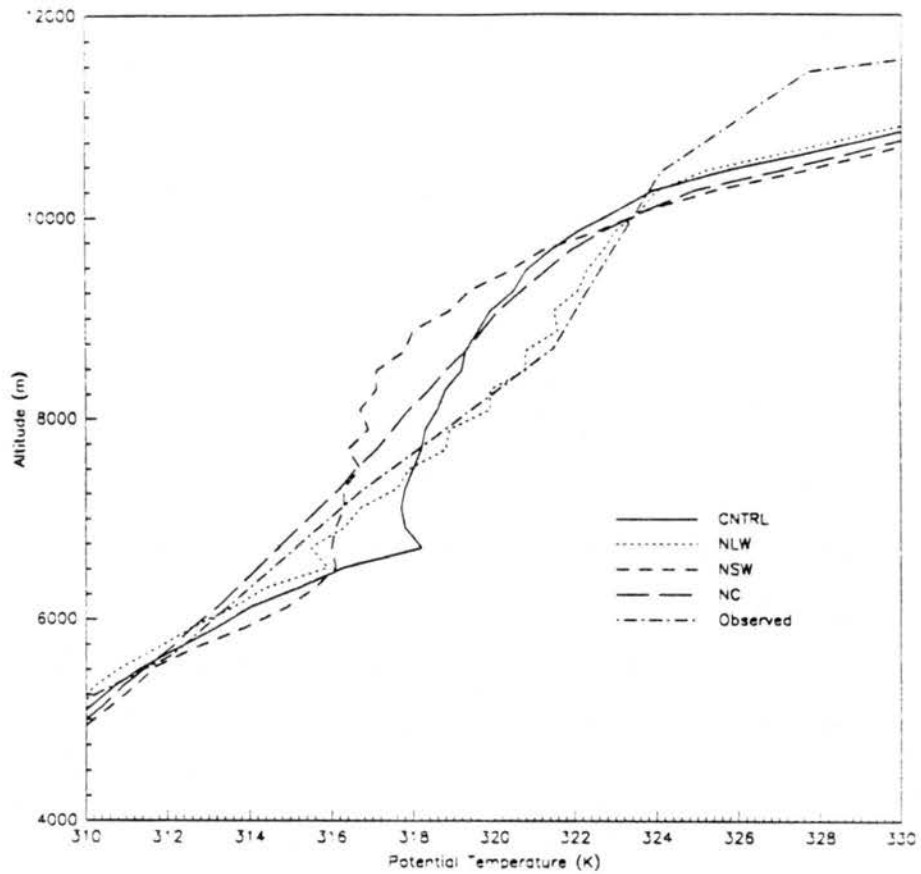
Figure 7.1: Sounding comparison for Sault Ste. Marie, MI at 2100 UTC for all runs and the observed case.
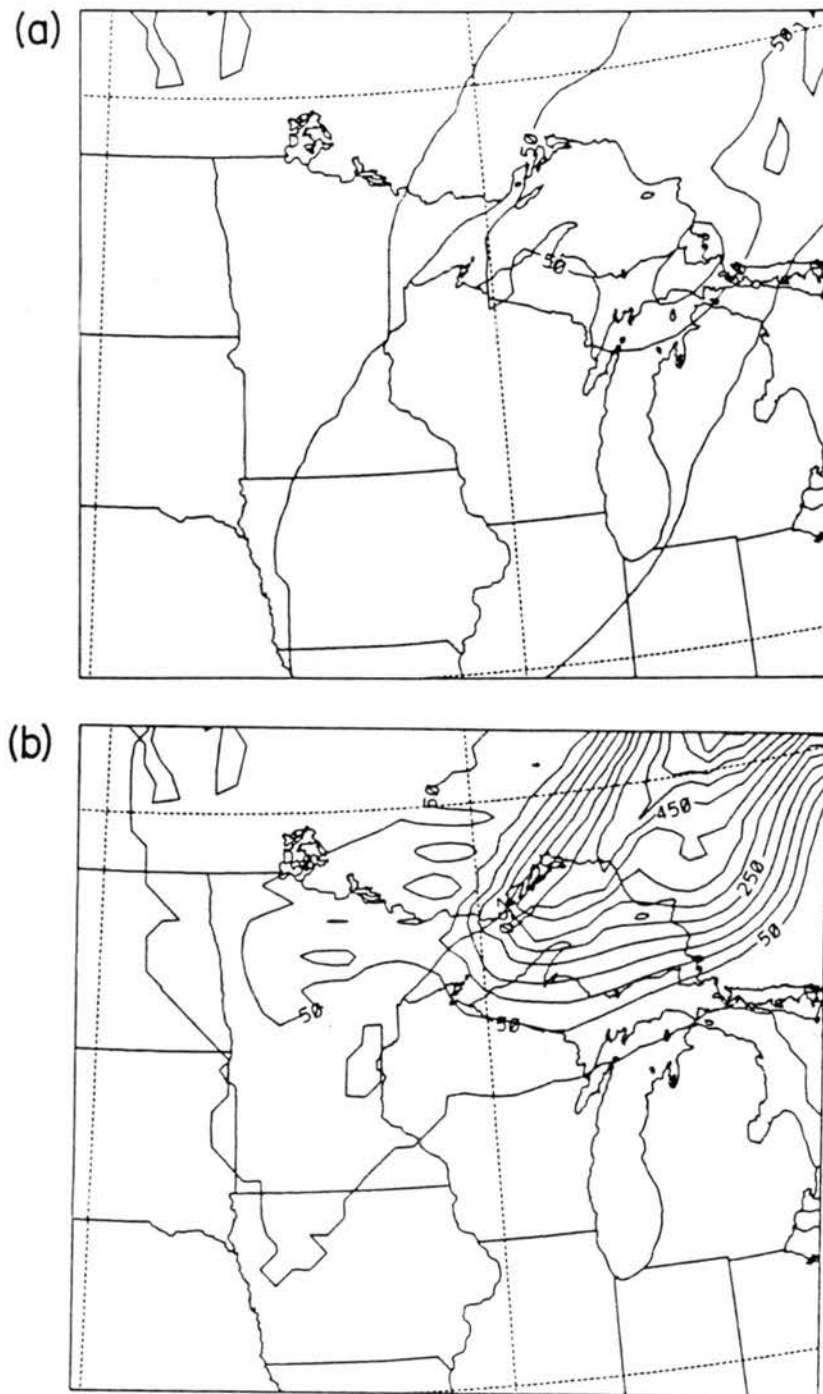
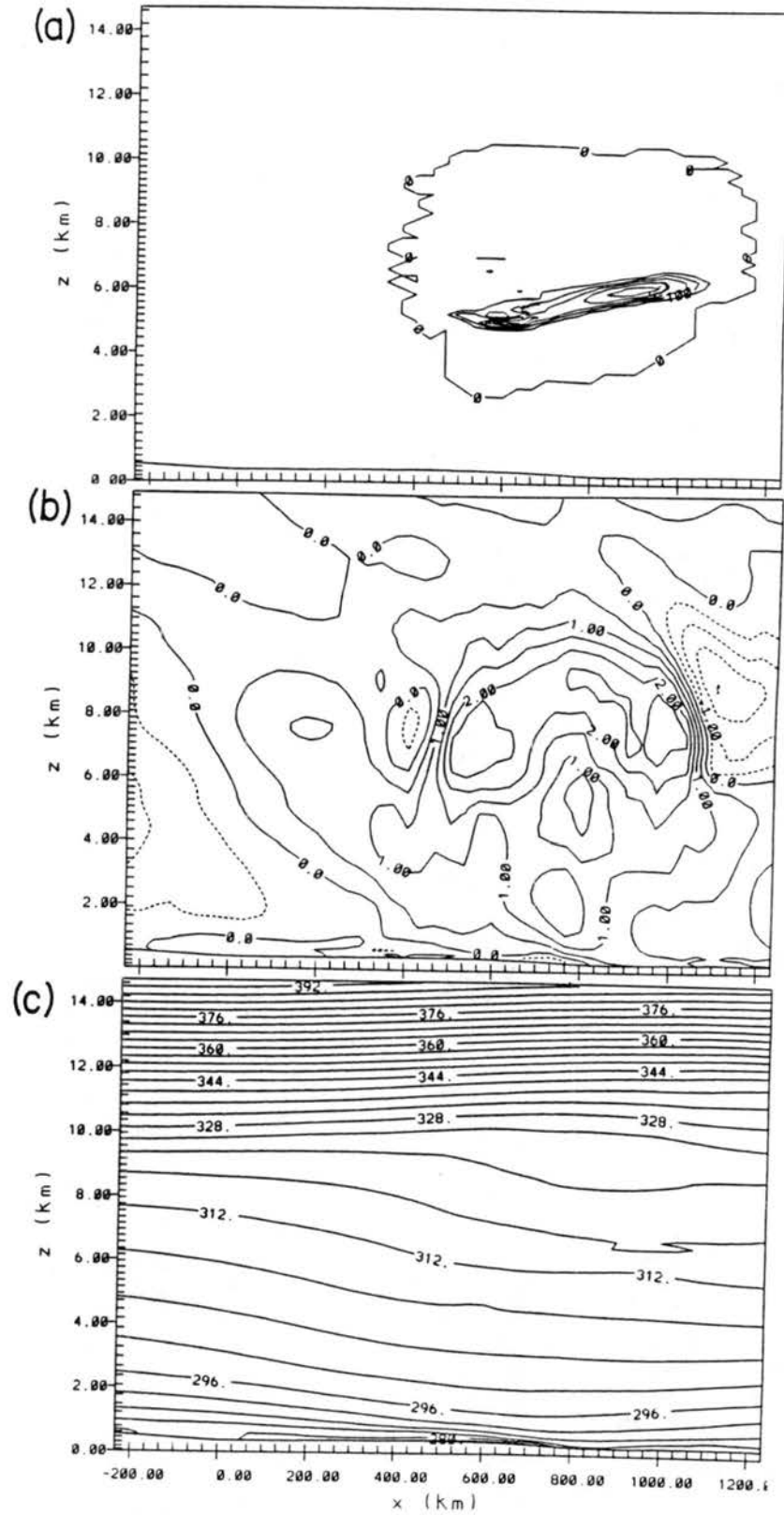Figure 7.2: NLW ice water path at 1900 UTC for (a) 6-12 km, (b) 0-6km.

Figure 7.3: NLW vertical cross sections for $j = 25$ at 1900 UTC of (a) ice water content (g/m^3), (b) vertical motion (cm/s), (c) potential temperature (K).

7.1.3 Discussion

The NLW sensitivity study displays the expected characteristics. Cloud top areas are not cooled without infrared processes and cloud bases are not warmed. The atmosphere is more stable and a less convective vertical motion field results. Without the convective processes to help maintain supersaturation, the clouds are thinner.

7.2 NSW - The shortwave effects on clouds

7.2.1 Description

As in the longwave scheme, the Chen and Cotton (1983a) shortwave radiation scheme tests for condensate in the column. This test was set to fail in the NSW sensitivity simulation. It's important to note that the longwave scheme was left on.

7.2.2 Results

At 1900 UTC, differences were found primarily in the potential temperature field. Figure 7.5a shows this field. Figure 7.1 shows the NSW cloud base and middle to be $\approx 2.5^oC$ cooler and the cloud top to be $\approx 1.0^oC$ cooler than the CNTL cloud. Note that the lapse rate from $6 - 8km$ is virtually the same.

The vertical motion cross section for this time (Figure 7.5b) shows lower amplitude features but the same basic cellular structure found in the CNTL simulation.

Figure 7.4 shows high cloud IWP for 1900 UTC. The overall area matches the CNTL values but the maxima over Lake Michigan is slightly less.

7.2.3 Discussion

The elimination of shortwave effects did not seem to make a large difference in the IWP. The effects were seen in the potential temperature field and were evident as a decrease in the total cloud temperature. The lapse rate was only slightly more stable in the $6 - 8km$ region suggesting that the shortwave radiation warms the entire depth of the cloud. As a result, the convective nature of the lower cloud layer was more evident in the NSW run than the NLW simulation. Cellular activity occured but magnitudes are less than the CNTL run due to the slight increase in stability.
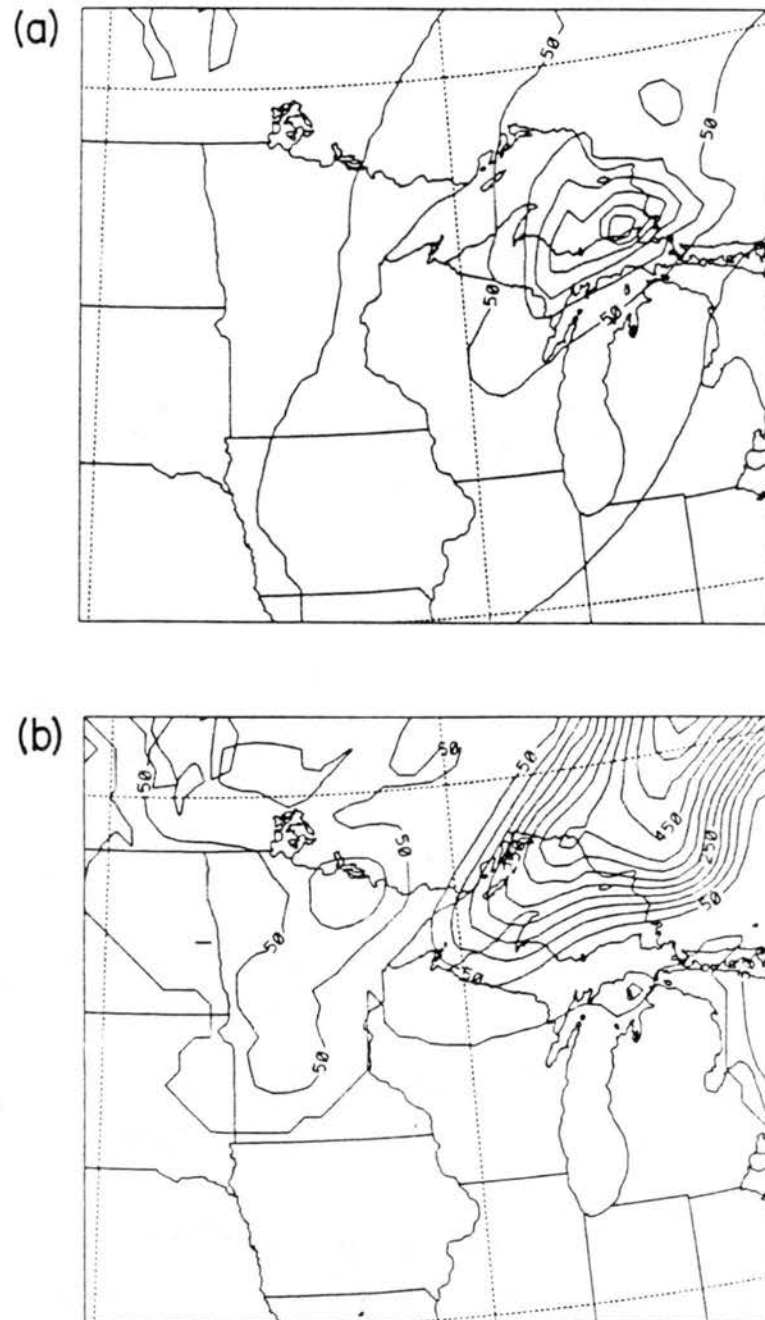
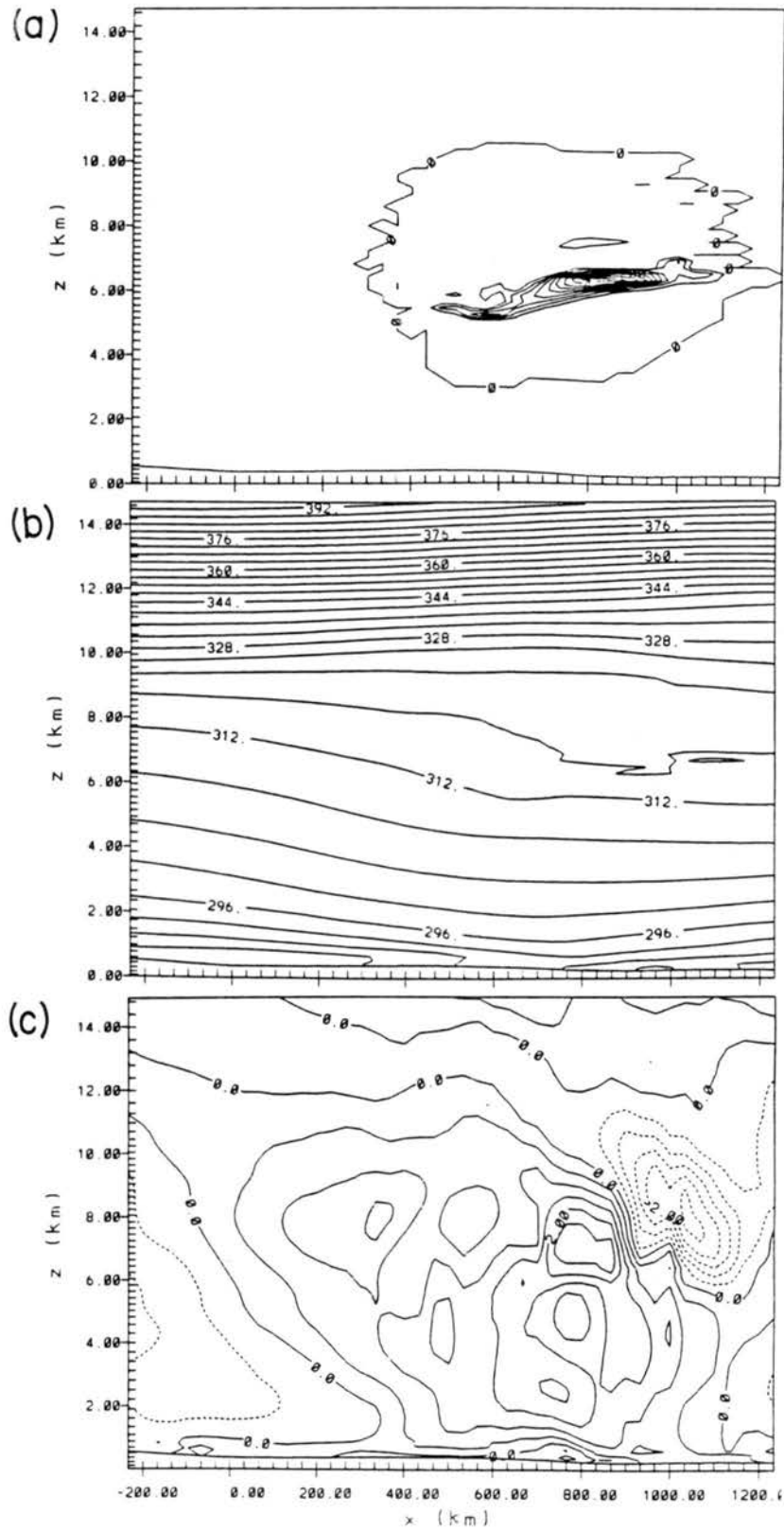Figure 7.4: NSW ice water path at 1900 UTC for (a) 6-12 km, (b) 0-6km.

Figure 7.5: NSW vertical cross sections for $j = 25$ at 1900 UTC of (a) ice water content (g/m^3), (b) vertical motion (cm/s), (c) potential temperature (K).

7.3 NC - The dynamical effects of clouds

7.3.1 Description

RAMS users are allowed to choose a level of microphysical sophistication for their particular simulation. The CNTL simulation had pristine ice, aggregate, cloud water, and rain condensate species while the NC simulation allowed only vapor. No condensate was allowed. This test was designed to show the changes in the dynamical fields due to cloud diabatic effects.

7.3.2 Results

This simulation provides an excellent example of the effects clouds have on their environment. There is a feedback and given time, it could be quite significant.

Figure 7.6a shows the vertical motion field of the NC simulation. It is a smooth, $1cm/s$ updraft associated with the eastside of the longwave trough passing through the area. In contrast, Figure 6.8b is very cellular, convective in nature, and the magnitudes of the upward and downward motion are higher.

Figure 7.6b, when compared to Figure 6.8c, shows that the humidity patterns are almost the same. In areas of cloud, the CNTL pattern has less supersaturation because of condensation.

The NC potential temperature field for 1900 UTC is displayed in Figure 7.6c. Figure 7.1 shows the NC environment to be $\approx 3.2^oC$ cooler at $6.4km$ and $\approx 1.0^oC$ warmer at $10km$.

Note also that the boundary layer in this simulation is much more realistic than the cloudy area in the CNTL run. The CNTL boundary layer is very shallow and has a strong inversion. The NC boundary layer is not nearly as stable and reaches reasonable heights for midday. Figure 4.6 shows the the increase in boundary layer potential temperature for Green Bay.

Another interesting comparison can be made between Figures 7.6d and 6.8f. These show the magnitude of the horizontal wind in a vertical cross section. The NC simulation produces a smooth wind speed pattern associated with steady synoptic scale forcing. The CNTL simulation has horizontal variations in the cloudy region.

107
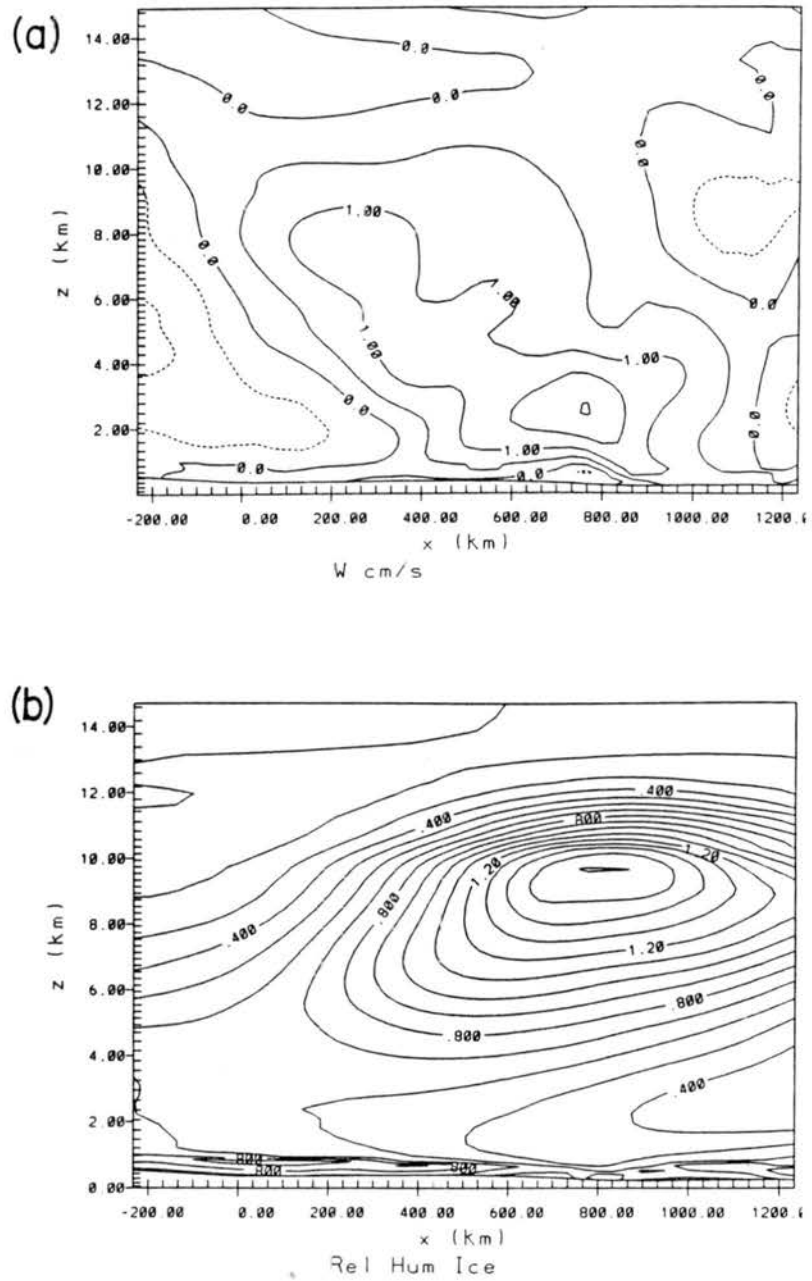
Figure 7.6: NC vertical cross sections for $j = 25$ at 1900 UTC of (a) vertical motion (cm/s), (b) RHi (%), (c) potential temperature (K), (d) horizontal speed (m/s).

(c) Potential Temp

(d) Horiz Speed
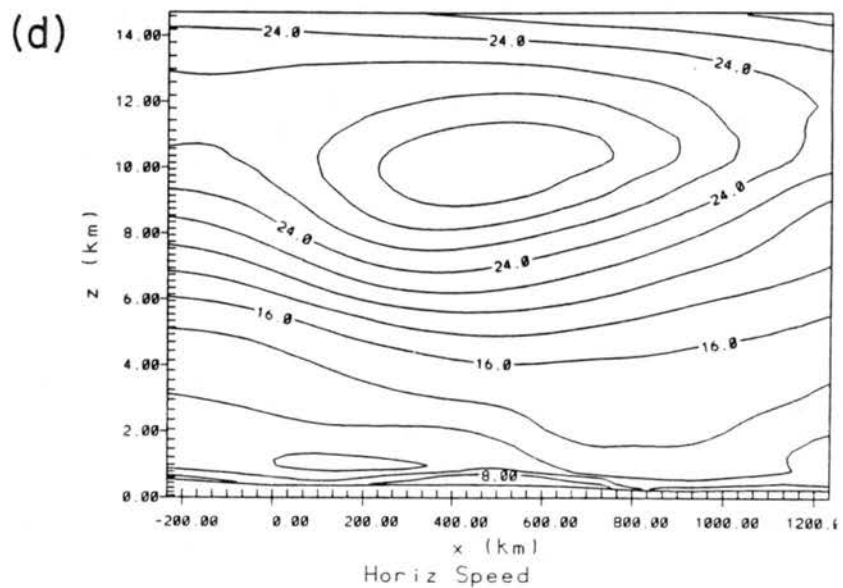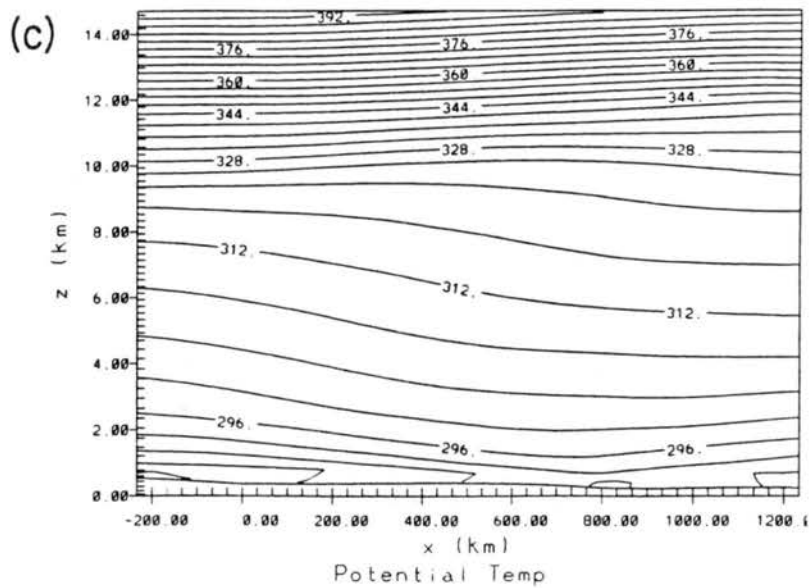
Figure 7.6: Continued.

7.3.3 Discussion

Comparison of the vertical motion fields confirms the convective nature of the thick, lower layer of cloud. By removing the condensate, we've eliminated both the radiative effects and the latent heating effects. From the NLW and NSW results, it appears that longwave radiative effects are the most dominant in changing the cloud environmental lapse rate. There does seem to be some smaller shortwave and latent heating effects.

The humidity patterns are very similar except where clouds have reduced the ice supersaturation. The ice supersaturation was then due to dynamic forces; simple moisture convergence. It also appears to require only weak forcing to produce areas of near water saturation.

What is even more interesting is how the cloud could change upper level wind speeds so dramatically. The increased vertical flux of horizontal momentum may have decreased the wind speeds in the cloud.

Chapter 8

SUMMARY AND CONCLUSIONS

This study had two main goals:

- To simulate a cirrus cloud system and verify the results against a detailed observation data set.

- To use the simulation results along with sensitivity simulation results to further our understanding of the cirrus life cycle.

Accomplishing the second goal depended heavily on the success of the first. To this end, we have recreated the events of 28 October 1986 very well, thus establishing a fair degree of confidence in RAMS ability to simulate cirrus cloud systems. To summarize the study, we'll discuss cloud forcing, the results of the verification, results of the sensitivity analysis, and the simulated cirrus lifecycle. Finally, there will be a short discussion of the vertical grid point resolution required to realistically simulate cirrus layering.

8.1 Cloud forcing mechanisms

The propagation and deepening of a broad upper level trough produced a $1500km$ wide area of $1 - 2cm/s$ upward vertical motion at cirrus levels. This vertical motion was on the east side of the trough as it moved in a southeasterly direction.

A short wave disturbance propagated along the prevailing flow and increased the upward motion in a $\approx 300km$ diameter region.

Once the cloud was established, radiative processes may have destablized the cloudy region and lessened the resistance to convective motions.

8.2   Verification of the CNTL simulation

Verification of the CNTL simulation was accomplished on two scales, synoptic and mesoscale. The synoptic verification compared conditions on the course $100km$ horizontal resolution grid to standard rawinsonde network observations and GOES infrared imagery. The mesoscale verification compared conditions on the nested $33km$ grid to three hourly rawinsonde reports, surface observations and high resolution bispectral satellite imagery.

The synoptic verification showed extremely good agreement between the model generated fields and the 12 hourly synoptic observations. The large scale cloud features matched the infrared satellite imagery to a great degree as well.

The mesoscale verification showed good agreement between model generated surface features and observed surface features. The movement of the surface frontal convergence line was particularly well simulated.

The vertical structure of the high level ice clouds was also well represented. Cloud tops, bases and layered structure all matched aircraft and lidar observations very well, particularly in the pre-clearing cloud system described by Starr and Wylie (1990). The simulation showed the high level generation zone, fall streaks and a lower level convective generation zone.

The model failed to develop the dramatic clearing line obvious in the satellite imagery. Starr and Wylie mention that lidars measured a thin, $10 - 11km$ cloud layer in the clearing area. This is not apparent on satellite imagery. However, the model generated IWP shows minimal values remaining in this area. The model did not produce the vigorous midlevel shortwave disturbance Starr and Wylie infered from rawinsonde data. There was only a weak vertical motion couplet, incapable of reducing humidities to the extent that the cloud would have evaporated. The best explanation for the weakness of the feature is that it was not resolved by the objective analysis of the initial data used to start the simulation.

The simulation of the cold frontal low clouds was good. Low cloud IWP patterns matched infrared and bispectral imagery until late in the period when the simulated clouds appeared to move too far south. This did not occur in the NLW and NSW sensitivity simulations, perhaps suggesting some radiation interaction with low level clouds.

112

And finally, the model did not reproduce 9.5 to 11km convective cirrus clouds that are evident in the satellite imagery after the clearing line. The model did show the tendency for destablization, evident in the soundings from Green Bay, but it never initiated the cellular cloud generation in Wisconsin and Iowa after 1900 UTC. Starr and Wylie suggest the upper level destabilization was due to enhanced cold air advection behind the shortwave disturbance. Since the model created only a weak the shortwave disturbance, the destabilization was much less, and the clouds did not form.

8.3 Sensitivity analysis

The optical depth of the simulated clouds depended heavily on longwave radiation processes. Without the longwave radiation, the clouds were also more stable, evidence of radiative cloud base warming and cloud top cooling. Because of the increased stability, the vertical motions were about 50% less than the CNTL simulation. The resulting clouds had about 50% less ice water content.

The removal of shortwave radiative interaction with condensate did not change the optical depth of the clouds significantly. The clouds were only slightly more stable than CNTL clouds but the whole cloud layer was $\approx 2.5^oC$ cooler without the shortwave heating contribution.

The simulation without condensate showed that high supersaturations with respect to ice at high altitude were due to dynamically-forced moisture convergence. It also showed that the cloud can alter the horizontal flow by increasing the vertical flux of horizontal momentum.

8.4 Simulated cirrus lifecycle

Given RAMS ability to recreate multi-layered high clouds in this case, it is reasonable to discuss aspects of the cirrus lifecycle as modeled for this case.

8.4.1 Formation

Cirrus clouds in this case appeared to be generated by nucleation of areas of near water saturation (RHi of 150%). Lower layers may have been generated when crystals fell from

above into areas of high humidity. These conclusions are substantiated by the ability of the NC sensitivity study to produce very high RHi values at $11km$, evidence of fall streaks and the creation of a second layer below and downstream from the generation areas.

8.4.2 Maintenance

The cloud top generation areas appear to continue to generate as long as supersaturations exist upstream and the ice nuclei are available. The lower layer seems to be maintained and deepened by convective processes initiated by cloud top cooling and cloud base warming. Cloud bases continue to drop as precipitating crystals fall into supersaturated air, evaporate and moisten this subcloud layer. Crystals generated at high levels continue to fall into the lower layer, providing additional nuclei.

8.4.3 Dissipation

The only dissipation mechanism observed in these simulations appeared to be evaporation due to subsidence. Areas of lower humidity were generally associated with weak downward motions but since the motions were weak, the drying did not occur instantaneously. As a result, clouds existed in areas of weak subsidence.

8.5 Vertical resolution

These simulations show that a model with $200m$ vertical resolution is capable of reproducing some cirrus layers. Reproducing the $200m$ thick layer observed at $11.3km$ on this day would have required $50m$ resolution. This resolution is obviously completely unrealistic for climate models or operational mesoscale forecast models. Cirrus parameterizations will require a vertical quantity analogous to cloud fractional coverage in the horizontal. It remains to be determined how this measure of layering can be related to environmental conditions.

Chapter 9

SUGGESTIONS FOR FURTHER RESEARCH

As this study comes to a close, there are certainly many more questions to be answered. Research on cirrus cloud dynamics is just beginning. RAMS is an excellant tool for preforming a wide range of future cirrus simulations.

As a continuation of the simulations described here, further sensitivity studies could explore the data and grid resolutions necessary to predict realistic cirrus clouds in an operational mode. What vertical resolution is needed to represent layering? What horizontal resolution is necessary to represent the mesoscale variability in cirrus? What initial, high-level, moisture data is required?

The addition of high resolution nests would help determine the scales of organization in cirrus clouds. RAMS could be configured as a cloud model for large eddy type simulations of the role of turbulence in the cirrus lifecycle.

The ice phase parameterization in RAMS could be expanded to include homogeneous nucleation processes, a radiative contribution to crystal growth and a multi-modal crystal size spectra.

In addition to cirrus specific research, the pursuit of a faster longwave radiation scheme and improved initial data assimilation would aid future cirrus modeling efforts.

Bibliography

Arakawa, A. and V. R. Lamb, 1981: A potential enstrophy and energy conserving scheme for the shallow water equations. *Mon. Wea. Rev.*, **109**, 18–36.

Barnes, S. L., 1973: Mesoscale objective map analysis using weighted time series observations. ERL NSSL-62 NTIS COM-73-10781, NOAA, 60.

Braham, Jr., R. R. and P. Spyers-Duran, 1967: Survival of cirrus crystals in clear air. *J. Appl. Meteor.*, **6**, 1053—1061.

Chen, C. and W. R. Cotton, 1983a: Numerical experiments with a one-dimensional higher order turbulence model: Simulation of the wangara day 33 case. *Boundary-Layer Meteorol.*, **25**, 375—404.

Chen, C. and W. R. Cotton, 1983b: A one-dimensional simulation of the stratocumulus-capped mixed layer. *Boundary-Layer Meteorology*, **25**, 289–321.

Ciesielski, P. E., D. E. Stevens, R. H. Johnson, and K. R. Dean, 1989: Observational evidence of asymmetric inertial instability. *J. Atmos. Sci.*, **46**, 817–831.

Clark, T. L., 1977: A small-scale dynamic model using a terrain-following coordinate transformation. *J. Comput. Phys*, **24**, 186–215.

Conover, J. H., 1960: Cirrus patterns and related air motions near the jet stream as derived by photography. *J. Meteor.*, **17**, 532—546.

Cotton, W. R., M. A. Stephens, T. Nehrkorn, and G. J. Tripoli, 1982: The Colorado State University three-dimensional cloud/mesoscale model - 1982, PartII: an ice parameterization. *J. Rech. Atmos.*, **16**, 295–320.

Cram, J. M., 1990: *Numerical Simulation and Analysis of the Propagation of a Prefrontal Squall Line.* PhD thesis, Colorado State University, Fort Collins, Colorado, 332 pp.

Dalu, G. A., P. J. Flatau, R. A. Pielke, and G. L. Stephens, 1990: Horizontal structure of cirrus clouds – analytical theory. In *1990 conference on cloud physics*, American Meteorological Society, AMS, 45 Beacon Street, Boston, Mass., 613–616. San Francisco, Calif.

Durran, D., 1986: *Mesoscale meteorology and forecasting.* American Meteorological Society, 792 pp.

Durran, D. R. and D. B. Weber, 1988: An investigation of the poleward edges of cirrus clouds associated with midlatitude jet streams. *Mon. Wea. Rev.*, **116**, 702–714.

Flatau, P. J., 1990: *Theoretical and numerical studies of cirrus clouds.* PhD thesis, Colorado State University, Fort Collins, CO 80523. Department of Atmospheric Science.

Flatau, P. J., G. A. Dalu, W. R. Cotton, G. L. Stephens, and A. J. Heymsfield, 1989: Mixed layer model of cirrus clouds: Growth and dissipation mechanisms. In *Symposium on the role of clouds in atmospheric chemistry and global climate*, American Meteorological Society, 151—156.

Flatau, P. J., I. Gultepe, G. Nastrom, W. R. Cotton, and A. J. Heymsfield, 1990: Cirrus cloud spectra and layers observed during the FIRE and GASP projects. In *1990 conference on cloud physics*, American Meteorological Society, AMS, 45 Beacon Street, Boston, Mass., 200–206. San Francisco, Calif.

Flatau, P. J., G. J. Tripoli, J. Verlinde, and W. R. Cotton, 1989: The CSU-RAMS cloud microphysics module: General theory and code documentation. Technical Report 451, Colorado State University, Fort Collins, Colorado 80523.

Gal-Chen, T. and R. C. J. Somerville, 1975: On the use of a coordinate transformation for the solution of the Navier-stokes equations. *J. Comput. Phys*, **17**, 209–228.

Grund, C. J. and E. W. Eloranta, 1990: The 27-28 October, 1986 FIRE Cirrus Cloud Study: Cloud optical properties determined by high spectral resolution lidar. *Mon. Wea. Rev.*, **118**, 2344–2355.

Gultepe, I., A. J. Heymsfield, and G. V. Rao, 1990: Moisture and heat budget of a cirrus cloud from aircraft measurements during FIRE - october 31 case study. In *AMS cloud physics conference*, AMS. San Francisco.

Heymsfield, A. J., 1972: Ice crystal terminal velocities. *J. Atmos. Sci.*, **29**, 1348—1356.

Heymsfield, A. J., 1975a: : Cirrus uncinus generating cells and the evolution of cirriform clouds. part i: Aircraft observations of the growth of the ice phase. *J. Atmos. Sci.*, **32**, 799—808.

Heymsfield, A. J., 1975b: Cirrus uncinus generating cells and the evolution of cirriform clouds. part ii: The structure and circulations of the cirrus uncinus generating head. *J. Atmos. Sci.*, **32**, 809—819.

Heymsfield, A. J. and R. G. Knollenberg, 1972: Properties of cirrus generating cells. *J. Atmos. Sci.*, **29**, 1358—1368.

Heymsfield, A. J., K. M. Miller, and J. D. Spinhirne, 1990: The 27–28 October, 1986 FIRE cirrus case study: Cloud microstructure. *Mon. Wea. Rev.*, **118**, 2313–2328.

Heymsfield, A. J. and C. M. R. Platt, 1984: Parameterization of the particle size spectrum of ice clouds in terms of the ambient temperature and the ice water content. *J. Atmos. Sci.*, **41**, 846—855.

Hill, G. E., 1974: Factors controlling the size and spacing of cumulus clouds as revealed by numerical experiments. *J. Atmos. Sci.*, **31**, 646–673.

Klemp, J. B. and D. K. Lilly, 1978: Numerical simulation of hydrostatic mountain waves. *J. Atmos. Sci.*, **35**, 78–107.

Klemp, J. B. and R. B. Wilhelmson, 1978: Simulations of right- and left-moving storms produced through storm-splitting. *J. Atmos. Sci.*, **35**, 1097–1110.

Lilly, D. K., 1962: On the numerical simulation of buoyant convection. *Tellus*, **14**, 148–172.

Lilly, D. K., 1988: Cirrus outflow dynamics. *J. Atmos. Sci.*, **45**, 1594—1604.

Louis, J. F., 1979: A parametric model of vertical eddy fluxes in the atmosphere. *Boundary-Layer Meteorol.*, **17**, 187–202.

Mahrer, Y. and R. A. Pielke, 1977: A numerical study of the airflow over irregular terrain. *Beitr. Phys. Atmos.*, **50**, 98–113.

McCumber, M. C. and R. A. Pielke, 1981: Simulation of the effects of surface fluxes of heat and moisture in a mesoscale numerical model. Part I: Soil model. *J. Geophys. Res.*, **86**, 9929—9938.

McNider, R. T. and R. A. Pielke, 1981: Diurnal boundary-layer development over sloping terrain. *J. Atmos. Sci.*, **38**, 2198–2212.

Meyers, M. P., P. J. Demott, and W. R. Cotton, 1991: New primary ice nucleation parameterizations in an explicit cloud model. Submitted to J. Appl. Meteor.

Minnis, P., P. Heck, and E. F. Harrison, 1990: The 27-28 October 1986 FIRE IFO Cirrus Case Study: Cloud parameter fields derived from satellite data. *Mon. Wea. Rev.*, **118**, 2426–2446.

Nicholls, M. E., W. R. Cotton, S. T. Heckman, P. J. Flatau, and C. J. Tremback, 1990: A modeling investigation of the 28 October 1986 FIRE cirrus case. In *1990 conference on cloud physics*, American Meteorological Society, AMS, 45 Beacon Street, Boston, Mass., 207–210. San Francisco, Calif.

Pielke, R. A., 1974: A three-dimensional numerical model of the sea breezes over south Florida. *Mon. Wea. Rev.*, **102**, 115–134.

Quante, M., 1989: Flugzeugmessungen der Turbulenzstruktur in Cirruswolken. Technical Report 65, Institut für Geophysik und Meteorologie der Universität zu Kö ln, Köln, 121.

Reuss, J. H., 1967: Wolken-Stereomessbildreichen, II; Grossraumige cirrus bandes als merkale von Luftmassengrenzen der hohes troposphare and ihrer Eigenshaften. *Beitr. Phys. Atmos.*, **36**, 7–15.

Sassen, K., C. J. Grund, J. D. Spinhirne, M. Hardesty, and J. M. Alvarez, 1990: The 27-28 October, 1986 FIRE Cirrus Case Study: A five lidar overview of cloud structure and evolution. *Mon. Wea. Rev.*, **118**, 2288–2312.

Sassen, K., D. O. Starr, and T. Uttal, 1989: Mesoscale and microscale structure of cirrus clouds: Three case studies. *J. Atmos. Sci.*, **46**, 371–396.

Smagorinsky, J., 1963: General circulation experiments with the primitive equations. I. The basic experiment. *Mon. Wea. Rev.*, **91**, 99–164.

Smith, W. L., P. Hein, and S. K. Cox, 1990: The 27-28 October, 1986 FIRE Cirrus Case Study: In situ observations of radiation and dynamic properties of a cirrus cloud layer. *Mon. Wea. Rev.*, **118**, 2389–2401.

Stackhouse, P. W., 1989: A theoretical and observational comparison of cirrus cloud radiative properties. Master's thesis, Colorado State University, Fort Collins, CO 80523. Department of Atmospheric Science.

Starr, D. O., 1987: A cirrus cloud experiment: Intensive field observations planned for FIRE. *Bull Am. Met. Soc.*, **67**, 119–124.

Starr, D. O. and S. K. Cox, 1980: Characteristics of middle and upper tropospheric clouds as deduced from rawinsonde data. Atmospheric Science Paper 327, Department of Atmospheric Science, Colorado State University, Fort Collins, CO.

Starr, D. O. and S. K. Cox, 1985a: Cirrus clouds. Part I: A cirrus cloud model. *J. Atmos. Sci.*, **42**, 2663—2680.

Starr, D. O. and S. K. Cox, 1985b: Cirrus clouds. Part II: Numerical experiments on the formation and maintenance of cirrus. *J. Atmos. Sci.*, **42**, 2682—2694.

Starr, D. O. and D. P. Wylie, 1990: The 27-28 October 1986 FIRE IFO cirrus cloud study: Meteorology and clouds. *Mon. Wea. Rev.*, **118**, 2259–2287.

Tremback, C. J., 1990: *Numerical simulation of a mesoscale convective complex: model development and numerical results.* PhD thesis, Colorado State University, Dept. of Atmospheric Science, Fort Collins, CO 80523, 274. Also published as Atmos. Sci. Paper No. 465.

Tremback, C. J., G. J. Tripoli, and W. R. Cotton, 1985: A regional scale atmospheric numerical model including explicit moist physics and a hydrostatic time-split scheme. In *Preprints, 7th Conference on Numerical Weather Prediction*, AMS, AMS, Montreal, 355—358.

Trenberth, K. E. and J. G. Olson, 1988: ECMWF global analysis 1979-1986: circulation statistics and data evaluation. Tech Note 300, NCAR, 82 pp.

Tripoli, G. J., 1988: *A numerical investigation of an orogenic mesoscale convective system.* PhD thesis, Dept. of Atmospheric Science, Colorado State University, Ft. Collins, CO, 290 pp.

Tripoli, G. J. and W. R. Cotton, 1980: A numerical investigation of several factors leading to the observed variable intensity of deep convection over South Florida. *J. Appl. Met.*, **19**, 1037–1063.

Tripoli, G. J. and W. R. Cotton, 1982: The Colorado State University three-dimensional cloud/mesoscale model-1982. Part I: General theoretical framework and sensitivity experiments. *J. Rech. Atmos.*, **16**, 185–220.

Tripoli, G. J. and W. R. Cotton, 1989: Numerical study of an observed orogenic mesoscale convective system. Part 1: Simulated genesis and comparison with observations. *Mon. Wea. Rev.*, **117**, 273–304.

Varley, D. J., I. D. Cohen, and A. A. Barnes, 1980: Cirrus particle distribution study, Part VII. Technical Report AFGL-TR-80-0324, Air Force Geophysics Laboratory, Hanscom AFB, 82 pp.

Yagi, T., 1969: On the relation between the shape of cirrus clouds and the static stability of the cloud level – studies of cirrus cloud: Part IV. *J. Met. Soc. Jap.*, **47**, 59—64.
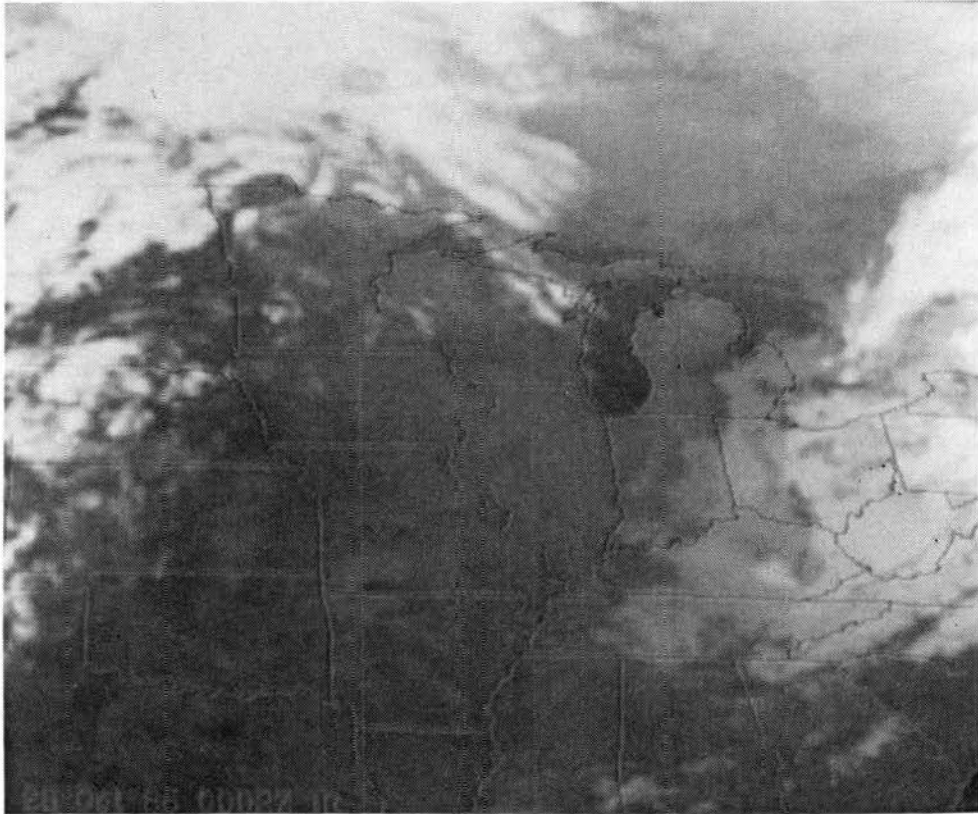
Appendix A

SATELLITE IMAGERY

123

Figure A.1: Infrared imagery from GOES channel 8 at 0002 UTC on 28 Oct 86.

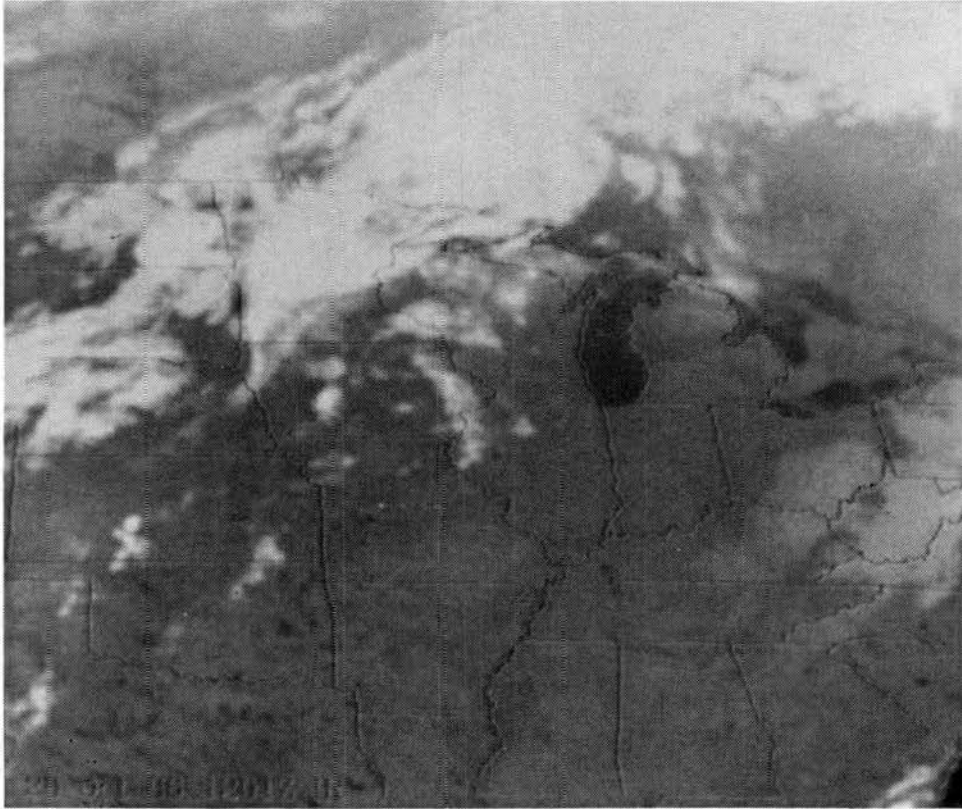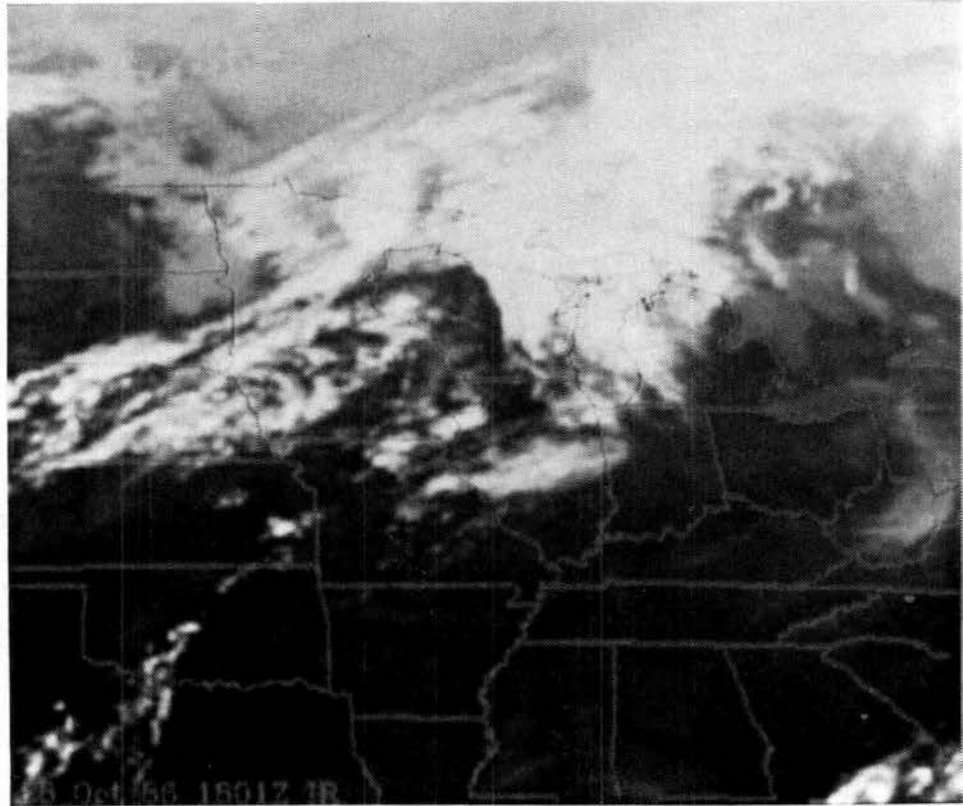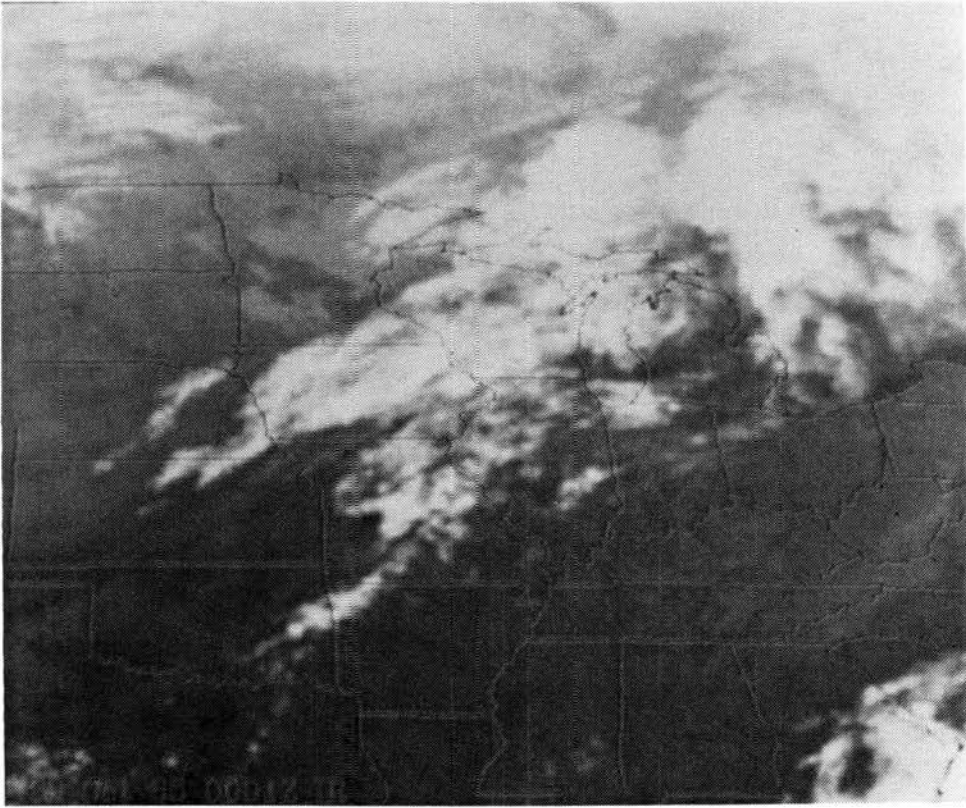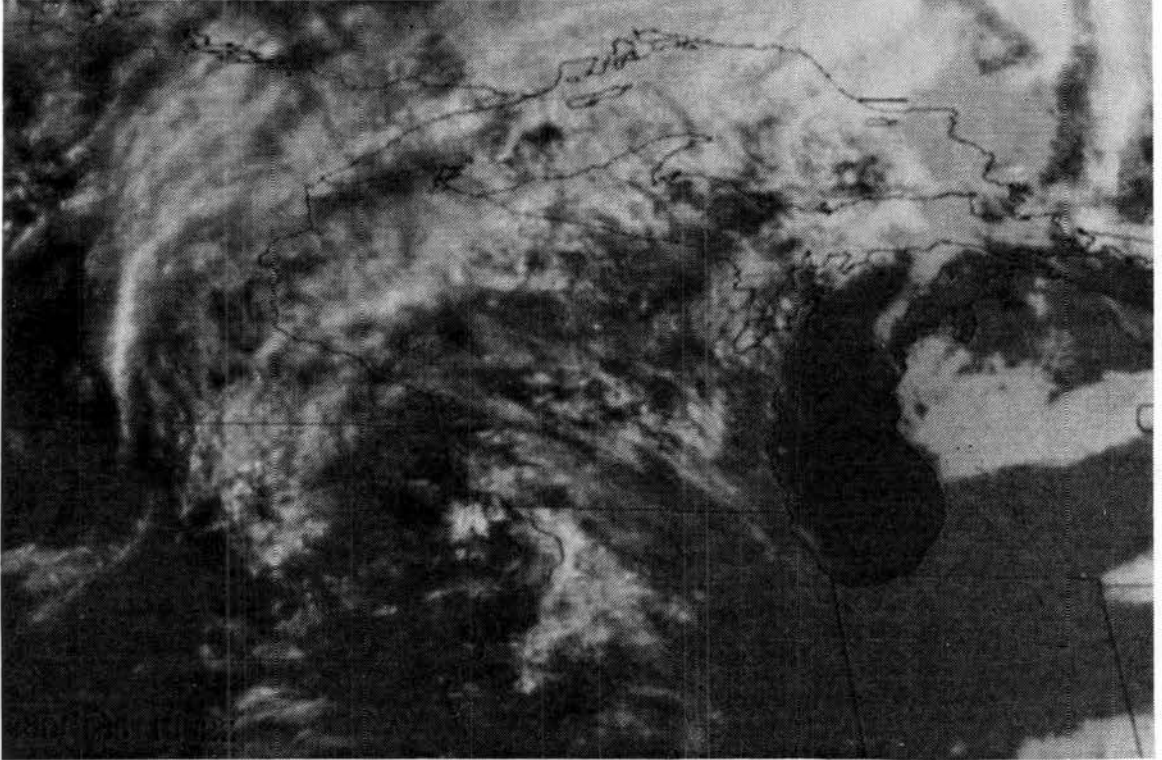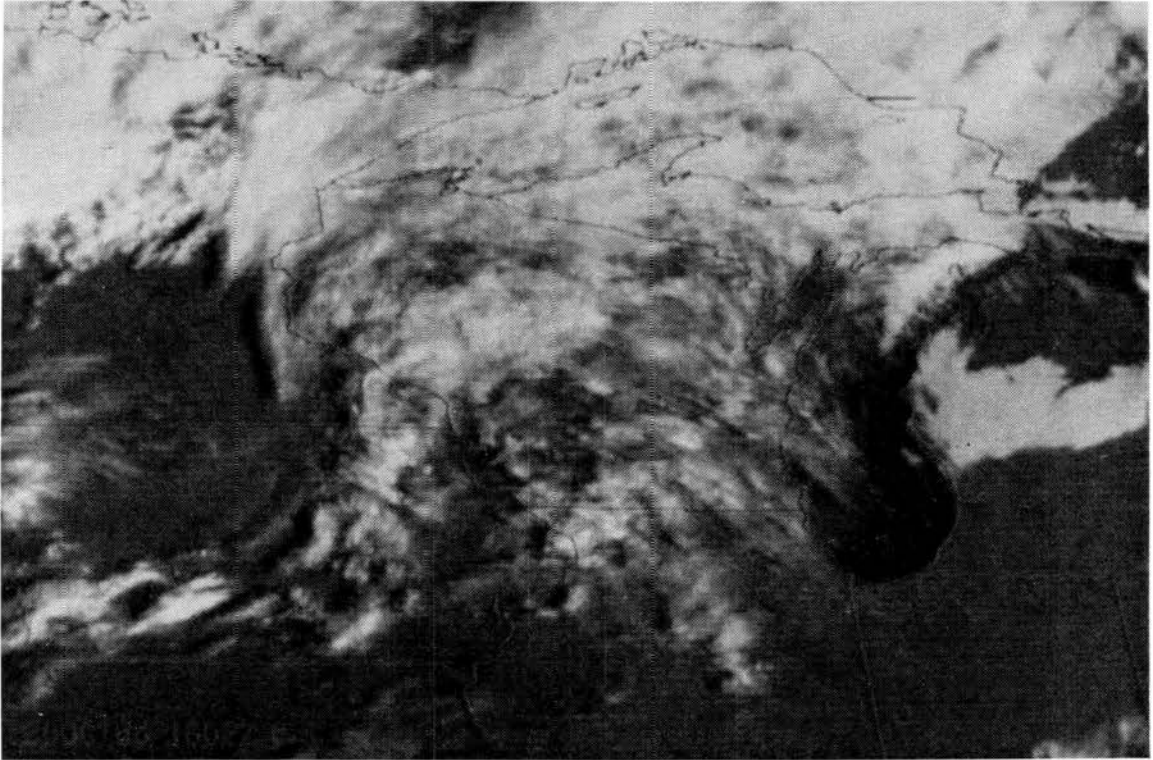Figure A.2: Infrared imagery from GOES channel 8 at 0602 UTC on 28 Oct 86.

Figure A.3: Infrared imagery from GOES channel 8 at 1202 UTC on 28 Oct 86.

Figure A.4: Infrared imagery from GOES channel 8 at 1802 UTC on 28 Oct 86.

Figure A.5: Infrared imagery from GOES channel 8 at 0002 UTC on 29 Oct 86.

Figure A.6: Bispectral imagery from GOES at 1332 UTC on 28 Oct 86.

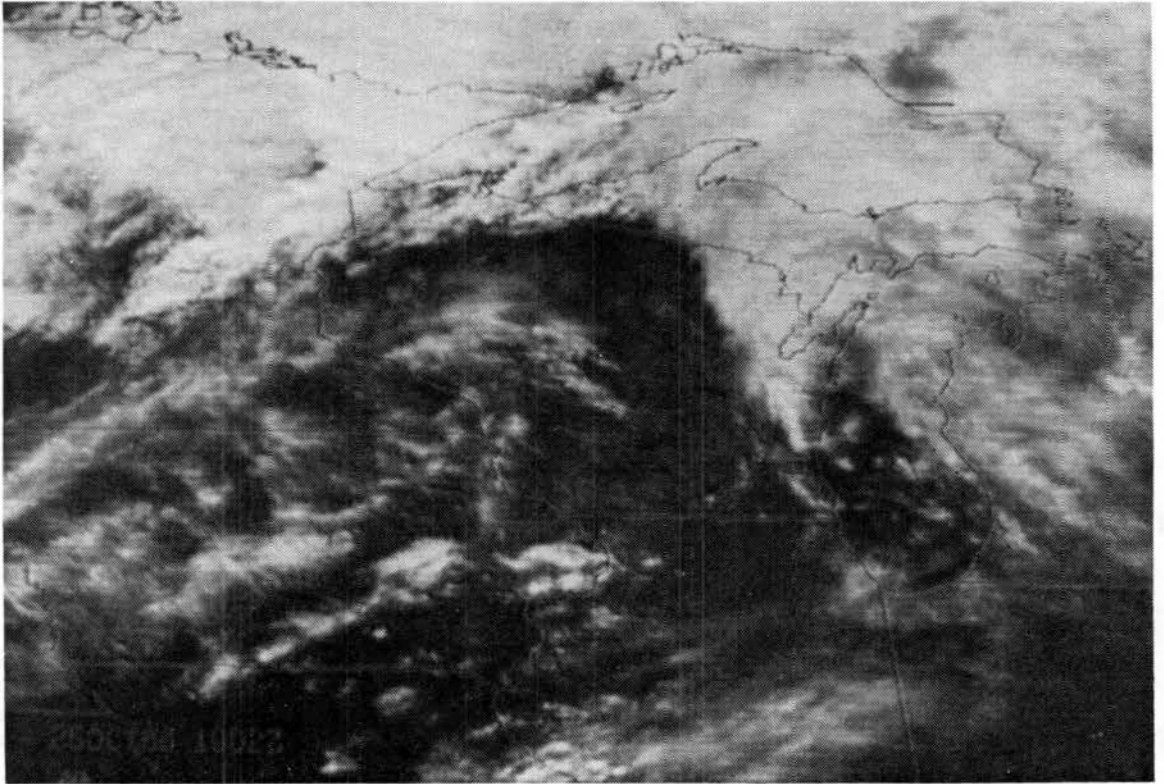Figure A.7: Bispectral imagery from GOES at 1502 UTC on 28 Oct 86.

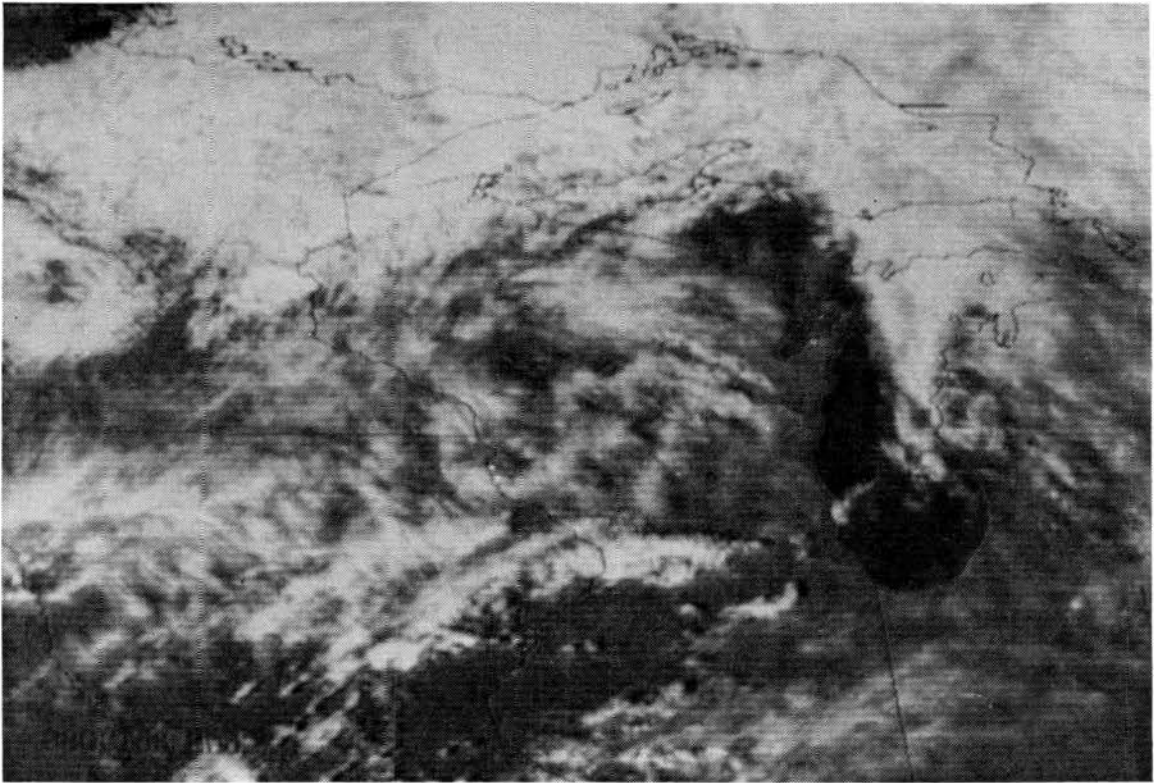Figure A.8: Bispectral imagery from GOES at 1902 UTC on 28 Oct 86.

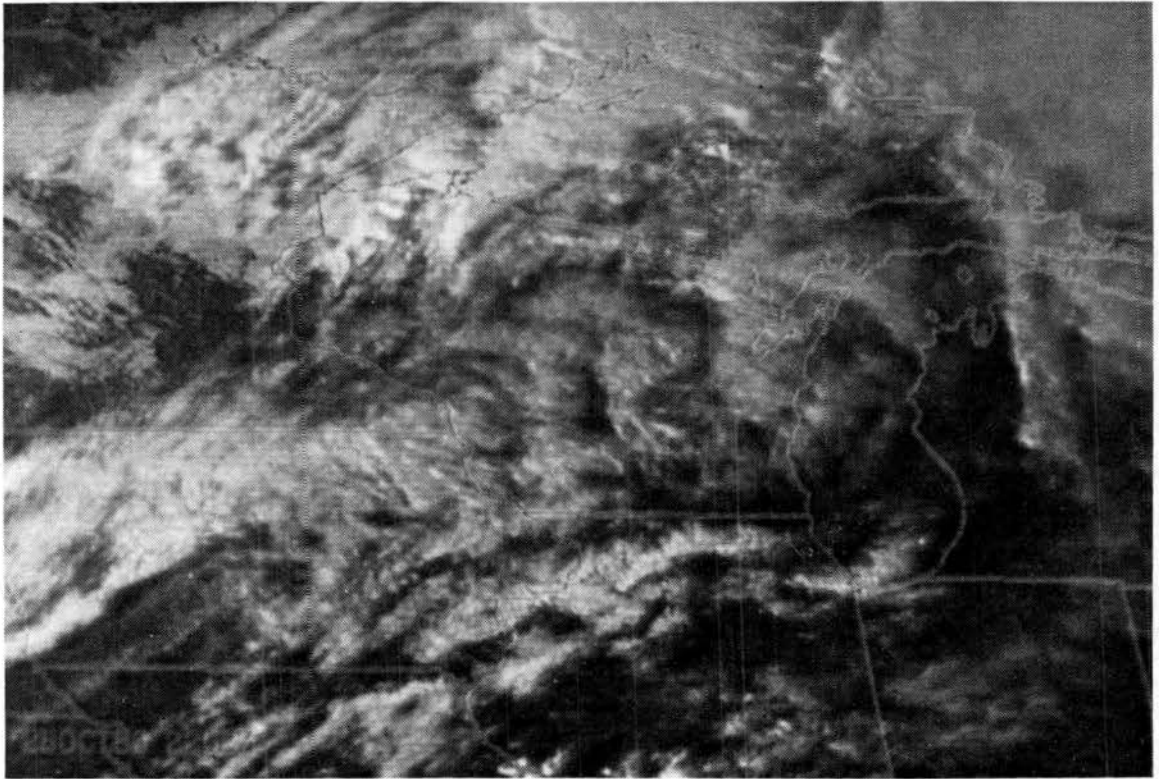Figure A.9: Bispectral imagery from GOES at 2032 UTC on 28 Oct 86.

Figure A.10: Bispectral imagery from GOES at 2202 UTC on 28 Oct 86.

561119